



City Research Online

City, University of London Institutional Repository

Citation: Court, Alecsandra (2025). Baromorphing Active Wing Technologies for future zero-emission flight by pneumatic control (BAWTech). (Unpublished Doctoral thesis, City St George's, University of London)

This is the accepted version of the paper.

This version of the publication may differ from the final published version.

Permanent repository link: <https://openaccess.city.ac.uk/id/eprint/35255/>

Link to published version:

Copyright: City Research Online aims to make research outputs of City, University of London available to a wider audience. Copyright and Moral Rights remain with the author(s) and/or copyright holders. URLs from City Research Online may be freely distributed and linked to.

Reuse: Copies of full items can be used for personal research or study, educational, or not-for-profit purposes without prior permission or charge. Provided that the authors, title and full bibliographic details are credited, a hyperlink and/or URL is given for the original metadata page and the content is not changed in any way.

City Research Online:

<http://openaccess.city.ac.uk/>

publications@city.ac.uk

Baromorphing Active Wing Technologies for
future zero-emission flight by pneumatic control
(BAWTech)



Miss Alecsandra Court

A thesis presented for the degree of
Doctor of Philosophy

City, University of London
Aeronautics and Aerospace Research Centre

January 2025

Acknowledgements

Firstly, I would like to thank my primary supervisor, Professor Christoph Bruecker, for his guidance and vast wealth of knowledge both during my undergraduate and postgraduate studies. It really would not have been possible otherwise. I would also like to thank Professor Ken Grattan, for welcoming me into the Worshipful Company of Scientific Instrument Makers. The livery company has provided funding but also an invaluable network and for that I am thankful. I also am very grateful to the technicians, Keith, Richard and Kugan for their help.

Secondly, I also thank Omar, for his unjudgemental help with my never-ending questions and much-needed friendship throughout my postgraduate studies.

Finally, I would like to thank my fiancé, Ollie, for his constant support, love and optimism at every step. He really helped me keep my marbles together.

Declaration

I, Alecsandra Cristina Maria Court, confirm that the work presented in this thesis, titled "Baromorphing Active Wing Technologies for future zero-emission flight by pneumatic control (BAWTech)", is my own. I confirm the following:

- Where information has been derived from other sources, I confirm that it has been indicated in the thesis;
- Any main sources of help have been listed;
- Where I have quoted the work of others, the source is clearly listed. Excluding such quotations, the work is entirely my own.
- Part of the thesis has been published.

Signed: _____

Date: _____

Abstract

This thesis presents a set of three follow on experimental papers carried out on NACA 0012 aerofoils either with active trailing edge flaplets or an array of sensing hairs. The experiments investigate using pneumatics for active flow control via trailing edge flaplets and then bio-inspired sensing flow hairs, including a new camera setup for sensing hair monitoring.

The pneumatic flaplets were inspired by the pop-up feathers that birds have, that aid them during different flight manoeuvres. The flaplets were designed and tested before being used as an upstream gust generator. The sensing hairs were a continuation of work already carried out at City, University of London but were adapted to be an integrated sensing array. The tips of the hairs were monitored via PIV and their ability to detect flow structures was analysed. Finally, an EBC was considered as a replacement for the high-speed camera for the same setup with the sensing hairs and showed potential for future studies.

The first study was a fluid dynamics study via PIV into the effect that the flaplets had on the nearby and downstream flow in the water tunnel. It was found that, during the opening stages of the flaplet, fluid is drawn in from the boundary layer and then expelled during the closing stages, generating a vortex that travels downstream.

The second study used an integrated array of flow-sensing hairs, placed downstream of the gust generator. The movement of the tips of the hairs was monitored via a high-speed camera and was compared to PIV images taken at the same location, under the same tunnel conditions. It was found that the hairs can detect the arrival, size and structure of the flow disturbance, giving us a flow 'footprint'.

The third study was a feasibility study, into using an EBC in place of a high-speed camera with the sensing hairs. Comparative experiments were carried out in both air and water using both cameras and the sensing hairs under different flow conditions. The results demonstrate the ability that the EBCs have to detect large flow structures and show promise for real-time flow monitoring.

Contents

Acknowledgements	iii
Declaration	iv
Abstract	1
List of figures	6
Nomenclature	9
1 Introduction	10
1.1 Thesis Layout	10
1.2 Introduction	11
2 Paper 1-Design and implementation of spanwise lift and gust control via arrays of bio-inspired individually actuated pneumatic flaplets	16
2.1 Abstract	17
2.2 Introduction	17
2.2.1 Scope	18
2.3 Design and Construction of Spanwise Control Concept	18
2.3.1 Design Background	18
2.3.2 Construction	20
2.4 Water Tunnel Test	22
2.4.1 Experimental Setup	22
2.4.2 Actuation Control	23
2.4.3 Test Description	26
2.5 Test Results	26
2.6 Conclusions	28
2.7 Outlook	31
2.8 Critical Review	32
2.8.1 Paper Overview	32
2.8.2 Supplementary Infomation	32
2.8.3 Problems and Limitations	33
2.8.4 PIV Uncertanties	34
2.8.5 Future Work	34
2.8.6 Measurements for the future	36
3 Paper 2-Fly by Feel: Flow Event Detection via Bioinspired Wind-Hairs	39
3.1 Abstract	40
3.2 Introduction	40
3.3 Materials and Methods	42
3.3.1 Disturbance generation	42
3.3.2 Experimental setup for PIV	43

3.3.3	PIV processing	44
3.3.4	Sensing pillars	45
3.3.5	Experimental setup for pillar tracking	47
3.4	Results	48
3.4.1	PIV Disturbance Characterisation	48
3.4.2	Disturbance sensing via pillars	52
3.5	Discussion	53
3.6	Conclusion	54
3.7	Critical Review	55
3.7.1	Paper Overview	55
3.7.2	Supplementary Information	55
3.7.3	Problems and Limitations	56
3.7.4	PIV Uncertainties	57
3.7.5	Future Work	57
3.7.6	Measurements for the Future	58
4	Paper 3(Unpublished)-Event Based Cameras: A Comparative Study For Fluid Event Detection	61
4.1	Abstract	62
4.2	Introduction	62
4.3	Background	63
4.4	Experimental Setup	64
4.4.1	Dynamic water test	65
4.4.2	Static air test	66
4.5	Results	66
4.5.1	Dynamic water test	66
4.5.2	Single gust disturbance	70
4.5.3	Cross flow disturbance	71
4.6	Conclusions	72
4.7	Extension	73
4.7.1	Further experimental setup	73
4.7.2	Further results	74
4.7.3	Further discussion	77
4.8	Critical Review	78
4.8.1	Paper Overview	78
4.8.2	Supplementary Information	78
4.8.3	Problems and Limitations	78
4.8.4	Future Work	79
4.8.5	Measurements for the Future	80
5	Conclusions	82
5.1	Concluding Remarks	83
5.2	Purpose and Novelty	83
5.3	Future Work	84
5.4	Emerging Topics	84

6	Calibration of Equipment	87
6.1	Water Tunnel	88
6.2	Wind Hairs	89
7	Appendices	100
7.1	A	100

List of Figures

1	The first flight in the Wright Flyer on Kill Devil Hills	11
2	Airbus's 'Bird of Prey' concept	12
3	NACA0012 aerofoil model with individual pneumatically actuated spanwise trailing edge flaps concept. The model consists of 8 single segments in the spanwise direction, which each has a flap to be actuated with a controlled opening-closing cycle.	19
4	Top end plate, shown with mounting piece fitted and recessed fittings. The mounting piece is the support for the sting as a stable connector to the traverse in the tunnel.	20
5	A single segment of the aerofoil with the balloon inside. Top: the inflated situation with the flap deployed. Bottom: deflated position as the reference situation with the flap flush with the trailing edge.	21
6	Balloon-to-pressure line fitting, using the typical syringe-type Luer cone connector used in medical devices such as for the balloon catheter in use.	21
7	Schematic control diagram of the pneumatic control system.	22
8	Schematic of the experimental setup in the water tunnel, top view. Flow is in negative x-direction from bottom to top.	23
9	Schematic of the experimental setup in the water tunnel, front view. Flow is in negative x-direction from right to left.	24
10	Valve control unit with Arduino controller (top) and shown in the lab with pressure lines connected to the balloons in the aerofoil (bottom).	25
11	Typical flap actuation patterns used in the control tests. All open (left) and simulation of a spanwise wave pattern with 1,4,5,8 open (right).	26
12	Picture of the water tunnel with the model inside and the optical setup for PIV measurements with LED light from the left and camera looking from the bottom.	27
13	Flow visualisation using multi-exposed particle traces during opening and closing of the trailing edge flap row (the top figure has double the exposure time compared to the bottom).	29
14	Velocity vectors overlaid on the colour-coded vorticity field (rainbow colour distribution) for three successive time-steps of the flow, 0.5 chord length downstream of the trailing edge after flap action. (Flow direction is from the top to the bottom).	30
15	Schematic showing the setup to determine the zero AoA	32
16	Schematic of the pneumatic system	42
17	Schematic of the actuation	43
18	Schematic of the PIV setup for the measurements in the vertical plane (camera outside of the tunnel).	44

19	Schematic of the flexible pillar sensor in the boundary layer flow. Note the rectangular cross-section of the structure, which makes the sensor sensitive to only the streamwise flow direction.	46
20	View of the sensing pillars with marked tips, under LED light.	47
21	Schematic of the setup for pillar tracking	48
22	PIV snapshots in multi-exposure mode showing the development of the flow structure from the gust generator, as seen from the camera in the two different planes.	49
23	PIV snapshots showing the development of a flow structure from the gust generator, as seen from the camera normal to the wing plane. The vector plot is overlaid with sectional streamlines and the grey areas indicate regions of reduced streamwise velocity magnitude (in steps of 20%). Non-dimensional time is $t^*=0.1$, $t^*=0.27$ and $t^*=0.48$	50
24	Same as in Fig. 23, however when seen in the cross-section from the camera underneath the tunnel. Non-dimensional time is $t^*=0$, $t^*=0.1$ and $t^*=0.2$	51
25	Sketch of the starting vortex after flap deployment, which is shed into the wake, forming a horse-shoe type vortex (derived schematically from the PIV results in the different cross-sections).	51
26	Quiver plot of pillar tip displacement at the instant $t^*=0.7$ when the flow event moves over the pillar array after flap deployment (mean pillar deflection subtracted, maximum quiver length equals a tip displacement of 1mm).	52
27	Exploded view sketch of two hair sections sandwiched between 3D printed aerofoil sections. Not to scale.	56
28	Sketch of the whole sensing model. Not to scale.	57
29	Photo of the sensing pillar array, with marked tips shown under green LED	63
30	Schematic of the movement of the pillars as outputted by the camera.	64
31	Schematic of the dynamic experimental setup in water with the gust generator.	65
32	Schematic of the dynamic experimental setup in water with the upstream cylinder.	66
33	Schematic of the static experimental setup in air.	67
34	Comparison of layered EBC view and quiver plot	68
35	Enlarged view of one pillar probability density location, with red arrow to indicate flow direction.	69
36	Graph showing the variation of Strouhal with Reynolds for a cylinder	69
37	Two raw images of data as shown from the camera in Metavision, taken 0.2s apart, showing flow retardation.	70

38	Raw image of data as shown from the camera in Metavision, with pillar phase difference in columns highlighted with green lines. The red arrows indicate oscillating flow direction in a singular plane.	71
39	Schematic of the side view of the wind tunnel setup.	73
40	Setup image with both laser and camera visible of the wind tunnel.	74
41	Frequency map of wind hairs in the wind tunnel, with a colour bar below.	75
42	Time series plot of the first hair, with calculated frequency shown.	76
43	Shortened time series plot of the first three hairs.	76
44	Normalised velocity convection between hairs, with sensing aerofoil overlaid. Not to scale.	77
45	Schematic of the top, open surface of the water tunnel, with test section and flow direction highlighted. (Please note this is not to scale).	88
46	Graph with linear trend line fitted showing the variation of freestream velocity with pump hp. Dots represent data points, dashed line is a trend line	89
47	Graph to show the variation of pillar tip deflection with freestream velocity	90
48	Damping curved average across chordwise pillars with a trend line fitted.	90

List of Equations

1	Stoke equation	34
2	Particle relaxation time	34
3	Non-dimensionalised time	48
4	Strouhal number	70
5	Water tunnel capacity	88
6	Underdamped oscillator	91

Nomenclature

α	Phase
γ	Damping coefficient
μ_f	Dynamic viscosity of fluid
ω_1	Sinusoid frequency
ρ_p	Density of particle
2D	Two dimensional
3D	Three dimensional
A	Amplitude
AC	Aerodynamic centre
AoA	Angle of attack
AR	Aspect ratio
BAE	British aerospace
C	Chord
CAA	Civil aviation authority
CAGR	Compound annual growth rate
CFD	Computational fluid dynamics
d_p	Diameter of particle
e	Exponential
EBC	Event-based camera
f_n	Natural frequency
FFT	Fast fourier transform
fps	Frames per second
GB	Gigabyte
GPS	Global positioning system
hp	Horse Power
l_c	Characteristic length
LED	Light emitting diode

PIV	Particle image velocimetry
Re	Reynold's number
RMS	Root mean square
Stk	Stokes number
t	time
t_p	Particle relaxation time
TR-PIV	Time resolved particle image velocimetry
U_∞	Freestream velocity
UAV	Unmanned aerial vehicle
UK	United Kingdom
x	Displacement
x_0	Initial displacement

1 Introduction

1.1 Thesis Layout

The following thesis is for a PhD by publication, as such the publications are two separate chapters, with the final chapter being a prospective publication. A critical review section follows each paper at the end of the chapter.

List of Publications

- Court, A., Selim, O., Pamment, K. and Bruecker, C. (2023), "Design and implementation of spanwise lift and gust control via arrays of bio-inspired individually actuated pneumatic flaplets", International Journal of Numerical Methods for Heat & Fluid Flow, Vol. 33 No. 4, pp. 1528-1543. <https://doi.org/10.1108/HFF-01-2023-0046>
- Court, A.; Bruecker, C. Fly by Feel: Flow Event Detection via Bioinspired Wind-Hairs. Fluids 2024, 9, 74. <https://doi.org/10.3390/fluids9030074>

List of Conference Papers

- Court, A., Pamment, K. and Bruecker, C. (2022), "Spanwise Lift and Gust Control via Arrays of Bio-inspired Individually Actuated Pneumatic Flaplets", 56th 3AF International Conference AERO2022, Toulouse
- Court, A. and Bruecker, C. (2024), "Event Based Cameras: A Comparative Study For Fluid Event Detection", 21st International Symposium on Applications of Laser and Imaging Techniques to Fluid Mechanics, Lisbon

Unpublished

- Event Based Cameras: A Comparative Study For Fluid Event Detection (Extended version)

1.2 Introduction

People have often looked to the natural world for inspiration, often looking at the sky and natural fliers in awe. Our history is filled with mythology and literature depicting winged beings. Perhaps one of the most famous being the story of Icarus, whose father built him wax and feather wings to be able to fly to freedom but he flew perilously close to the sun and the wax unfortunately melted [1]. In the 15th Century, Leonardo da Vinci, sketched his design of a "helical airscrew", [2], we recognise this as an early attempt at a helicopter, however it lacked adequate propulsion. He is regarded as one of the first engineers to study the mechanics of flight, based on what he saw from bats and birds. His most famous work, an ornithopter, was a sketch of a human-powered aircraft that flapped its wings.

In much more recent history, the Wright brothers are generally accepted as the first people to sustain fixed-wing powered flight. The brothers both took flight during multiple test runs on December 17th 1903 in their Wright Flyer, the tests were a success, covering around 50m at a 3m altitude, [3] and gave way to a very famous photo, see Figure .



Figure 1: The first flight in the Wright Flyer on Kill Devil Hills [4]

The Wright brothers developed three-axis control, they understood the mechanics of flight by looking at how birds turned or banked during flight. This innovative development allowed for improved stability and manoeuvrability during their powered flight [5]. Their breakthroughs spurred on a new era of technological advancement and paved the way for modern flight as we know it.

More recently, designers and engineers have also looked to nature for inspi-

ration. Many companies have nature-inspired concepts.



Figure 2: Airbus's 'Bird of Prey' concept [6]

Current designs can also be optimised with bio-inspired ideas. Both Airbus and Boeing have used OptiStruct (part of CAE software suite Hyperworks by Altair), a software that lets engineers redesign components the way nature would, based on certain input parameters. This is a relatively new field, called morphogenesis, that is based on nature-based algorithms and allows for more natural and organic structures to be designed, [7] For example, trees form extra cells in such a way that resists bending that the tree would experience naturally, and the bones of birds have complex internal structures that allow them to be light but strong [8]. The software, OptiStruct, allows the user to upload a mature design, as well as the performance and load constraints, and then redesigns based on the growth pattern of bone, leading to a lightweight design. This idea, of looking to nature to improve our engineering designs, is being taken up by many research groups, with the aim of creating lightweight structures. [9] imitated the helical laminar structure found in the rods of mantis shrimp by layering thin layers of carbon fibre and epoxy composites and analysed their complex failure rates.

Another novel concept was that of BAE's 'smart skin' for use on aircraft, which contained thousands of microsensors integrated into the skin and stretched over the aircraft. The idea behind this skin was to be able to make a platform 'feel'; in the same way that people and animals can 'feel' their surroundings. The concept suggested that the skin could measure parameters such as; velocity, GPS, temperature and hull strain in not just localised areas but also be able

to recognise patterns in the measurements [10] Whilst this concept is nearly 10 years old, it shows the desire for novelty thinking when it comes to design and integration for engineering improvement.

Many of the bioinspired engineering material concepts and practices base themselves on being high-strength and lightweight. Similarly, the large-scale bioinspired systems, such as the 'smart skin' concept predict that they will be able to improve aircraft efficiency by being able to feel the surrounding flow and react accordingly precisely. The aviation sector must welcome any weight reduction or flight efficiency improvement, as it is well known that aircraft produce a range of greenhouse gases that directly contribute to climate change, the CAA also welcome these novel technologies [11]. The UK set a target to reduce greenhouse gas emissions by 80% in 2050 compared to 1990 and have current net-zero plans by 2050 [12].

Another novel concept is that of using pneumatic systems of aircraft wings either in place of hydraulic and electrical systems or as a basis for wing morphing. A pneumatic system is typically easier and cheaper to maintain compared to a hydraulic system, as it is a 'cleaner' system, not filled with oil. Using a pneumatic system on a wing also allows the stagnation point pressure to be tapped into for an easy source of high-pressure air. Pneumatics have been developed and tested for sweep control on small-scale UAVs in [13] and variable AR in [14], amongst other applications.

Using pneumatics leads to fully morphing wing structures or baromorphing wing structures. Many researchers are exploring the use of morphing wings, with a short review given in [15], where they found that actuation and sensing were lagging behind in wing morphing. Shape morphing elastomers, such as [16], where a silicone material has been developed that is pressurised and changes shape completely, could pave the way to a fully morphable wing structure. It is these new and novel techniques that engineering requires to meet future targets.

There are general flow systems for circulation control, many of which have been implemented on aircraft for decades, however these systems could benefit from such novel technologies. Spoilers tend to be on the suction side of a wing and towards the trailing edge. They extend upwards when required, where they purposely reduce lift by stalling the wing after the spoiler. Typically, there are two uses for spoilers, the first being to control roll or descent rate during flight and the second being to increase drag on landing, (roll here is rotation about the axis that runs nose to tail, pitch is rotation about the axis that runs wingtip to wingtip and yaw is rotation about the vertical). Airbrakes are similar but are designed to increase drag without changing the spanwise lift distribution. Shape memory alloys have shown the potential to be used in aerodynamic spoilers, as a rapid and precise control mechanism via bistable alloy actuators, [17]. This new technology poses both optimal drag and downforce (currently applied to automotive spoilers) and an improvement in fuel efficiency.

Gurney flaps are also most typically seen in the automotive sector, however, they still have relevant applications on helicopters and wind turbines. They are small tabs at right angles to the trailing edge that deploy a very small amount (a few percent of the chord length). They increase the pressure on the pressure side, resulting in a decrease in pressure on the suction side and thus the boundary layer stays attached to the trailing edge. Whilst the maximum lift coefficient is increased, the drag coefficient also increases, especially at small AoAs. Recently, oscillating gurney flaps have been researched for use on wind turbine blades, [18], these flaps oscillate between the upper and lower surfaces during blade rotation. The current CFD findings show that beneficial vortex interactions occur, which then correct undesirable pressure distributions, leading to an improvement in lift force.

Segmented flaps are often used on aircraft trailing edges to allow for more optimum settings in more flight scenarios. These flap systems can be 'smart' systems in which smooth hinge lines and embedded actuators allow for drag reductions at off-design conditions. Studies of such systems are carried out to find layout optimisations and deflections, such as [19]. Variable camber wings also can work via deflections of flaps and allow for shape optimisation, research is currently looking at retro-fitting variable camber systems to segmented flap systems for long-range fuel saving potential, [20].

Engineers and designers must look for new solutions and improvements for flight control and efficiency. Currently, there are many aspects of research that provide exciting potential for future benefit. Much of this research builds on biomimicry and uses smart, morphing materials.

This thesis aims to better understand the dynamic flow control mechanisms that birds of prey possess via a specially developed model in Paper 1. In Paper 2, an array of flow sensing pillars will be improved and their abilities quantified via comparative measures. Finally the aim of Paper 3 is to assess the feasibility of the use of EBCs in place of traditional PIV cameras.

This thesis is a by-publication thesis; as such, there are three main sections that follow the three main papers: chapters 2,3 and 4. Each paper has its own introduction, methodology, setups, results, and conclusion section, as were published, followed by a critical review. These chapters are preceded by an introduction chapter (this current chapter) and followed by a conclusion chapter. Following this is a calibration chapter, as well as the references and appendices.

This page has been left blank to separate chapters

2 Paper 1-Design and implementation of spanwise lift and gust control via arrays of bio-inspired individually actuated pneumatic flaplets

Contents

2.1	Abstract	17
2.2	Introduction	17
2.2.1	Scope	18
2.3	Design and Construction of Spanwise Control Concept	18
2.3.1	Design Background	18
2.3.2	Construction	20
2.4	Water Tunnel Test	22
2.4.1	Experimental Setup	22
2.4.2	Actuation Control	23
2.4.3	Test Description	26
2.5	Test Results	26
2.6	Conclusions	28
2.7	Outlook	31
2.8	Critical Review	32
2.8.1	Paper Overview	32
2.8.2	Supplementary Infomation	32
2.8.3	Problems and Limitations	33
2.8.4	PIV Uncertanties	34
2.8.5	Future Work	34
2.8.6	Measurements for the future	36

2.1 Abstract

Covert feathers on avian wings can show dynamic pop-up behaviour in rapid succession as a reaction to turbulent gusts. The purpose of this paper is to understand the possible flow control mechanism induced during such dynamic motion cycles. A model aerofoil is designed with suction side spanwise control of rows of bio-inspired flaplets. A NACA 0012 aerofoil is equipped with a spanwise row of eight flaplets at 80% chord, connected to pneumatic actuators and can be deployed to max 15° in a prescribed open–hold–close manner. The model is placed in a water tunnel and flow measurements are done in the wake of the flaps during a cycle using particle image velocimetry. During opening, boundary layer flow is sucked into the void space between the wing surface and the flaplet, which induces backflow underneath the flaplet and traps the fluid inside. This fluid is expelled downstream during closure, which generates a forward directed jet as seen by the formation of a vortex-ring like structure with higher axial momentum. The entrainment of the jet leads to the re-energising of the boundary layer flow further upstream. This paper presents a furtherment of understanding of the action of pop-up feathers for separation control. The actuation of the bio-inspired flaplets shows a flow vectorising effect which can be used for active separation and gust control. In the case of incipient separation, flaplet action can act to re-attach the flow because of the jet entrainment effect.

2.2 Introduction

As technology advances, engineering and aviation seek ways to ever improve design, whether it be to better efficiencies or to discover new concepts of control mechanisms. The natural world has long since been looked at as an idea source and now, biomimicry models engineering design and production on the inspiration of natural processes. A system based on the ability that birds possess, allowing them to actively pop-up wing feathers during flight to change their aerodynamic parameters, has been developed at City, University of London [21] and will be the basis of this work. Biomimicry work has been carried out at City previously, investigating the dive pattern of a Peregrine Falcon [22] and the flight control due to wing morphing, using wind tunnel tests and high fidelity simulations on idealised models. Owl-inspired passive trailing edge flaplets have also been investigated at City [23] for aerodynamic and aeroacoustic benefits. While those flaplets have shown their benefit already as passive pace-makers to control non-linear instabilities in the boundary layer, the current study expands on the idea of using active control of such flaps near the trailing edge. This is to study the effect of opening and closing the flaps when initially aligned with the suction side of the aerofoil. Such motion patterns can generate successive suction and blowing into the wake, which might be of benefit to prevent incipient stall or to counteract gust-induced flow separation. As the concept is designed with multiple individual flaplets, it allows for spanwise control of such events, providing more complex patterns of response for UAVs. The global UAV market has steadily grown in recent years and is expected to continue

growing at a compound annual growth rate (CAGR) rate of 8.59 % for the period 2018 to 2026 [24]. This increase in new design and test concepts for small and medium UAVs requires new UAV technologies, such as variable spanwise lift control for high-speed manoeuvres. Additionally, high altitude, extreme endurance and ultra-large wing span concepts need improved testing methods for spanwise gust control functionality. More complex gust patterns with varying spanwise intensity or wind direction, or with travelling wave characteristics are difficult to implement in the wind tunnel under controlled conditions. Conventional gust generation in wind tunnels is often done with a heaving wing or by two oscillating wings as in [25], temporarily redirecting the airflow to create an effective change in the angle of attack downstream. The current concept is not comparable to a morphing wing with a smooth trailing edge, as it is using flaplets on a rigid body aerofoil. It can be seen as an intermediate step for fixed-wing structures to achieve improved control functionality. Fully flexible structures were investigated in [26], where complex spanwise camber variation was achieved without gaps and discontinuities. Another project that showed the benefits of a fully morphable wing was [27], in which twist morphing wings were found to be more energy efficient during roll control. The project is therefore put into context with the aforementioned papers.

2.2.1 Scope

The paper states, discusses and explains the design process and the initial testing of a finite wing section with 8 pneumatically actuated suction side flaps. The pneumatic control permits fast flap response time, whilst the independently controllable flaps allow for spanwise flow variation. The effective performance of the spanwise flaps is analysed via particle image velocimetry (PIV) of the downstream wake section. The main objective of the project is to produce controllable and repeatable flap action and study the responsive flow pattern in a flow tunnel (water channel) to gain further knowledge of the interaction with the flow along the aerofoil and in the wake. Furthermore, the pneumatic model is tested for its use as an upstream device to generate controlled disturbances with complex spatial-temporal patterns, to be used for later measurements.

2.3 Design and Construction of Spanwise Control Concept

2.3.1 Design Background

The control concept was originally developed from the finite spanwise lift control concept described in [21]. The design sought to adapt the circulation distribution along the span, using individually controllable pneumatically actuated flaps. The resultant model is currently being researched as an upstream gust generator, to produce fast response, and repeatable and consistent flow disruptions, which can be controlled in their spanwise phase and amplitude individually.

The model consisted of removable trailing edge sections that each contained

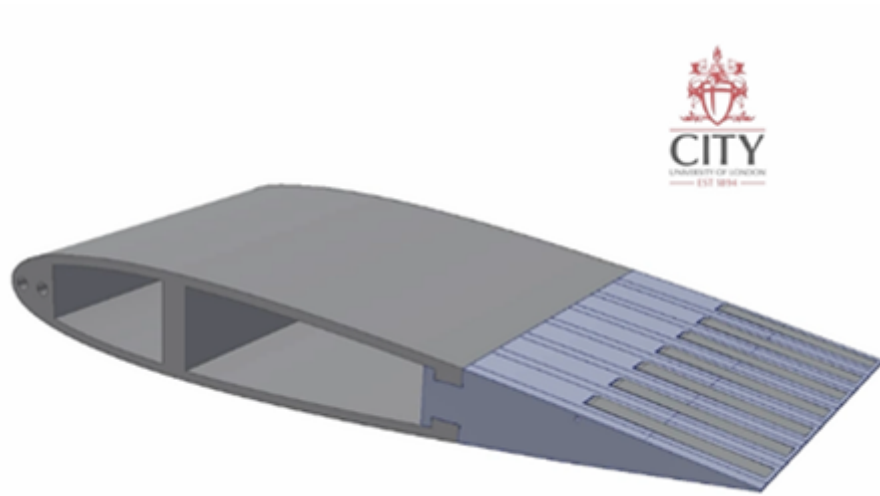


Figure 3: NACA0012 aerofoil model with individual pneumatically actuated spanwise trailing edge flaps concept. The model consists of 8 single segments in the spanwise direction, which each has a flap to be actuated with a controlled opening-closing cycle.

a pneumatic actuator and flap, allowing for the flaps to be repeated in the spanwise direction, shown in blue in Figure 3. Each trailing edge section could slide along the aerofoil section. This design allowed for ease of access and thus improved reparability of each section. The use of a pneumatic system was inspired by work such as [16], wherein mesostructured elastomer plates underwent fast, controllable, and complex shape transformations, at the application of pressure. Also, for aerofoil applications, there is always a constant source of high-pressure flow from the bypass of the engine or from the stagnation pressure which can be used for any pneumatic control system, meaning that a compressor is not needed in this system. The use of pneumatics in this project can allow for full baromorphing structures in future work, utilising the same pneumatic system. For this project, it was chosen to use inflatable air cushions as actuators, which control the deployment motion of the flaplets. For ease of use, we applied latex balloon catheters (Latex Nelaton Ballonkatheter, Balloon volume 5-10ml Praxisdienst GmbH & Co KG, Germany) as they were a ‘readymade’ solution to the problem. During the flap deployment, an elastic rubber band is stretched inside the cavity, which ensures to return of the flaps towards the original position flush with the wall when pressure is reduced again to ambient. This ensures a quick return towards the original position.

2.3.2 Construction

The flaps to be tested were based on a NACA0012 aerofoil of chord length 30cm and a finite span of 40cm. The trailing edge flap sections each had a span of 1.6cm and began at 64 % chord length from the leading edge. Both the aerofoil section, as shown in grey in Fig.1 and the trailing edge sections, shown in blue in Figure 3 had a 5mm diameter hole through them. This allowed for a threaded bar to be inserted and nuts to be added at either end to hold the sections tightly together. The nuts were recessed into capped end sections of span 8mm. A steel mounting section was manufactured and fitted into the top cap, to allow for the model to be mounted onto the traverse in the water tunnel, see Figure 4.



Figure 4: Top end plate, shown with mounting piece fitted and recessed fittings. The mounting piece is the support for the sting as a stable connector to the traverse in the tunnel.

The model utilised 3D printed sections to allow for ease of manufacture, assembly and repairability. All the trailing edge pieces are slotted into the front portion of the aerofoil and can be removed individually.

The trailing edge sections were designed with a slot in for the balloon to sit into and one solid side wall, to stop the balloon affecting its neighbouring balloon at maximum inflation. The flaps were made from formed mild steel and included a soft soldered bush and pin hinge mechanism to fit into the trailing edge piece. Upon inflation, the balloon causes the flap to pivot around its hinge and move into the open position, see Figure 5. When the pressure is reduced back to ambient pressure, the flap closes due to the elastic recoil forces of a rubber band, which is attached at the inside end of the flap and also to the segment. Specialist fittings were manufactured from brass to mimic the tip of a syringe to allow connection to the Festo pressure lines (Festo Automation Solutions, Esslingen, Germany). This ensured the pressure lines to be securely connected to the balloon catheters.

The control of the pneumatic system is shown in Figure 7, as a schematic

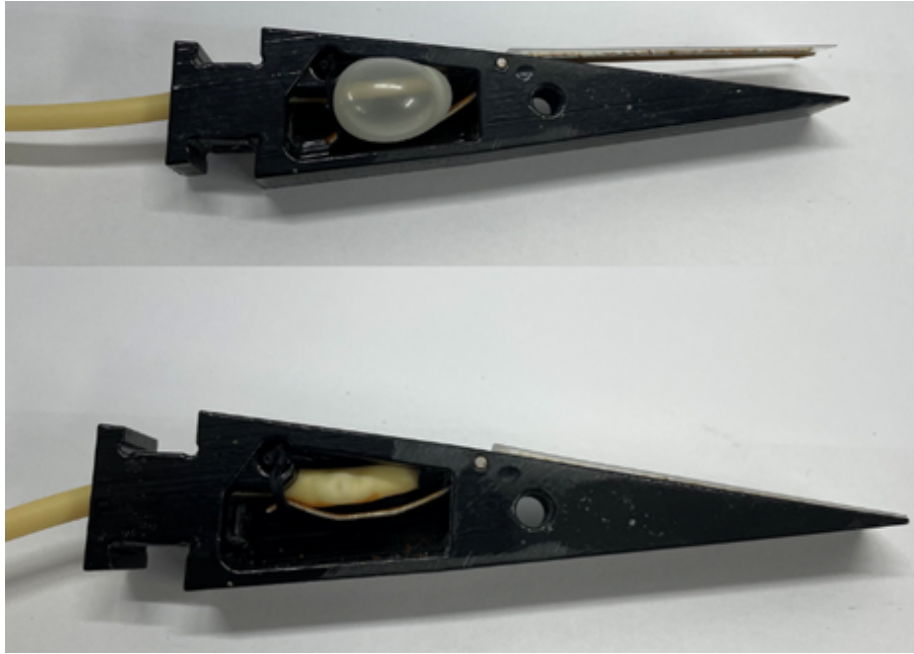


Figure 5: A single segment of the aerofoil with the balloon inside. Top: the inflated situation with the flap deployed. Bottom: deflated position as the reference situation with the flap flush with the trailing edge.



Figure 6: Balloon-to-pressure line fitting, using the typical syringe-type Luer cone connector used in medical devices such as for the balloon catheter in use.

diagram. The pneumatic valve system referenced was developed in a previous joint DFG project together with the IME1, RWTH Aachen. It was used herein alongside an Arduino board to control the opening and closing of the individual valves in the valve block, and therefore individual flaps. The regulator, valve block and pressure pipes used were also from Festo.

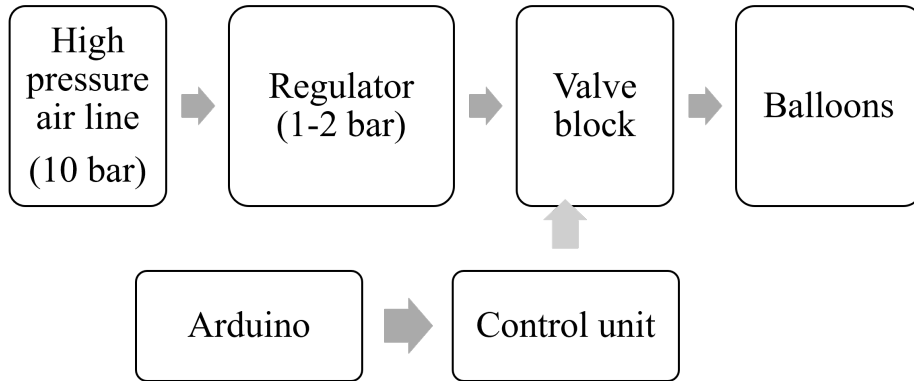


Figure 7: Schematic control diagram of the pneumatic control system.

Further iterative design improvements led to a few modifications to the design of the model after the construction phase. One such was to add thin, laser cut, Perspex sheet strips to the flaps, adhered with doubled sided tape. This ensured each of the flaps spanned the entire width of each individual trailing edge segment, thus creating less flow disturbance due to gaps between the flaps in the open position when run in parallel for several segments.

2.4 Water Tunnel Test

2.4.1 Experimental Setup

The model, as described in the previous section, was tested for downstream disturbance in the water tunnel at City, University of London, see Figures 8 and 9. A constant flow speed of $U_0 = 5\text{cm/s}$ was used, corresponding to a chord Reynolds-number of $Re_C = 15 \times 10^3$. The flow was suitably seeded with silver coated ceramic particles of diameter $80\mu\text{m}$ (Hart Materials Limited, Tamworth, UK), used as tracer particles. The goal was to capture clear PIV results of the immediate flap and downstream wake and to quantify the effect of the flaps actuating. A 3mm LED light sheet (IL-105/6X Illuminator, HardSoft, Germany) was used to illuminate the flow around the 5th flap in the horizontal plane. The recordings of the flow were taken with a high speed camera (Phantom Micro M310) mounted underneath the tunnel, pointed towards the LED light sheet via a mirror mounted at 45° (recordings at frame rates of 300fps, format 1280x800 px). Recordings were taken with different focal lengths, a larger field

of view with $8 \times 12 \text{ cm}^2$ was taken with a 100mm focal length and a zoomed-in view with $4.5 \times 6 \text{ cm}^2$, using a variable focal lens. As displayed in 8, the model was mounted at $\text{AoA} = 0^\circ$ in the centre of the tunnel in all axes, for initial testing. The traverse was then moved, moving the model upstream, allowing for PIV recordings to be taken at different locations downstream of the aerofoil.

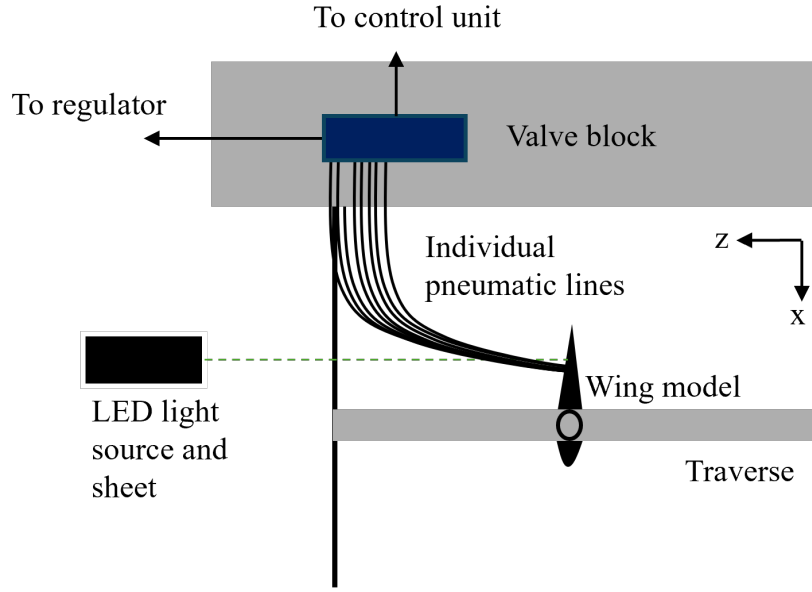


Figure 8: Schematic of the experimental setup in the water tunnel, top view. Flow is in negative x-direction from bottom to top.

2.4.2 Actuation Control

The flaps were individually controllable via an Arduino board and Arduino IDE software connected to the valve control unit, see Figure 10. The Arduino code outputted the instructions to the control unit and then therefore the valve block, regarding the pattern and opening or closing of each valve (total number of 20 valves). The valve block had high-pressure air supplied via a regulator from a 10 bar pressure line input. The opening of a valve allowed a specified balloon to inflate, and the closing allowed for ambient pressure to return and the balloon to deflate. The typical opening time of a balloon is about 200ms, similar to the closing time by the recoil action of the rubber band. To avoid bursting the balloons, the time of high pressure is limited to about 1s in the current configuration. A time extension was possible by running the valves in an oscillating pattern with repeated short valve closing-reopening cycles. This keeps the flaps in their fully deployed configuration with only marginal motion and decreased risk of balloon failure.

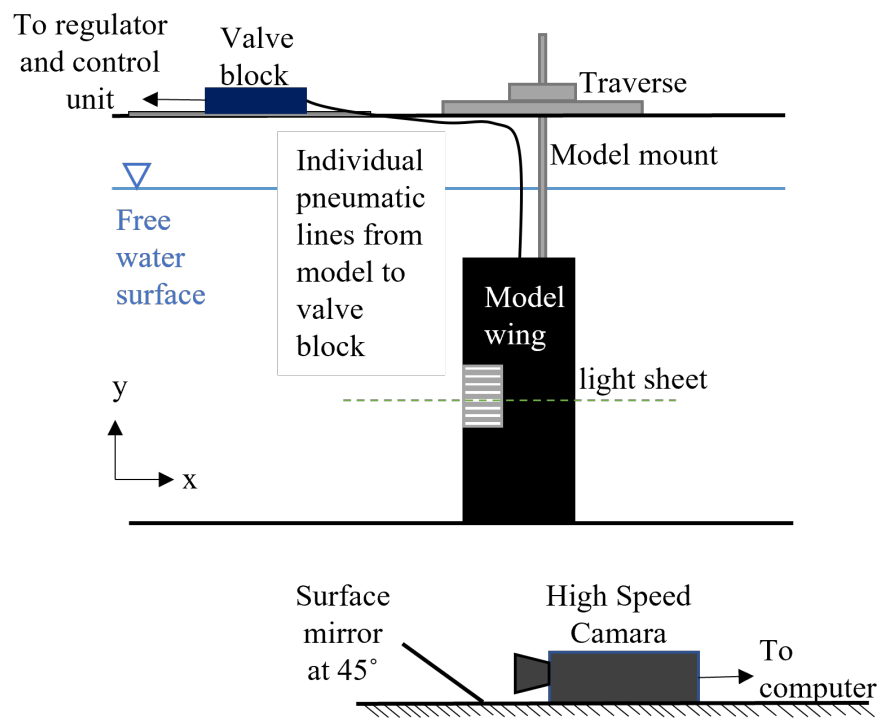


Figure 9: Schematic of the experimental setup in the water tunnel, front view. Flow is in negative x-direction from right to left.

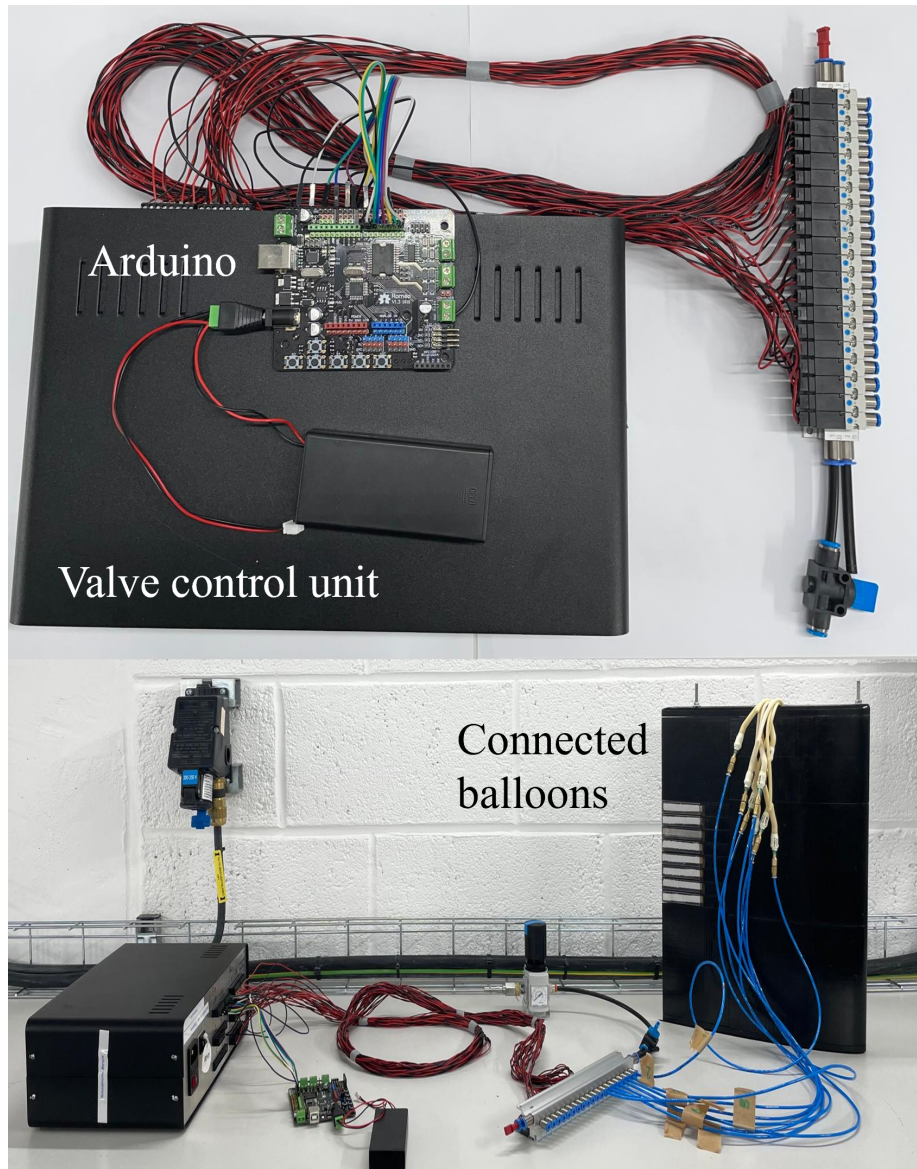


Figure 10: Valve control unit with Arduino controller (top) and shown in the lab with pressure lines connected to the balloons in the aerofoil (bottom).

2.4.3 Test Description

The Arduino board was programmed to run different flaplet patterns and duty cycles. As a reference, one of the tested patterns was all flaps up (flaplets 1-8), hold for 1s and then down again, whilst capturing live images. Another pattern was two flaplets at the centre up (4 & 5), two down on each side (2 & 3, 6 & 7) and the outer (1, 8) up again. This resembles a spanwise wave-type actuation pattern.

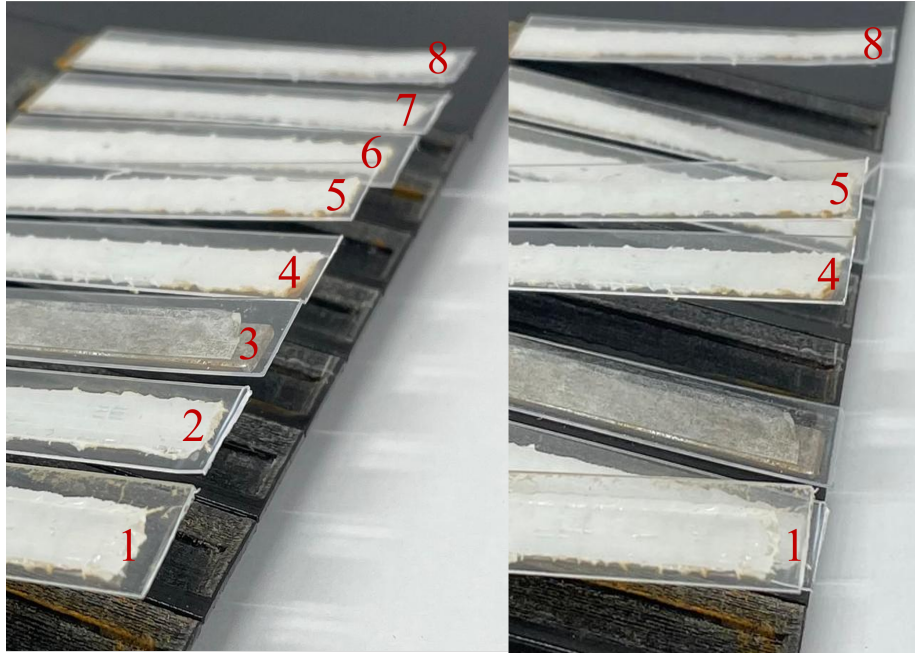


Figure 11: Typical flap actuation patterns used in the control tests. All open (left) and simulation of a spanwise wave pattern with 1,4,5,8 open (right).

A picture of the complete setup with the LED light illuminating the plane of the 5th flap is shown below in Figure 12, illustrating the overall arrangement of the measurement equipment together with the control unit on top of the tunnel.

The PIV recordings were taken at different distances downstream of the trailing edge to investigate the history of the flow pattern generated by the flaps. Meaning different runs of the experiment were carried out with the model moved upstream in 7cm steps, via the traverse. The optical camera setup remained in its original position.

2.5 Test Results

Initial tests of the wake pattern for the actuation of all flaps simultaneously are shown by flow visualisation pictures in Figure 13 during the cycle of a single

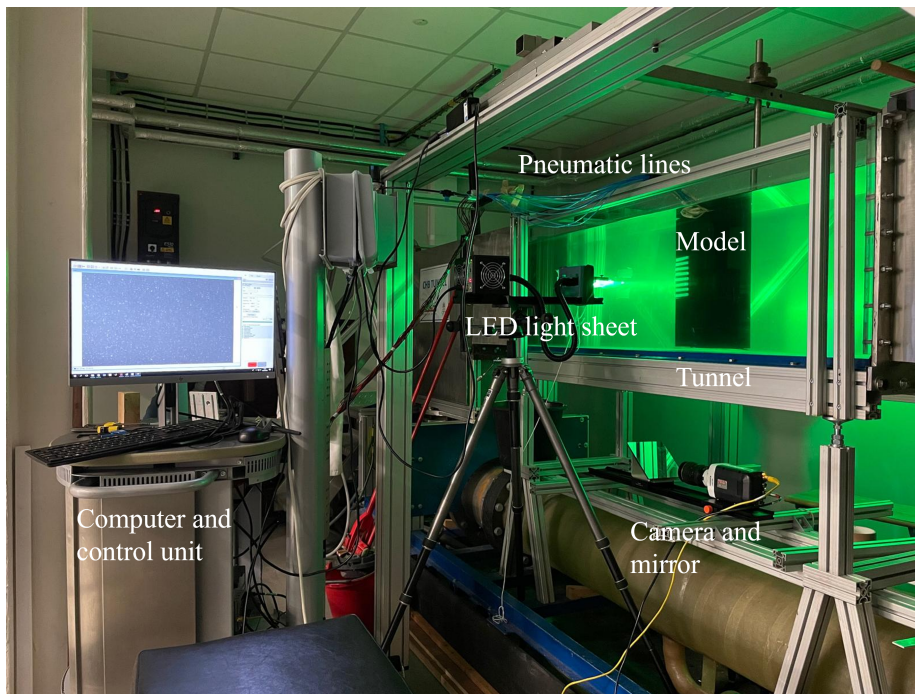


Figure 12: Picture of the water tunnel with the model inside and the optical setup for PIV measurements with LED light from the left and camera looking from the bottom.

sequence of opening and closing of the flaps. Those pictures are generated from the recorded image sequences, taken for Time-Resolved Particle Image Velocimetry (TR-PIV). The light sheet is positioned along the mid-section of the 5th flap in the horizontal plane. During the flap opening, a starting vortex is shed from the tip of the flap, while suction flow goes inwards into the void between the flap and the trailing edge. During flap closure, a portion of low-energy fluid previously entrained in the wake is expelled as a high-speed jet. According to Bernoulli’s principle, an increase in fluid velocity corresponds to a decrease in pressure. As the flap closes and generates a strong streamwise jet, the local pressure at the trailing edge decreases, which in turn accelerates the surrounding flow into the former wake region. This effectively displaces the wake downstream. The entrainment effect of the jet draws in fluid from both sides of the trailing edge, promoting further acceleration due to the induced pressure gradient. This acceleration persists until the wake begins to reform. Overall, the control cycle captures low-momentum fluid during flap opening and, through the kinetic action of the flap during closure, imparts energy to it. The resulting jet injects momentum into the trailing-edge region, disrupting the wake and enhancing overall flow stability through a localised increase in streamwise kinetic energy.

The current principle induces the momentum due to the squeezing effect, while the suction process entrains only fluid of low momentum from the near wake. The net effect is therefore argued to be helpful such as jet blowing, e.g. if local separation is happening.

Further downstream, the induced flow pattern evolves into a S-type flow disturbance, which is documented by the results from the TR-PIV measurements at a position of 0.5 chord length downstream of the trailing edge, see Figure 14. The early state of the wake is easily seen on the top of the figure, by means of the streamwise elongated shear layers left and right of the wake region, which slowly oscillates in the transversal direction with small amplitude. The opening-closing cycle generates a larger vortex in the wake (clockwise rotation in blue), which is seen by the disc-like blue region on the top of the image. This region moves further downstream and induces a sinusoidal modulation in the transversal direction (shown as the thick red line in the middle section).

The last stage of this sequence illustrates the disruption of the wake region that the cycle has caused. There is a region of low vorticity and rather homogeneous flow that continues after the wake of the aerofoil has re-established (not shown here).

2.6 Conclusions

The initial results presented herein show the feasibility of the pneumatic actuation principle of segmented flaps at the trailing edge for flow control. The action of the flaps is to capture low-momentum fluid from the near-wake region of the trailing edge during the opening phase, driven by the local suction in the increasing void between the flap and the surface. The closure phase then expels this fluid in the form of a tangential jet, which reenergises via entrainment of the

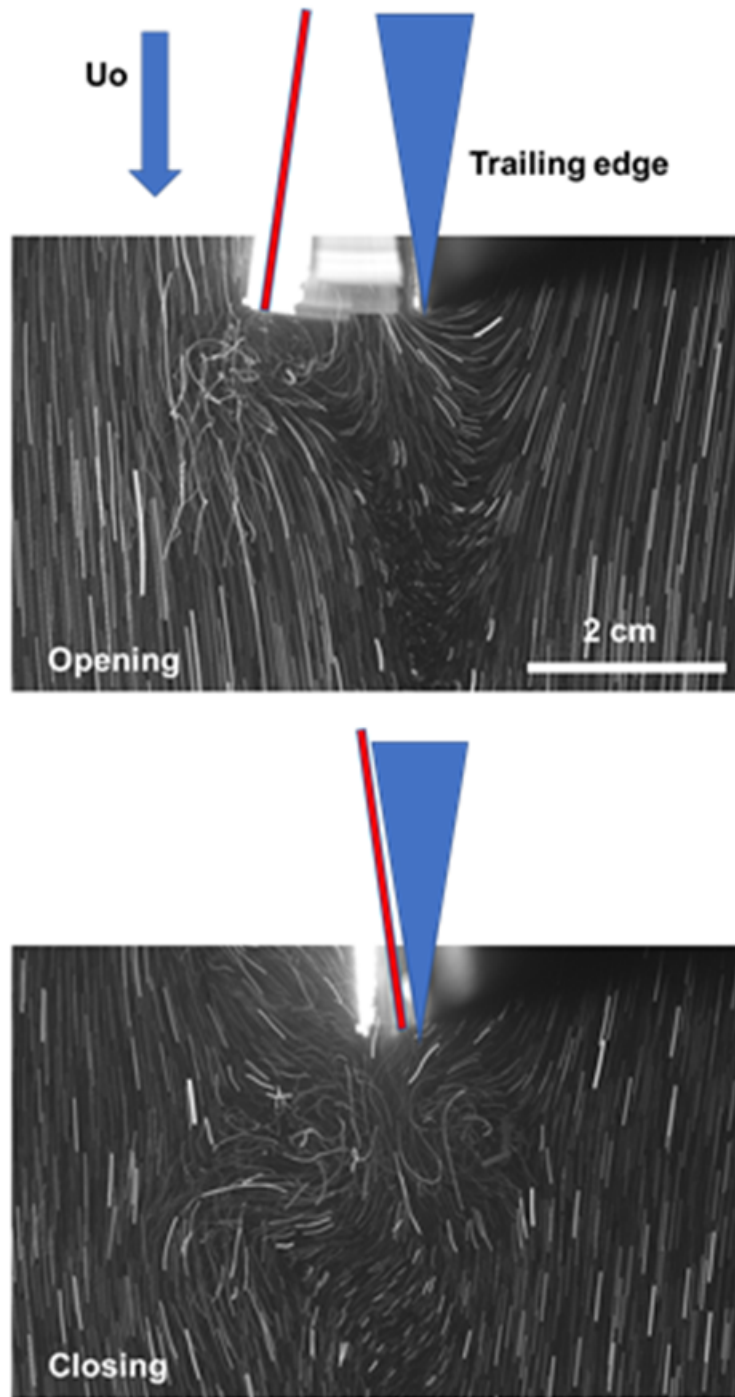


Figure 13: Flow visualisation using multi-exposed particle traces during opening and closing of the trailing edge flap row (the top figure has double the exposure time compared to the bottom).

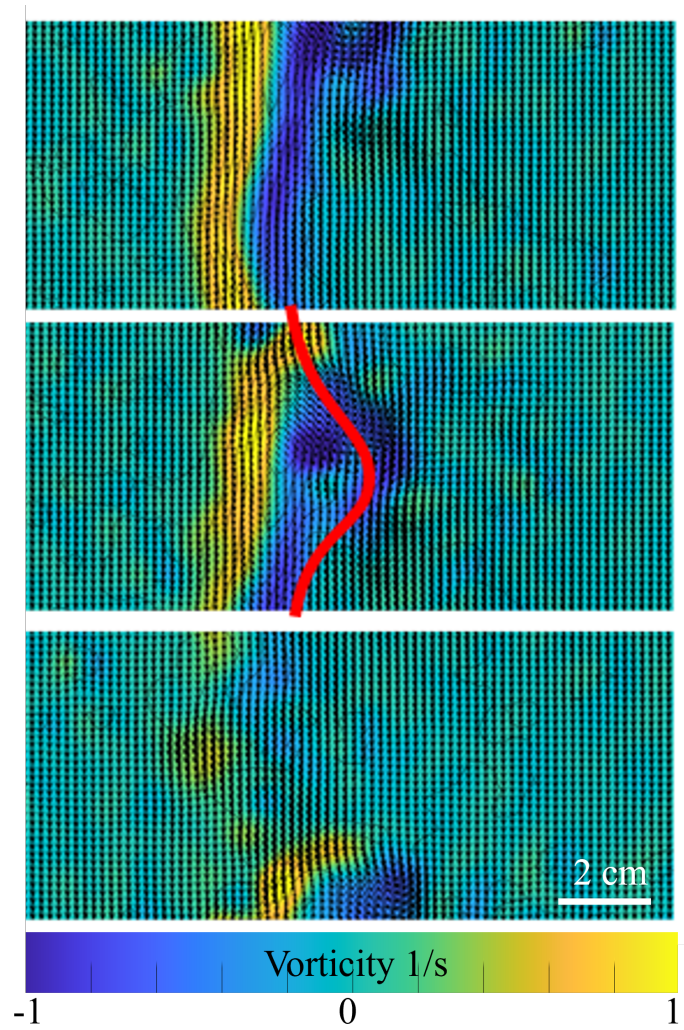


Figure 14: Velocity vectors overlaid on the colour-coded vorticity field (rainbow colour distribution) for three successive time-steps of the flow, 0.5 chord length downstream of the trailing edge after flap action. (Flow direction is from the top to the bottom).

fluid near the trailing edge and interrupts the wake. The first tests were done at an $\text{AoA} = 0^\circ$, which affected mainly the wake region. Further investigations will focus on the effect of increasing AoA and local interaction of the flap on the suction side with the outer flow near the trailing edge, especially for the purpose of lift control. In addition, the flaps may help to interrupt the growth of separation bubbles on the aft part of the aerofoil by preventing upstream transport and re-energising the boundary layer by the tangential jet formation. The current configuration at $\text{AoA} = 0^\circ$ is further used for the generation of controlled gusts in an upstream position away from test objects such as aerofoils or bluff bodies, testing their response under complex gust situations. The design allows for spatial-temporal patterns under controlled and repeatable conditions.

2.7 Outlook

The concept using the flaplet actuators shows promise for beneficial flow control on the basis of the observed flow manipulation near the trailing edge, (suction of low momentum fluid from the trailing edge near the wake and successive tangential blowing into the wake). Further studies are required to test for lift-generating configurations for higher AoA and the modification of the flow by the flap action in such circumstances. In addition, different patterns of duty cycles (opening time – fully open -closing time) will be investigated to find the optimum parameter for different control aspects, such as prevention of separation growth, or interruption of the wake relative to the characteristic time-scales of these flow formation features. In addition, different sequences of flap action need to be tested for their suction and jet formation efficiency. A single flap has a larger percentage of the amount of fluid entering from the side during opening and also during closing when part of the fluid is expelled along the side of the flaps. This effect depends on the number of neighbouring flaps, which have similar phases in the motion cycle. For the next stage of testing, more than one plane will be analysed using 3D Scanning PIV, allowing the capture of the flow in the complete cross sections behind all flaps in the row. The far-wake region of the current configuration with the S-type transversal flow is planned to be used for investigating the effect of such disturbances on stall cells. Therefore, the aerofoil will be installed in our wind tunnel upstream of the test section and will be equipped with pneumatic control to generate isolated gusts of S-type transversal flow patterns. Current research is working with an aerofoil equipped with near-wall micro-pillar flow sensors to capture the interaction of these gusts with the flow over the wing.

2.8 Critical Review

2.8.1 Paper Overview

Paper 1 presents a novel method of actuation of suction side trailing edge flaplets, via off-the-shelf pneumatics. The design idea was based on previous work at City, University of London, based on bio-inspired passive trailing edge flaplets on a NACA0012 aerofoil. The previous work looked at arrays of passive flexible elements that were allowed to oscillate freely, at high frequencies, on the trailing edge [28]. The results were captured via TR-PIV measurements, and a good reduction in tonal noise was found. Paper 1 somewhat built on this idea but with the development of an active pneumatically actuated individually controllable setup consisting of eight trailing edge flaplets on the suction side. The opening and closing effects of these flaplets were studied via PIV in the water tunnel and the successive sucking and blowing effects into the wake were studied. These flaplets were based on the pop-up feathers that birds of prey have, as well as work carried out in our research group [29], that allow the bird to control flow separation.

2.8.2 Supplementary Information

Zero Angle Setting

The water tunnel used, has an above traverse, allowing for the x-direction setting of the model in the test section. The traverse is mounted centrally in the z-direction and the mounting hole is central to this, thus the model is central in the z-direction. However, since the flaplet model has its mounting rod around its AC, the model, even though it's mounted to the traverse, can spin freely about this rod. This results in a setup that makes it extremely difficult to determine where $\text{AoA}=0^\circ$ is. To overcome this a simple solution was developed and is shown in Figure 15.

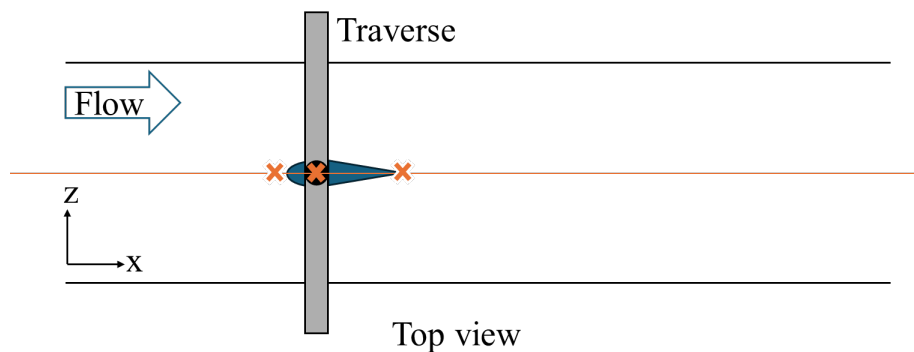


Figure 15: Schematic showing the setup to determine the zero AoA

The orange line in Figure 15 represents a piece of taut string, tied to points at

either end of the tunnel, centred on the mounting rod and traverse. The orange crosses represent plumb bobs that were used at the leading edge, mounting rod and trailing edge, this allowed for the model to be set at zero and firmly tightened to the traverse.

Other Balloon Volumes

This version of the flaplet model used off-the-shelf catheters for the pneumatic actuation. This was done to allow for easy, cost-effective and simple manufacture of the model. Catheters come in a range of sizes for varying applications, cardiac catheters were disregarded, as the balloon inflation diameter was too small. Urinary catheters were then chosen, for their much larger inflation diameter and the pressure they could exert on the internal flaplet mechanism. A French size, Fr, 12 was chosen, requiring approximately 10ml of air to inflate. Sizes range from Fr 10- 18, the larger sizes had too much lag time on inflation and the smaller sizes were easily burst.

2.8.3 Problems and Limitations

The following are some problems encountered during the testing for Paper 1.

Balloon Lifecycle

As the balloons were catheters, which are by design, single-use, there were some problems with the cycling of them (inflate-deflate). It was also found that UV and LED light increased the rate at which the latex cracked and degraded, this resulted in brittle balloons that easily burst. For the experiments in Paper 1, the balloons were replaced after every use and put away in a dark cupboard for storage. This was inefficient, so the actuation was redesigned for Paper 2.

Discontinuous Flaplets

As can be seen in Figure 11, the flaplets have a thin sheet of perspex glued to the outer surface to create a continuous surface. To stop the perspex catching on themselves, a gap of roughly 1mm was left between each flaplet. This then created a discontinuous suction side trailing edge surface, whilst it was not an issue for these experiments, it is an area to be improved upon. A complete flexible sheet could be used to cover all the flaplets to mitigate the gaps.

Corrosion

Both the flaplet and the hinge pin were made out of mild steel, unfortunately, this resulted in the flaplet surface corroding after use in the water tunnel. Not only did the corrosion look unsightly but it also caused material swelling around the hinge pin, which increased the friction in the hinge. This meant that occasionally the flaplets would get stuck in a position, requiring the model to be stripped down and the hinge pin lightly sanded. Between Paper 1 and Paper 2, the flaplets and hinge pins were remanufactured from aluminium. Whilst this did solve the problem, it is not the ideal solution, as they are still prone to

corrosion. Stainless steel would be even better, as that will be extremely inert to the conditions.

2.8.4 PIV Uncertainties

Detailed below are some sources of uncertainty that arise from PIV.

Stokes Number

Stokes number is the measure of how closely the tracer particles follow the flow for given conditions and can be defined as follows in Equation 1.

$$Stk = \frac{t_p U_\infty}{l_c} \quad (1)$$

Where t_p is the tracer particle relaxation time, U_∞ is the freestream velocity and l_c is the characteristic length of the model in the tunnel. The relaxation time of the particle can be calculated as shown below in Equation 2.

$$t_p = \frac{\rho_p d_p^2}{18\mu_f} \quad (2)$$

Where ρ_p is the density of the tracer particle, d_p is the diameter of the tracer particle and μ_f is the dynamic viscosity of the fluid.

Using these equations and the tracer particle properties, as found on the manufacturer's website (Hart Materials, Tamworth, UK), the Stokes number is around 0.005, meaning that the tracer particles closely follow the streamlines and accuracy errors are below 1%.

Integration Windows

Using a reference scale image, the px/mm was determined to be 7.14, with a time step of 3.3ms between images.

2.8.5 Future Work

Detailed below are some different directions that this work could take for future investigation.

Morphing wing

Whilst far off, this work presented in paper 1, could act as the initial stepping stone into a fully morphing wing. Classical designs for morphing wings tend to rely on heavy mechanical systems to 'morph' the wing into new shapes, usually via modifying twist or camber. [30] developed a morphing wing with elastomeric skin. Internally, the model contained servo motors that controlled telescoping tubes at four spanwise locations. They found that the twist enhanced the operating envelope of the AoA.

These mechanical systems often have such a weight penalty, that it tends to cancel out any real-world efficiency benefits they might bring. Pneumatics offer a more lightweight approach, the hardware required is just lightweight tubing to carry the high-pressure air to the method of actuation. No compressors or storage tanks may be necessary, as a wing has a constant source of high-pressure air at the stagnation point. The method of actuation here is a balloon, or later on, a small cylinder, which is very lightweight when compared to a mechanical cam system or hydraulic actuation.

There have been many advances in materials in recent years. Now it is possible to 3D print silicone elastomers, such as [16]. These baromorphing elastomers undergo fast-acting, controllable and complex shape transformations when pressure is applied through them. Such a material could be used for a fully morphing trailing edge section, where dependent on the location of applied pressure, the trailing edge could flex up or down across multiple spanwise locations. The benefit of using such material would be that the trailing edge would be a smooth continuous surface, compared to the multiple edges created by the flaplets.

Alternative actuation

If a morphing elastomer was used, piezoelectric actuation of the flaplets could be considered. As previously mentioned, mechanical and hydraulic actuation carry a significant weight penalty for all the hardware, however, piezoelectric materials could be a lightweight solution. Consider a morphing wing, with an outer elastomer skin, this skin could contain piezoelectric fibres at different chordwise and spanwise locations. If an electric current were to be passed through these fibres, then they would mechanically deform, thus changing the wing properties. Many researchers have studied piezoelectric actuation specifically for incorporation into aviation materials. A study of recent trends, [31], reports the benefits of such an idea, as the adaptive structures have high energy density, good stiffness coefficients and strain rates. The advantages of such materials and integration should motivate the development and testing of these smart materials on aircraft wings to improve efficiency.

Wingtip flaplets

It is well known that birds have wing tip feathers that they use to perform certain flight manoeuvres, as found in [32]. The slotted feathers that the birds have on their wing tips reduce induced drag and can reduce total drag by around 12%, a figure consistent with wing theory predictions when considering winglets. Work is also being carried out in our research group, looking into the effect of serrated wingtips, [33]. Flexible, 3D-printed, wingtip extensions have been tested on a NACA0012 at varying AoAs and it has been found that the wingtips dislocate the main tip vortex to reduce induced drag. This work has currently been with passive wingtips but has the potential for active wingtips, as well as smart material integration.

2.8.6 Measurements for the future

For the model described in Paper 1, it was found that, at $\text{AoA}=0^\circ$, the model can be used as a gust generator, where controlled gusts may be needed for other models to determine their response to complex flow situations. It was found that the opening and closing of the flaplets mainly affected the wake region and so could be used as an upstream gust generator. The initial results have been discussed but it is thought that the flaplets could benefit from further testing.

Lift control

The flaplets should be tested at other AoAs, using high-speed PIV measurements to study the potential that they have for modifying the spanwise lift distribution. It has been seen in other work that controllable wing flaps can be beneficial to flight conditions, [34] utilised multiple trailing edge flaps for drag reduction, by minimising induced drag, or to limit wing bending moment by changing the load distribution along the span. Similarly, [35] numerically determined the characteristics that allowed a trailing edge flap to improve lift at high angles of attack and studied the benefits that arose from the interaction of the flaplet and flow field. It was found that the flaplets could deliver a 20% increase in lift on a NACA0012 at AoA of 20° . If measurements were to continue, the use of 3D scanning PIV may be beneficial to provide detailed cross-section images. Another consideration for the future is the pattern of flaplet opening and whether different patterns may be needed. The flaplets are individually controllable, so if needed, only certain spanwise sections could open or close, this could be useful for modifying certain aspects of the spanwise lift distribution.

Flaplet positions

Similarly, the position of the flaplets on the surface can be investigated for relative effect. Moving the hinge location further forward, towards the leading edge, and further back, towards the trailing edge, and even such that the flaplets extend past the trailing edge, have possible benefits for flow control. The locations could be studied based on current aircraft segmented flap locations, under the same tunnel conditions as Paper 1.

Time scales

Testing the flaplets in the water tunnel allowed for a reduced rate of flow structure growth and development, due to the relative damping effects arising from the increased density of the water when compared to air. However, the relative time scale of the flaplet opening/open/closing cannot be altered, as it is a function of the pneumatic actuator. At a freestream speed of 0.35cm/s , the Re of the flaplet model in air is approximately 7000 and approximately 300k in water but the opening time of the flaplet stays constant at 250ms. In water, this means that the opening/closing timescale is too fast to compare to the same air velocity situation. Some future work needs to be carried out to investigate the possibilities and the effects that changing this time scale has and the relative comparison between air and water flow situations.

Real world applications

The flaplets can be scaled for use in a wide range of real-world applications. A key consideration in their implementation is the force required to actuate them. This opening force is influenced by several factors, including the properties of the working fluid, the desired actuation timescale, the dimensions and mass of the flaplets, and the mechanical losses within the hinge mechanism. Although these forces have not yet been thoroughly investigated, the use of pneumatic actuators—known for their scalability and capacity to generate significant force—suggests that achieving the necessary actuation forces is feasible. It is also known that wings have a source of high pressure at their stagnation point, this could be tapped into to provide the high-pressure air (or via an engine bypass), avoiding the need for heavy air compressors. Whilst this system could avoid compressors and storage tanks, it would be unlikely that a full pneumatic system is possible, the use of electronics would still be needed to control the opening and closing of the air valves. Such real-life applications could include: upstream gust generation for research purposes, spanwise lift control devices on fixed-wing UAVs for gust alleviation and increased lift at high AoAs.

Sustainability

Even small improvements in aerodynamic efficiency can lead to significant fuel and emissions savings over the lifetime of an aircraft, which will help the aviation sector reach its sustainability targets. Improvements such as drag reduction, enhanced flow control and lightweight novel designs are all steps in the right direction.

This page has been left blank to separate chapters

3 Paper 2-Fly by Feel: Flow Event Detection via Bioinspired Wind-Hairs

Contents

3.1	Abstract	40
3.2	Introduction	40
3.3	Materials and Methods	42
3.3.1	Disturbance generation	42
3.3.2	Experimental setup for PIV	43
3.3.3	PIV processing	44
3.3.4	Sensing pillars	45
3.3.5	Experimental setup for pillar tracking	47
3.4	Results	48
3.4.1	PIV Disturbance Characterisation	48
3.4.2	Disturbance sensing via pillars	52
3.5	Discussion	53
3.6	Conclusion	54
3.7	Critical Review	55
3.7.1	Paper Overview	55
3.7.2	Supplementary Information	55
3.7.3	Problems and Limitations	56
3.7.4	PIV Uncertainties	57
3.7.5	Future Work	57
3.7.6	Measurements for the Future	58

3.1 Abstract

Bio-inspired flexible pillar-like wind-hairs show promise for the future of fly-by-feel by detecting critical flow events on an aerofoil during flight. To be able to characterise specific flow disturbances from the response of such sensors, a comparison of quantitative PIV measurements of such flow-disturbance patterns are compared against the sensor outputs under controlled conditions. Experiments were done in a flow channel with an aerofoil equipped with a 2D array of such sensors when in uniform inflow conditions compared to when a well-defined gust is introduced upstream and is passing by. The gust is generated by the sudden deployment of a row of flaps on the suction side of a symmetric wing that is placed upstream of the aerofoil with the sensors. The resulting flow disturbance generates a starting vortex with two legs, that resembles a horseshoe-type vortex shed into the wake. Under the same tunnel conditions, PIV measurements were taken downstream of the gust-generator to characterise the starting vortex while further measurements were taken with the sensing pillars on the aerofoil in the same location. The disturbance pattern is compared to the pillar response to demonstrate the potential of flow-sensing pillars. It is found that the pillars can detect the arrival time and structural pattern of the flow disturbance, showing the characteristics of the induced flow field of the starting vortex when passing by. Therefore such sensor arrays can detect the "footprint" of disturbances as temporal and spatial signatures, hence allowing us to distinguish those from others or noise.

3.2 Introduction

In the natural world, it can be seen that many animals and insects have a variety of 'in-built' sensors, which they can use for flight sensing or event detection in both air and water. Bats are one example, they have hair-like structures that coat their wings, which have been the subject of in-depth research. [36] hypothesised and found that bats use these hairs to sense changes to the boundary layer profile to improve their stability and manoeuvrability during flight. Similarly, [37] found that the wind hairs had high sensitivity to reverse airflow to allow the bat to monitor instabilities during slow flight that could lead to separation. It should also be noted that bats are incredibly complex fliers, their wings containing many features that improve their performance, [32] and therefore rely on such sensors to remain in full control during extreme manoeuvrability. It is not only bats that possess these sensing hairs, seals also use sensing whiskers [38], in which oncoming flow direction and velocity can be felt by the dynamic responses of their whiskers. Rats are thought to have active whisker sensing abilities, [39], in which they may be able to control the relative velocities of their whiskers when using them to sense surfaces in their surroundings. This is an area of nature in which aviation can benefit once fly-by-feel can be realised, tactile whiskers have already proven that learning from these designs is useful [40] and [41].

Many researchers are developing and testing bio-inspired sensors for a vari-

ety of applications in engineering. A good overview can be found in the review papers by [42] and the most recent one by [43]. Such sensors have been developed based on optical, piezoresistive, piezoelectric and capacitive principles. With respect to air flows, optical sensors were developed by [44] in the form of flexible microscopic cantilever beam sensors for wall-shear stress measurements, allowing the optical detection of separation in complex turbulent flows. Other research has been done on sensors that could sense very low-speed air flow with directional sensitivity [45]. Research has also been done on piezoresistive hair-like sensors specifically for airflow sensing [46], in which the results showed that the response was proportional to the oncoming airflow velocity. Work such as [47] developed a flexible skin for a NACA0012 by mimicking biological systems. The flexible sensing skin could measure surface pressure, temperature and wall shear stress and has the potential to improve the capabilities that UAVs have both aerially and underwater. There is current interest in underwater MEMS sensors, for applications such as underwater autonomous vehicles [48], [49] and [50], the natural inspiration for these sensors tends to be fish that live in areas of very low light and have to rely on sensors for their surroundings. [51] developed and tested high-sensitivity neuromast-inspired flow sensors based on biological sensors that blind cavefish have for the navigation of underwater robots. Whereas, [52] developed and tested sensors on a biomimetic robotic stingray, where the sensors were successfully used to provide inputs to the robot that allowed it to track a given trajectory. In that sense, a fly-by-feel flight system based on bio-inspired hair sensors could improve the safety and reliability of flight manoeuvres in complex environments. In addition, such sensor arrays could also be useful for aerodynamic design studies in wind and water tunnels or to prove computational models.

In our lab, nature-inspired flexible pillar structures have been developed as biomimetic wind hairs and have already proven their ability for flow event detection and incipient stall monitoring([53]). The flexible pillar sensors work on the principles of flexible cantilever beams that are deflected by the flow-induced drag forces and as such allow detection of flow events by optically monitoring their dynamic behaviour. Similar strategies were also developed and reviewed for underwater flow sensing, based on seal whiskers [54], [55] and [56]. One benefit of such sensing systems is the potential for implementing those sensors into flow control strategies, which overall would allow reactions to critical flow situations by preventive measures, e.g. to prevent stall after sensing premature instabilities along the wing. In nature, we can see the benefits of morphing wings that can react to gusts or unstable flight conditions. Research has been done on the wing morphing ability of peregrine falcons during dive and pull-out manoeuvre, [22], thus improving their manoeuvrability in certain flight conditions. Morphing wing action can optimise drag performance in specific situations and also mitigate stall [40]. Furthermore, active flow control is possible through distributed flaplets on the wing and trailing edge, or leading and trailing edge morphability [57]. Those distributed flaplets can help to control the distribution of circulation and drag along the span in a sensitive way. Such a wing has been designed in our lab,[58], where the individually controllable flaplets mimic the

pop-up feathers that birds have. This concept has been used as a disturbance generator, where the flaplets open and close to create a gust-like disturbance and will be used in such a way again here. Integrating the sensors on the same wing paves the way for in-built flow monitoring, which could enable circulation management by feedback control through continuous flow monitoring. Such real-time feedback is possible by the advent of highly sensitive motion tracking cameras or event-based cameras, which offer real-time flow monitoring of the optical sensors.

The paper is structured as follows: after the introduction, the second chapter details the experimental methods and the wing modification with the actuated flaplets. The sensing principle is explained and integration of the sensors on a NACA0012 aerofoil is shown. Results of the experiments in uniform flow and with the induced gust are presented by means of the velocity fields and the response of the sensor array. A discussion and concluding remarks are given at the end.

3.3 Materials and Methods

All experiments were done in the low-speed water tunnel at City, University of London. The tunnel is open surface and has a clear test section of 1.5m length at a cross-section of 40cm by 40cm. Comparing similar Reynold’s numbers, flow studies done in the water tunnel, as opposed to the wind tunnel, allow for lower-budget experimental equipment but yield higher-quality PIV images. Typical flow speeds used were 35cm/s at a chord-based Reynolds number of 100k.

3.3.1 Disturbance generation

The disturbance generation was realised with a symmetric NACA0012 wing (chord $C1 = 30\text{cm}$) with four individually controlled pneumatically actuated flaplets, as previously developed in [58]. The pneumatic actuation has since been updated, from balloons to small pneumatic cartridge cylinders to overcome past repeatability concerns. The cartridges were from Festo (EGZ-6-5 Pneumatic Piston Rod Cylinder, Single Acting).

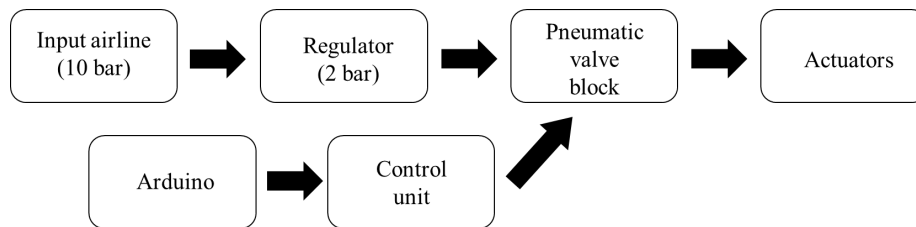


Figure 16: Schematic of the pneumatic system

As shown in the above figure, 16, the disturbance model was connected to a high-pressure air source and then regulated down to the required operating

pressure of the actuators of 2 bar. The flaplets were easily controllable via an Arduino board, where different buttons could be programmed to operate different flaplet duty cycles, by opening and closing the valves.

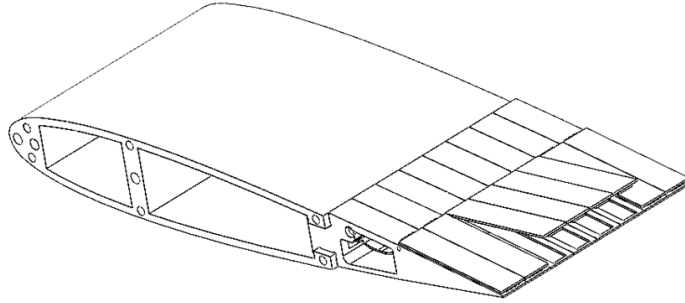


Figure 17: Schematic of the actuation

The flaplets had a clear rectangular section of thin acrylic sheet stuck on the suction side, to ensure there was a smooth and continuous flow surface. The above figure, 17, shows the middle four flaps open. For the gust disturbance generation, the four consecutive flaplets shown were opened, held for 1s and then closed, with the opening and closing phases around 250ms. The generated gust has the form of a starting vortex, which is shed from the trailing edge once the flaps have reached their maximum deployment position. A further description of the vortex is gained from the PIV measurements.

3.3.2 Experimental setup for PIV

The disturbance generator model explained above was set up in the tunnel such that the free ends of the model were against the lower viewing window of the test section and out of the tunnel at the free surface. The model was placed in the tunnel's centre to avoid wall effects. The flaplets are also centred in the channel flow to avoid the lower wall effects and the upper wave effects from the open surface. The camera used for all measurements was a high-speed Phantom M30, with the required section illuminated by a Dantec raypower 5000 5W continuous wave Argon-Ion laser ($\lambda=532\text{nm}$) with sheet thickness 1mm. Using a Tokina 100mm macro lens, the frame rate of the camera was a continuous 700fps, f-value of 2.8 with an exposure time of $1430 \mu\text{s}$ and window size of 1280x800.

To capture the disturbance generated in detail, two PIV setups were arranged. The first is with the light-sheet oriented in the horizontal plane, crossing the disturbance generator in the middle of the flap row that is to be actuated. The second setup uses the light-sheet in the vertical plane, parallel to the suction side and in line with the trailing edge. For both setups, there were two sets of images captured, the first at the trailing edge and the second at a half

chord (15cm) further downstream. This was achieved via a traverse that the gust generator model was attached to, while the recording setup remained in its position. A pre-mixed solution of tracer particles (diameter $50\mu\text{m}$) was added to the tunnel and allowed to mix thoroughly for an even seeding.

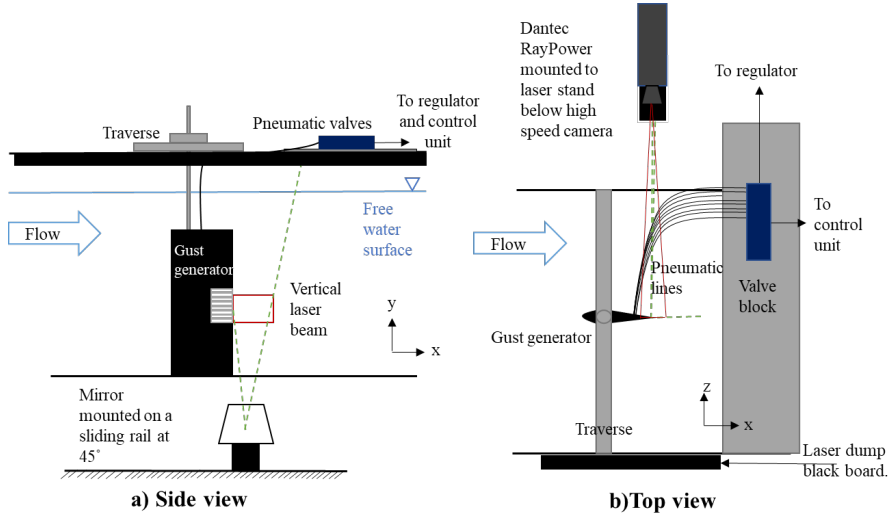


Figure 18: Schematic of the PIV setup for the measurements in the vertical plane (camera outside of the tunnel).

3.3.3 PIV processing

The recorded time series were processed using an in-house developed PIV processing toolbox written in Matlab. The code uses 2D cross-correlation between pairs of successive images in the time series. The time separation of the images is equal to the inverse of the recording frequency (700fps). A multi-pass algorithm is used which runs over two iterations across the images in small, decreasing interrogation windows with window-refinement (1st iteration 48×48 pixels, second iteration 32×32 pixels). The correlation peak is fitted with a 3-point Gaussian curve in x- and y-directions to achieve sub-pixel accuracy. Typical mean velocities result in displacements of between three and four pixels. Erroneous vectors were filtered out using maximum and minimum ranges of expected velocities and a local median filter. The vectors from those positions were interpolated from the nearest neighbours. A final 3×3 kernel Gaussian smoothing filter was run over the results to remove small-scale structures, highlighting large-scale coherent motion patterns.

3.3.4 Sensing pillars

Work was previously carried out by our team to develop and calibrate flexible pillar sensors in boundary layers down to a wall distance of 300 microns, where they acted as wall-shear stress sensors ([53] [59]). These sensors follow the principle of a one-sided clamped cantilever beam, bent by drag forces from the flow around the pillar. The measured signal is the tip bending between the wind-off and the wind-on situation. If the length of the pillar is small enough such that it is fully submerged in the viscous sublayer of the near-wall flow boundary, then this measure is proportional to the wall shear as the load profile is linear along the structure. Having a slender filamentous shape, these pillars mimic sensors seen in the natural world, such as wind hairs on bats [37] and have proven useful for the detection of flow events. Therein, the length of one pillar is of the order of the boundary layer thickness, which then integrates the forces along the length of the sensor in a non-linear manner. Therefore, the response is first-order proportional to the mean velocity at the edge of the boundary layer but is also affected by the changes in the curvature of the velocity profile ([36]). As shown in our previous work, the response of such sensors follows closely that of a 2nd order harmonic oscillator, which is described by a nearly constant gain until 30 percent of the natural frequency f_n . In liquids, the response is typically overdamped, which excludes any ringing ([59]).

The methodology presented herein follows the design of such sensors to be implemented in complex geometries by the technique of planar inlays made of elastomeric sheets. These pillars are easily laser cut from the large elastomeric sheets (sheet thickness 1.5mm) and then are clamped between parts of the model as shown in [59] and [53]. The shape of the elastomeric sheet is based on the wing cross-section and also has protuberances in the form of long slender beams with rectangular cross-sections, which represent the biomimetic sensory hairs. A wing model based on a NACA0012 profile was built which had an integrated 2D array of such sensors on the suction side. Each row of sensing pillars was clamped in between NACA0012 model sections. Each silicone section is a NACA0012 base of chord 20cm, with six evenly spaced pillars, starting at 15% chord. The pillars have a length of 7mm and a rectangular cross-section of 1.5mm by 0.3mm, with the longer side perpendicular to the freestream flow direction, this makes the pillars bend predominantly in the streamwise flow direction and not sensitive to spanwise flow, see figure 19.

The method to calibrate the sensors is described in detail in [53]. The static response is about 1mm tip deflection per velocity increase of 5m/s. The natural frequency of the structures in water is approximately 17 Hz. Note that those values depend on the Young's modulus of the elastomeric material and the clamping conditions, which need careful control during the calibration process and also the measurements. This is because those conditions may vary with time or handling of the wing model.

The above figure 20 shows the pillars under a green LED light, with the pink tips highly visible. The tips of the pillars were carefully marked with fluorescent dye (MMA-RhB- 113 Frak-Paticles, Dantec Dynamics, 584 nm peak emission,

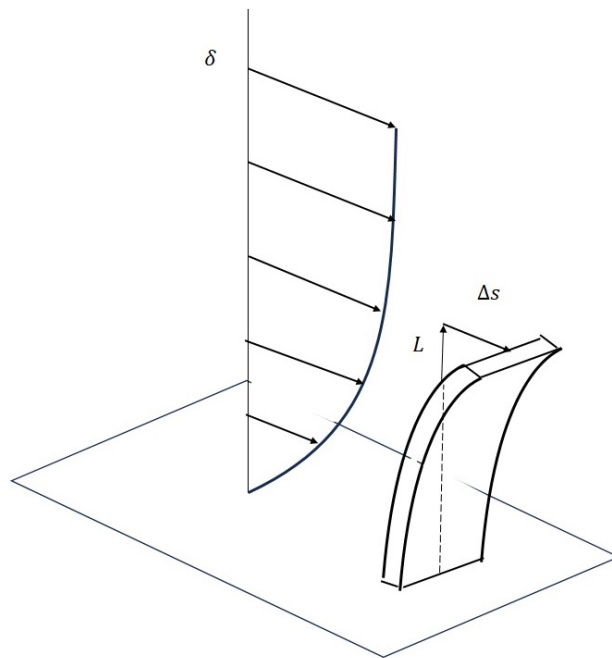


Figure 19: Schematic of the flexible pillar sensor in the boundary layer flow. Note the rectangular cross-section of the structure, which makes the sensor sensitive to only the streamwise flow direction.

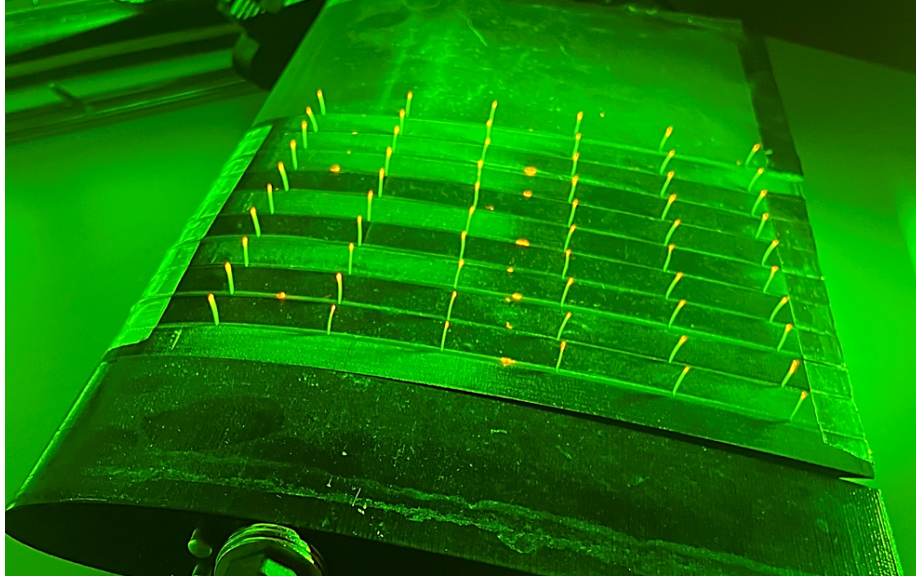


Figure 20: View of the sensing pillars with marked tips, under LED light.

540 nm peak absorption) to enhance the tip movement and aid in tracking them effectively. From the above figure 20, dye spots marked onto the model can also be seen, these were to ensure that the model did not move during the tests and were used as reference spots.

3.3.5 Experimental setup for pillar tracking

The NACA0012 wing equipped with the sensing pillars was placed downstream of the disturbance generator, acting as 'wind hairs' to sense the flow disturbance. Each one of the pillar tips was marked at the tip with a dye that can be seen through a band pass colour filter camera lens for greater contrast. Continuous recordings were taken as the flow disturbance passed the camera viewing window to characterise the flow. The recordings were processed to get the pillar tip deflection along the array. An in-house MATLAB code determined the relative displacement of the marked pillar tip locations between the "wind-off" and "wind-on" situations with an accuracy of 20 microns. This accuracy is achieved by interpolating the Gaussian peak in the underlying cross-correlation procedure, as explained previously.

In the above figure 21, C_1 is the chord length of the gust generator, 30cm and C_2 is the chord length of the sensing wing, 20cm.

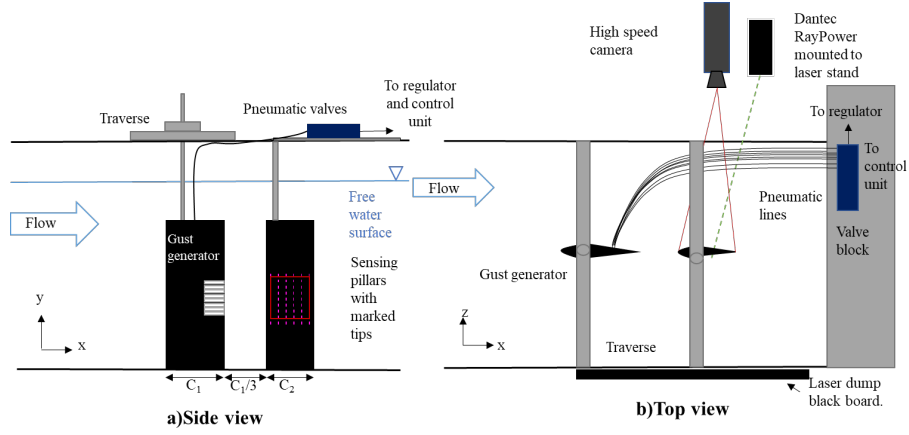


Figure 21: Schematic of the setup for pillar tracking

3.4 Results

3.4.1 PIV Disturbance Characterisation

The disturbance generated with the deployment of the 4 flaps as described in section 2 is characterised by the PIV measurements in the wake in the vertical plane along the chord of the wing (zero AoA) and in the horizontal plane crossing the centre of the deployed flaps. Figure 22 gives an impression of the PIV flow pictures after deployment, shown in the style of multi-exposed images by adding an n number of 10 successive images with an inter-spacing of 2 images. This illustrates the flow as if the picture was made with a pulsed laser light. The top view shows the curvature of the pathlines around the outer edges of the deployed flaps, where flow is diverted to flow around those edges. This flow pattern is nearly mirror-symmetric to the horizontal centerline in the middle of the deployed flaps. In the direct wake of the flaplets, one can see nearly stagnant flow, which then accelerates when moving further downstream. The cross-sectional view indicates the stages during deployment from the reflections of the edge of the flap. During its opening, flow is sucked into the void space and a clockwise rotating vortex is formed underneath the trailing edge of the flap. This starting vortex grows until the flaps are stopped, which is when it is shed into the wake.

The PIV images were taken at snapshots in the flow and shown in non-dimensionalised time as follows:

$$t^* = t \times U_\infty / C \quad (3)$$

Where t is the time in seconds, U_∞ is the freestream velocity (0.35m/s), and C is the chord length of the gust generator (0.30m). We consider $t=0s$, and therefore $t^*=0$, to be at the point at which the flaplets become fully open.

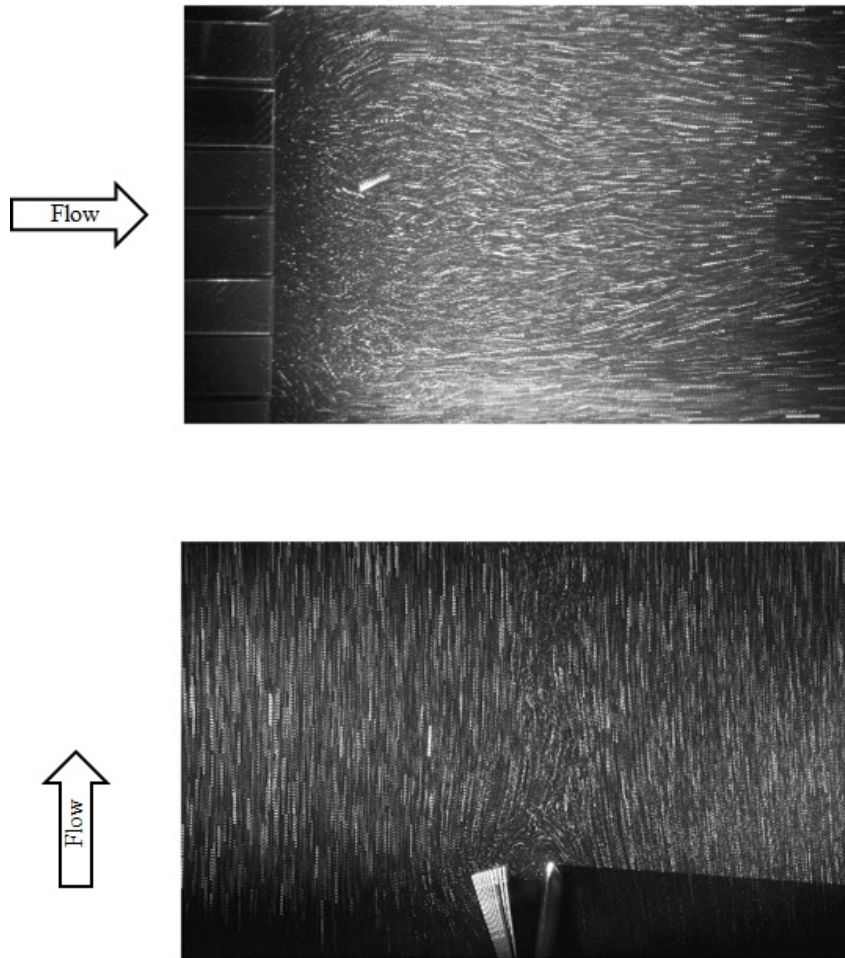


Figure 22: PIV snapshots in multi-exposure mode showing the development of the flow structure from the gust generator, as seen from the camera in the two different planes.

Below, in the figures, the convection of the disturbance structure can be seen, as you move from left to right in the figure. The trailing edge and flaplets were added to aid with layout understanding.

It can be seen from the diverging streamlines near the flaps in figure 23 that there is a flow disturbance at the bottom due to the flaplets fully opening. This agrees with the flow visualisation pattern from the multi-exposed images. The grey-coloured region at a short distance downstream at time $t^*=0.1$ indicates a region of lower streamwise velocity in the wake, which corresponds to the region cut through the centre plane in figure 24, $t^*=0.1$. This is where the streamwise velocity is reduced due to the induction of the head of the starting vortex (indicated by the red arrow in the figure).

The patterns in figure 23 show for all times again a certain degree of symmetry to the centerline, which lets us speculate that the starting vortex is nearly symmetric to the centerline of the flaps. From fundamental vortex theory (vortex lines must close) we conclude that the vortex seen in the cross-sectional view is the head of a vortex loop which has the legs in the form of the tip vortices at the edges of the outer flaps, see below. It must be noted that the field of view must be suitable, such that sufficient vortex lines can be seen, so a conclusion can be drawn as to whether lines are closed or looped.

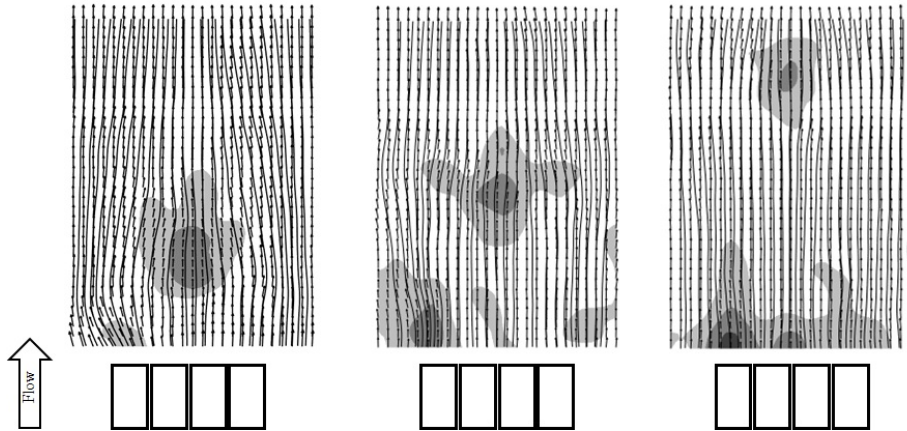


Figure 23: PIV snapshots showing the development of a flow structure from the gust generator, as seen from the camera normal to the wing plane. The vector plot is overlaid with sectional streamlines and the grey areas indicate regions of reduced streamwise velocity magnitude (in steps of 20%). Non-dimensional time is $t^*=0.1$, $t^*=0.27$ and $t^*=0.48$.

In Figure 24, the clockwise rotating red arrow indicates the head of the vortex loop, with a region of high velocity on top and lower velocities underneath, creating a clockwise rolling motion. Note that the vortex is convecting downstream with the mean flow, therefore the streamlines representing the vortex are not closed in circular form but are seen as strong bending curvature (addition

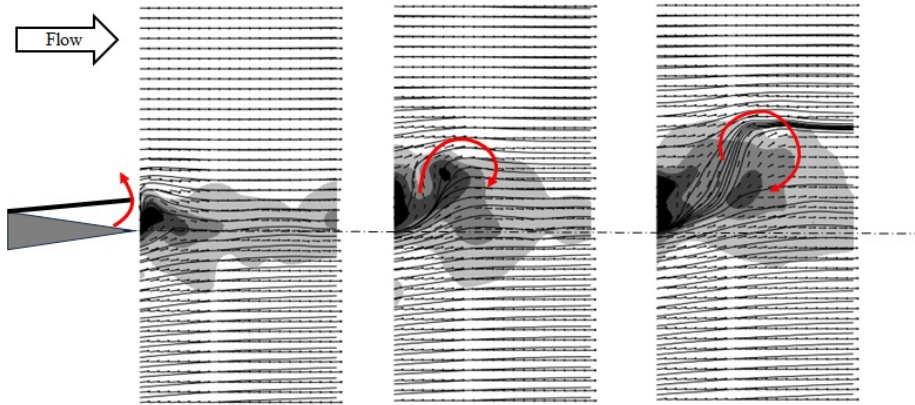


Figure 24: Same as in Fig. 23, however when seen in the cross-section from the camera underneath the tunnel. Non-dimensional time is $t^*=0$, $t^*=0.1$ and $t^*=0.2$.

of mean flow + circulation). This corresponds to the flow region representing the core of the starting vortex.

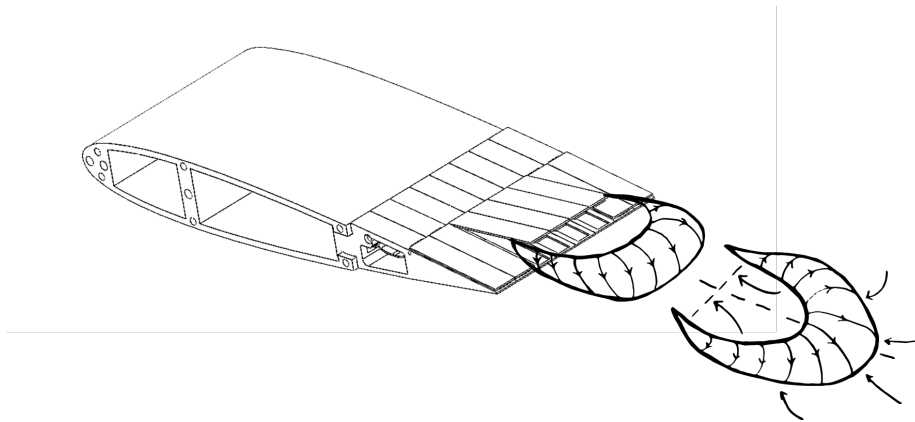


Figure 25: Sketch of the starting vortex after flap deployment, which is shed into the wake, forming a horse-shoe type vortex (derived schematically from the PIV results in the different cross-sections).

Superimposing the snapshots in both the horizontal and vertical planes allows us to draw conclusions on the 3D structure of the starting vortex. A drawing of the underlying structure is sketched in 25, resembling a horseshoe-type shape of the starting vortex when being shed into the wake. The head of the horseshoe is the front of the vortex loop, while the legs are joined on either end to the trailing vortices at the 'wing tips' of each of the outer flaplets. Fig-

ure 25 below illustrates our understanding of the shape of the initial horseshoe vortex forming at the flaplets and then the same vortex as it sheds and travels further downstream.

3.4.2 Disturbance sensing via pillars

The results from the image processing of the sensor images are in form of the pillar tip displacement $\Delta s(x_{i,j}, y_{i,j}, t)$ along the nodes of the array $X_{i,j}, Y_{i,j}$ for several i columns and several j rows. Tip displacement is only measured in the streamwise direction. From 26 it should be noted that the peak tip displacement is 4 pixels, corresponding to 1mm tip deflection. This data was used to plot a quiver plot of the pillar tip deflections at selected times to compare the detected pattern to the induced flow disturbance. It should be noted that the quiver plot given below has the mean flow deflection subtracted to emphasise flow retardation relative to the mean. Therefore positive bending shows accelerated flow while negative bending shows retarded flow.

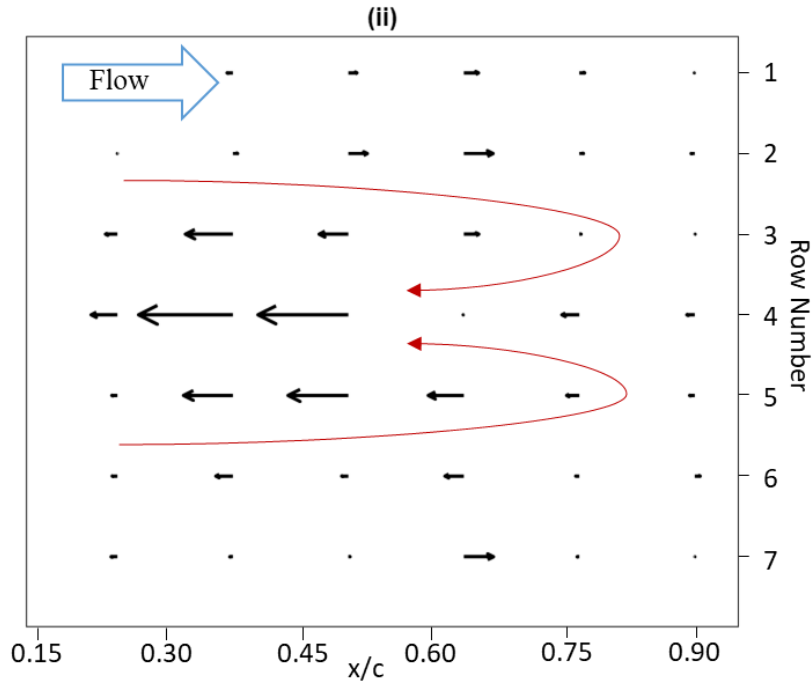


Figure 26: Quiver plot of pillar tip displacement at the instant $t^*=0.7$ when the flow event moves over the pillar array after flap deployment (mean pillar deflection subtracted, maximum quiver length equals a tip displacement of 1mm).

An exemplary result is shown for $t^*=0.7$ in 26, which is when the disturbance is expected to convect to the middle of the sensory array (for the given period

and distance to the gust generator). It can be seen that the disturbance roughly appears over five pillar rows at a time (rows 2-6 as shown), this correlates well to the affected span seen in 23, where the disturbance also acts over the span of the deployed flaps. In addition, the reconstructed pattern shows some degree of symmetry to the centerline, similar to what is observed in the characterisation of the disturbance pattern. There is a maximum local reduction in the deflection of the pillars along the centerline row for columns 2,3 (inline with the centre of the flaps). A weaker reduction is above and below this row which is where the pillar tips are nearer to the outer flaplets. Further away from the centerline is some flow acceleration as seen by the positive bend of the pillars. The red lines overlaid on the quiver plot indicate the suggested alignment of the head of the vortex loop and the resulting induced flow pattern underneath, as expected from the PIV images. Overall, the reconstructed pattern matches with what is expected to be a footprint of the horseshoe vortex on the trailing wing. Note that the strength of the induced vortex dissipates over the travel distance between the gust generator and sensing aerofoil due to viscous diffusion. This is why the PIV measurements for characterisation were done in the same downstream location as where the sensing pillars are placed.

The figure clearly shows that the pillars can detect the event by the time and structure it left as a footprint of such disturbance when travelling over the wing. In combination with event-based cameras or real-time image processing, such events could be recorded online, which is the pathway for feedback flow control. The observed pattern is also typical for stall cells, [60], therefore such measurement could also help to investigate the dynamics of such flow features in research.

3.5 Discussion

Our focus herein is the application of imaging techniques to detect patterns of sensor deflections that deviate from the mean situation when the aerofoil is flying in gusty conditions. The findings and their interpretations are discussed in this section, alongside limitations and future research.

From the results, it can be seen that the pillars are detecting the disturbances created by the gust generator, as both the disturbance and the Quiver plot show 5 rows of pillars being affected. Note again, that the shown quiver plot has plotted the tip deflection relative to the mean. The documented instantaneous pattern is nearly symmetrical to the horizontal centre line, which is the symmetry plane of the horse-shoe type flow structure generated from the gust generator. As mentioned above the starting vortex is generated and shed when the opening has stopped and the structure is then travelling along the suction side of the trailing wing, which is equipped with the sensing pillars. When the starting vortex is moving above the area of the pillars we see flow retardation in the centre and positive flow acceleration along the outside of the structure. This reflects the induced flow field underneath the horseshoe vortex. Therefore the pillars can detect the event by the time and structure it left as a "footprint" of such disturbance when travelling over the wing.

Overall, the results so far represent rather a qualitative picture of the disturbance pattern. In correlating the strength of those patterns, we must assume that the bending magnitude is approximately proportional to the mean velocity in the boundary layer and that the sensor response is fast enough to respond to critical events, which is predefined by the mechanical response of the cantilever-beam type elastic pillar. Beyond that, a further direct quantification of the flow velocities from the tip bending magnitude is not possible with good accuracy. This would require some further knowledge of the shape of the velocity profiles and details of the boundary layer characteristics, in addition to a calibration in respective flows. As such profile details are often not known a priori, the major value under such conditions is to gain the spatiotemporal characteristics of the disturbance pattern, albeit probably not reflecting all details of the disturbance in frequency, scale and strength. Nevertheless, the observed tip deflection pattern correlates in structure, symmetry and magnitude with the induced horseshoe vortex-type disturbance of the flow. Therefore, modern imaging techniques such as online motion capture technologies applied to the tips of the sensors can help to "feel" such disturbances real time during flight.

3.6 Conclusion

The results provided in this paper show the capability of flow-sensing pillars to be used for detecting the spatiotemporal footprints of flow events passing over a wing, tested in a flow channel with a specific gust generator. The observed pattern is also typical for stall cells, [60], therefore such measurement could also help to investigate the dynamics of such flow features in research. In combination with online image motion capture techniques applied to the fluorescent pillar tips, such events could be recorded online, which is the pathway for feedback flow control.

The verification of the capability of the pillars allows future research to be carried out using them. Event-based cameras are being investigated for flow monitoring and their potential is currently being discussed in other image-based velocimetry methods such as PIV [61]. It is hypothesised that event-based imaging of the 2D arrays of our sensor pillars would be an ideal candidate for such technology as the objects of interest (the pillar tips) are arranged in a well-ordered pattern and the deflections are typically in a limited range around the original wind-off situation. Furthermore, there is no need to calibrate for any out-of-plane motion as the geometrical structure of the sensors is predominately designed to be sensitive only to flow in the streamwise direction. In addition, the given number of pillars would provide a defined number of selected markers in the flow to be monitored, which does not change over time. Such type of event-based imaging of the sensors is planned as future work in our lab. Furthermore, machine learning may help to train the system for specific events, which then can be applied to different flow control strategies or for collision avoidance when detecting the wake of other objects.

3.7 Critical Review

3.7.1 Paper Overview

Paper 2, was a comparative study between the known flow patterns caused by an upstream disturbance and the ability the wind hairs had to detect such a disturbance. Experimentally, the model used as the upstream disturbance generator was the model developed and tested in Paper 1, with an improved and more reliable actuation method. The wind hair model is built on work already carried out in our research group, [62], and developed into an array of sensing wind hairs integrated into a NACA 0012 aerofoil, it should be noted that the size and shape of the pillars were not changed from that of past work. This was done such that results could be compared but a full geometrical study would be beneficial (discussed later on). The generated disturbance was observed, via PIV, to be a horseshoe-type vortex that was shed into the wake after the deployment of the flaplets. When the sensing array was put in the same location as the PIV was centred on and under the same conditions, it was found that the hairs could detect the arrival and the base structure of the flow disturbance. Therefore, these hairs have the ability to detect known flow structure footprints.

3.7.2 Supplementary Information

Wind Hair Design and Manufacture

A more detailed view of the makeup of the sensing array is shown below in Figure 27 and the overall sensing model in Figure 28. It can be seen that the silicone sheets (shown in red), of a chord section with the six hairs, are clamped between the 3D-printed aerofoil sections. The 3D sections are 1.6cm in the spanwise direction and have location pins on either side of the connecting rod, to ensure that each silicone section is aligned with the printed section that it sits on. Each section has a hole (as shown by the large black circle), which allows for a threaded bar to be inserted throughout the sandwiched array setup. The bar threads into a bottom piece, which is a large spanwise printed section of around 10cm span. A silicone section, without sensing hairs, was glued onto the bottom of this section to protect the perspex viewing section of the water tunnel. A similar top piece sits on top of the sensing array and is clamped down by a nut at the top of the model. The top and bottom pieces allow the sensing array to sit centrally in the tunnel, away from the wall effects at the bottom and wave effects at the top.

Real world applications

The real world applications of these sensing pillars are likely to be limited to academic research purposes, due to their low technology readiness level. However, they act as a low-intrusiveness flow sensing method when paired with a high-speed camera tracking the tips. They are also very cheap to produce and could be easily varied for specific applications, such as changing shape, length and bending properties for different fluids and flow structures. This being said, if the pillars were integrated into a skin, then the skin could be attached or

stretched over existing parts, thus not requiring a redesign for integration. This could then mean that the pillars could be used easily in other tunnels with other researchers, or even in industry, where easy flow sensing is required. A geometrical study would need to be conducted to allow for appropriate scaling and material selection if the pillars were to be used in different studies.

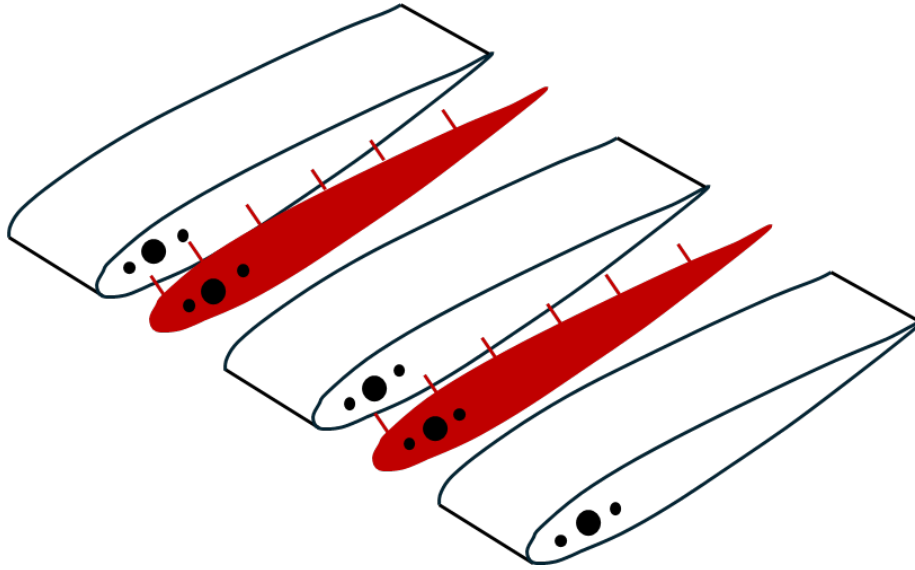


Figure 27: Exploded view sketch of two hair sections sandwiched between 3D printed aerofoil sections. Not to scale.

3.7.3 Problems and Limitations

Wind Hair Accuracy

The correlation the strength of the flow patterns detected by the hairs, was based on the assumption that bending magnitude is proportional to boundary layer mean velocity. It was also assumed that the response of the hairs was adequate to respond to the flow events. Whilst, some calibration testing has been performed on the hairs, see the Calibration Section at the end of this thesis, a more in depth study must be conducted both geometrically on the hairs and the boundary layer profiles. The assumptions must bear true, as the hairs could detect the flow structure and magnitude but perhaps lack accuracy in frequency and strength of the pattern.

Wind Hair Limitations

Due to the nature of the rectangular cross-section of the hairs, they can only bend in the streamwise direction. Whilst this limitation on out-of-plane movement can be beneficial (as discussed in Paper 3), it does mean that the hairs

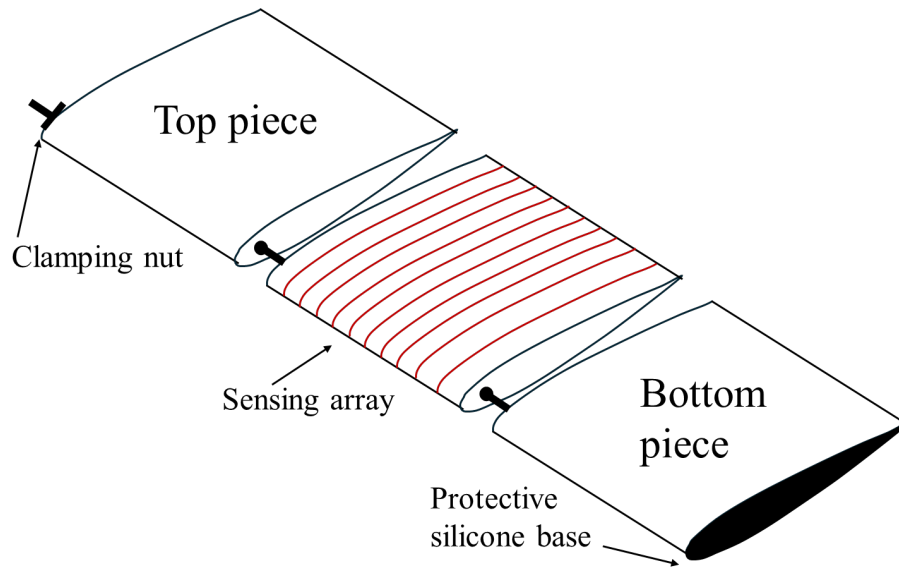


Figure 28: Sketch of the whole sensing model. Not to scale.

are bound to measure one component only. A circular cross-section would allow for another component of motion and so should be considered in the geometrical study. This increase in motion would help to detect better oncoming flow structures that are not perpendicular to the leading edge.

3.7.4 PIV Uncertainties

Detailed below are some sources of uncertainty that arise from PIV.

Stokes Number

Referring to the Equations 1 and 2 as described in the previous Critical Review Section for paper 1 and ρ_p as $1.2g/cm^3$, then $Stk=0.0003$ for these experiments. Thus the accuracy errors are below 1%.

Processing

A multipass algorithm of 48×48 pixels and 32×32 pixels was used for the PIV processing. Using the calibration of 7.7 px/mm this correlates to $6.2\text{mm} \times 6.2\text{mm}$ and $4.2\text{mm} \times 4.2\text{mm}$ respectively. Reducing the window even more, to 16×16 pixels, would improve the averaging of the particle displacement but runs the risk of producing erroneous vectors.

3.7.5 Future Work

Detailed below are some different directions that this work could take for future investigation.

Integration for Smart Skin

The idea of smart skins and integrated sensing, such as [10], is becoming an area of interest. Being able to create materials that have inbuilt sensing abilities to monitor various desired parameters, such as; temperature, velocity, and stress rates will help pave the way to safer, more efficient flight. In the case of the sensing hairs, they could be manufactured into a 'skin' covered in sensing hairs, via injection moulding. This would allow for the new smart skin to be non-invasively used on existing models, by just stretching the skin over the area of interest. Such an application lies mainly in research but could also extend to industry for model testing in areas such as racing car design and optimisation.

Other Sensing Capabilities

As touched upon in the previous paragraph, the development of smart skin, allows for other sensing capabilities. Major advancements in microfabrication technologies and electronics have allowed for the development of skins that sense a variety of parameters, [63] conceptualised a structural health monitoring smart skin sensor, that can identify the growth and propagation of cracks, via radio-frequency. Similar ideas are being developed for use on aircraft, with a short review of recent progress in [64], such structural technology could make the aircraft self-learning and self-repair certain areas. Designing more multifunctional skins, such as [47], could allow for multifunctional flying perception abilities, as well as structural health monitoring. The multiple sensors can detect flow separation, flutter and stall.

Fly-by-Feel via Active Flow Control

Research is currently being conducted into active flow control, using combined jets in [65] and shows potential for decreasing the unsteadiness of the vortex shedding in the wake. Whilst this work would not be using jets, but rather trailing edge flaplets or a morphing trailing edge, it shows the interest in active flow control. Team these ideas with machine learning algorithms, as reviewed in [66], to detect and react to flow structures accordingly and we have effective fly-by-feel solutions.

Event Based Cameras

EBCs are a novel and upcoming area for flow detection. These cameras are based on events, not frames, as per traditional cameras, the benefit being that a reduced data set is outputted, as data is only captured when there is a change detected. Researchers are looking into EBCs to replace traditional PIV setups, [61]. This could prove useful for the sensing hair array, as the motion of the hairs is already limited to a single plane and should have a low event rate.

3.7.6 Measurements for the Future

If this Paper were to be continued, the following points would act as a good basis for project improvements.

Wind Hair Study

The wind hairs should undergo both a geometric and material study to better understand their parameters' effects on their ability to detect certain flow characteristics. For the geometric study, parameters such as length, width and material thickness should be considered. The current configuration of wind hairs is that they are thinner in the chordwise direction than in the spanwise direction, this was a conscious choice to ensure that they would bend only in the chordwise direction and eliminate out-of-plane motion. However, the cross-section shape should be considered if other planes of motion wish to be studied. The length of the hair must be considered along with the thickness of the boundary layer at that chordwise location but also with the desired sensitivity of the hair. Another route of study would be to characterise the effects that the hairs have on one another, to look into the shedding frequency of each hair and how the spacing between them modifies their interaction and ability to detect flow characteristics. Material studies could also be conducted to establish the link between flexural modulus and the sensitivity of the hair to flow events.

Wind Tunnel

The wind hairs could be tested in the wind tunnel, without an upstream gust generator but at high AoAs, to investigate their ability to detect stall cells. Using the sensing hair model, and high-speed PIV, the hair tips could be tracked as they have been, but at higher AoAs, approaching, during and post stall. This work has already been started in our research group, [53], where it was found that the hairs have the ability to detect low-frequency oscillations, which are stall pre-cursors. This work has the potential for further development, with the authors citing material optimisation, hair location and manufacturing issues to be improved upon. Many of the author's improvements have been discussed in the paragraph above and together form the basis of this project continuation.

This page has been left blank to separate chapters

4 Paper 3(Unpublished)-Event Based Cameras: A Comparative Study For Fluid Event Detec- tion

Contents

4.1	Abstract	62
4.2	Introduction	62
4.3	Background	63
4.4	Experimental Setup	64
	4.4.1 Dynamic water test	65
	4.4.2 Static air test	66
4.5	Results	66
	4.5.1 Dynamic water test	66
	4.5.2 Single gust disturbance	70
	4.5.3 Cross flow disturbance	71
4.6	Conclusions	72
4.7	Extension	73
	4.7.1 Further experimental setup	73
	4.7.2 Further results	74
	4.7.3 Further discussion	77
4.8	Critical Review	78
	4.8.1 Paper Overview	78
	4.8.2 Supplementary Information	78
	4.8.3 Problems and Limitations	78
	4.8.4 Future Work	79
	4.8.5 Measurements for the Future	80

4.1 Abstract

A feasibility study using an event-based camera for the detection of plane-wise motion of a 2D array of bio-inspired sensing pillars to detect generated flow events. EBCs show potential for future applications where PIV may have been classically used. They have the benefit of only generating data when an event happens and with comparatively cheaper setups, they hold great potential for flow monitoring. EBCs collect pixel x and y locations, as well as pixel contrast change data at each time there is an event and can be trained on regions of interest. Comparative experiments were carried out in the labs at City, University of London, to investigate the feasibility of using EBCs for the detection of generated large flow structures in both air and water. The disturbances were produced by a gust generator, an upstream cylinder and an air gun for a variety of controlled situations, such as disturbances caused by gusts, crossflows and wake downstream oscillations. Some results were also compared to known PIV results from our lab to see how EBCs can detect a known flow structure over the sensing pillars. The results presented demonstrate the capability of the pillars and EBC to detect large flow structures. These initial results show promise for future applications of flow monitoring, such as real-time flow monitoring via a machine learning algorithm that is trained to detect certain flow patterns over the sensing pillars. This would be an intermediate step into a fully automated flow control loop.

4.2 Introduction

Classical frame-based cameras produce set-size images at set time intervals, providing large amounts of data regardless of whether something has changed in the field of view from the last time stamp. Event-based cameras, EBCs, capture data asynchronously in the form of a timestamp, pixel x and y locations and pixel contrast changes. This results in areas of view with no data, meaning that no pixel change has occurred and areas where change has occurred, either positive (bright) or negative (darker).

EBCs are not new technology, with the fundamental concepts having been discussed since the 90's in [67] and [68]. More recently, there has been work published on computer vision by [69] and [70]. The interest in these cameras has grown in recent years due to their relatively low cost compared to other high-speed setups [71]. However, the output of these cameras are very different to standard frame-based cameras, thus requiring novel processing techniques, as discussed in [72].

Researchers are now looking at applying EBCs to areas such as fluid dynamics for the application of particle image velocimetry, PIV. [73] discusses the uses of EVBs for PIV and the shortcomings that they have, it is found that an EVB and a low-cost pulsed laser provide a cost-effective alternate method of PIV measurement. From the same lab, [74], time-resolved PIV was successfully carried out with an EVB as opposed to a high-speed camera. The found result was that the described system was able to produce high-quality data, equivalent

to expensive high-speed camera setups at 10kHz.

In our lab, at City, University of London, work has already been carried out on the development and testing of a pneumatic gust generator, [58] as well as bio-inspired silicone sensing hairs [75]. The silicone sensing pillars are an ideal candidate for EBCs, as they are set event areas with only single plane movement, reducing the post-processing filtering requirement.

The layout of the paper is such that; experimental methods are detailed after the introductory chapter, followed by the experimental setup. After this, the results of the initial experiments are presented in the form of snapshot images and overlays. Lastly, discussions and concluding remarks are drawn.

4.3 Background

The experiments utilised two models, a gust generator used to generate up-stream disturbances and a sensing model used to detect flow structures. The two models have already been designed and tested in our lab, they are described in detail in [58]. The below figure 29, shows the array of flexible sensing pillars integrated into an aerofoil, the tips of the pillars are marked with a fluorescent dye (MMA-RhB-Frak-Particles, Dantec Dynamics) and viewed via a colour filter lens to ensure the tips are easily identifiable by the camera. The sensors are silicone and have a rectangular cross-section allowing for movement in the streamwise plane. The pneumatically actuated flaplet model will be referred to as the gust model and the bio-inspired flexible pillar model, the sensing model.

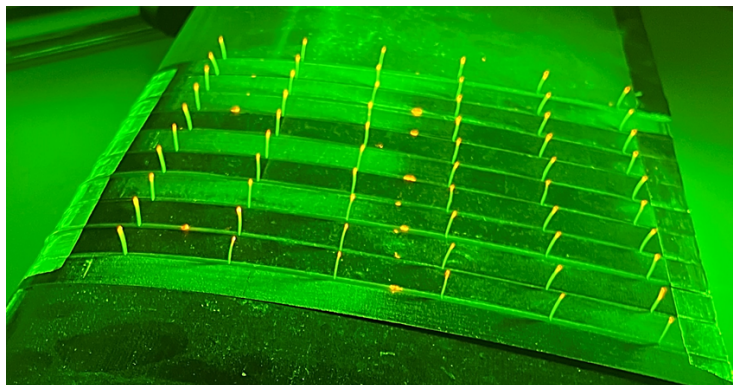


Figure 29: Photo of the sensing pillar array, with marked tips shown under green LED, taken from [58].

The EBC used in this paper was the EVK4 HD by PROPHESEE. Their camera was inspired by the functions of the human eye, where photoreceptors in the back of the eye turn the incoming light into signals, these signals are then processed in the brain via the optic nerve. Much like the photoreceptors, the pixels react independently and asynchronously to scene light changes. The result is sparse event data, driven only by changes in the scene.

Events generated by the event sensor are represented by two colours, which are the default camera settings; white to show increased light intensity (positive contrast change, polarity=1, "ON") and dark blue to show decreased light intensity (negative contrast change, polarity=0, "OFF"), where there are no events the colour will be black or white depending on the chosen colour schemes. When a pixel detects an event, it is transmitted to the on-demand readout, along with the timestamp, x and y positions and polarity of the contrast change.

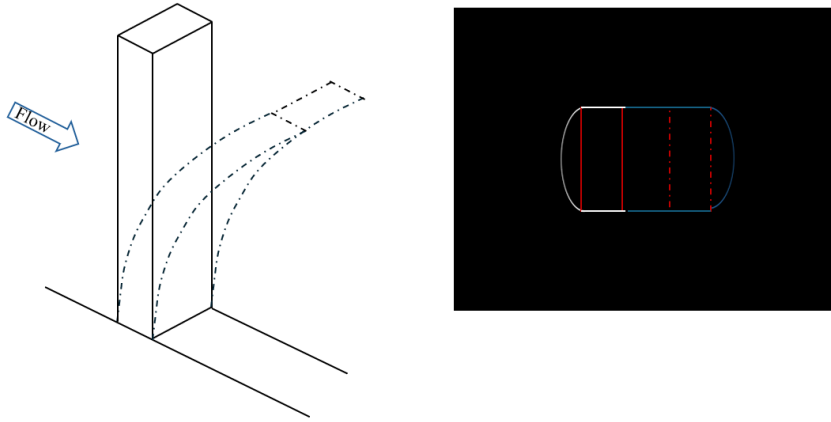


Figure 30: Schematic of the movement of the pillars as outputted by the camera.

The above figure, 30, shows the streamwise bending of the pillars due to oncoming flow on the left and the top-down view of the movement of the bending pillar on the right. The right-hand view is shown as how the camera shows the data, with the red boxes to show pillar movement overlaid. The white and blue lines represent a very simplified image that would be outputted, they represent the shape of the pixel spread detecting a change event.

4.4 Experimental Setup

Two measurement setups were used, a dynamic water test and a static air test to obtain a wider variety of results. The tunnel used was the water tunnel at City, University of London. The water setup for this paper follows largely the same structure as the setups described in [75], for ease of comparison. The camera used for the measurements was an event-based camera (Prophesee EVK4 HD), 1280 x 720 with a colour filter fitted. The filter was to aid in the visibility of the pillar tips, (marked with fluorescent dye), it was a green light filter (long-pass optical filter, cut-off wavelength of 550 nm, Edmund Optics). The cross-section of interest was illuminated by Dantec raypower 5000 5W continuous wave Argon-Ion laser ($\lambda=532\text{nm}$) with sheet thickness 1mm. The laser was

mounted outside the tunnel and the beam reflected such that it illuminated the region of interest vertically from below.

4.4.1 Dynamic water test

With Gust Generator

Here, the gust generator model was set upstream of the sensing model by a third of a chord length and mounted vertically in the tunnel. The free ends of the models were against the lower viewing window and above the free surface, as to avoid wave formation. The models were placed offset of the centre of the tunnel so that the trailing edge of the gust model aligned in the same place as the sensing model's leading edge. The tunnel velocity used was 35cm/s.

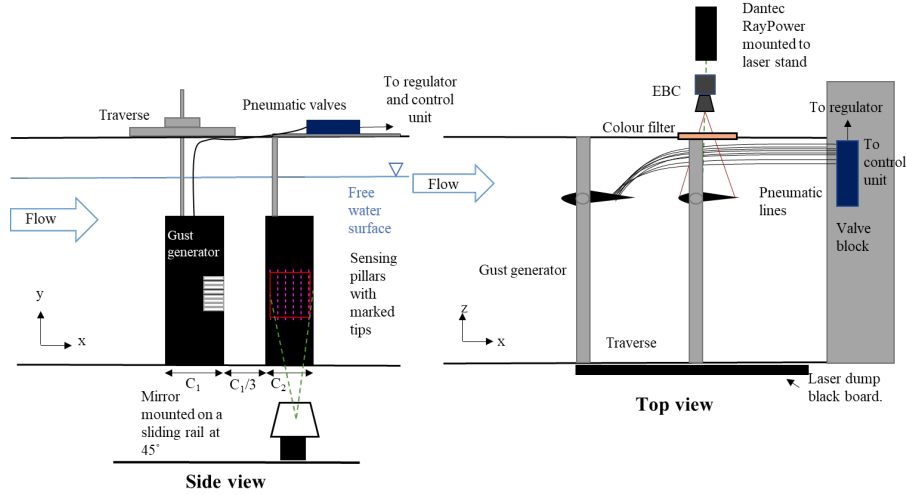


Figure 31: Schematic of the dynamic experimental setup in water with the gust generator.

The above figure, 31, shows the setup for the first of the dynamic water setups. C_1 corresponds to the chord length of the gust generate model, 30cm and C_2 the sensing model of 20cm.

The tunnel was run and allowed to settle to the chosen velocity, after which the gusts were generated via the opening and closing of the flaplets on the gust mode. This disturbance was recorded over the sensing pillars via the EBC.

With Upstream Cylinder

The next set of dynamic water tests were done without the upstream gust model and instead had a cylinder mounted upstream, as the shedding vortices produce constant shedding frequencies. The velocity of the tunnel was again, 35cm/s and the diameter of the cylinder was 2.7cm. The below figure, 32, shows

the setup. the cylinder was mounted perpendicular to the leading edge of the sensing model, centred on the middle row of sensing pillars.

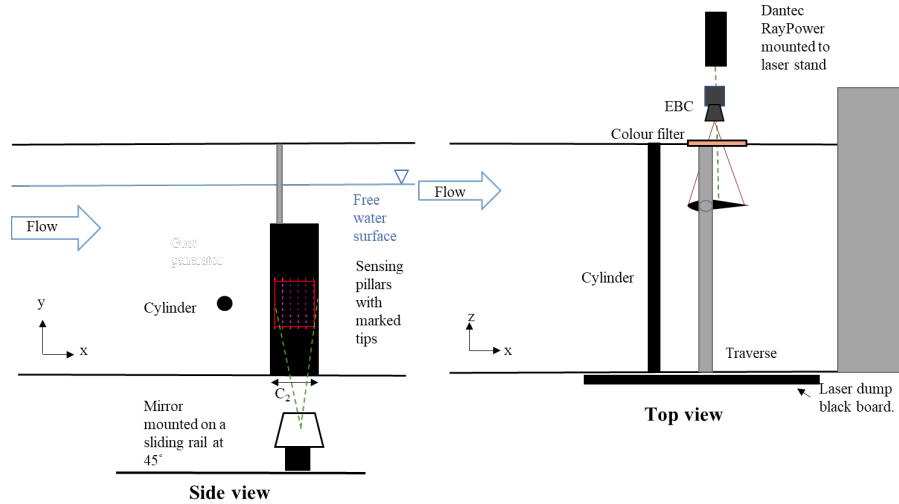


Figure 32: Schematic of the dynamic experimental setup in water with the upstream cylinder.

Like the gust recordings, the tunnel was set to the chosen velocity and allowed to settle. Recordings were then taken of the sensing pillars, as they were constantly disturbed by the upstream cylinder.

4.4.2 Static air test

The secondary set of measurements were taken statically in air, with the disturbance generated by a pneumatic air gun. The mounting of the sensing model, laser and camera was the same as described above, however, this test was done with a dry tunnel. The below figure, 33 shows the secondary setup.

The air gun provided constant disturbance (held on), gusts (pulsed on and off in quick succession) and cross winds (the angle of the air gun changed relative to the central line of pillars). Recordings were taken of all situations.

4.5 Results

4.5.1 Dynamic water test

The dynamic water test experiments gave rise to an opportunity to look at both the disturbance from the generator and the inherent disturbance that arises from the wake of the upstream cylinder over the pillars.

With Gust Generator Upstream

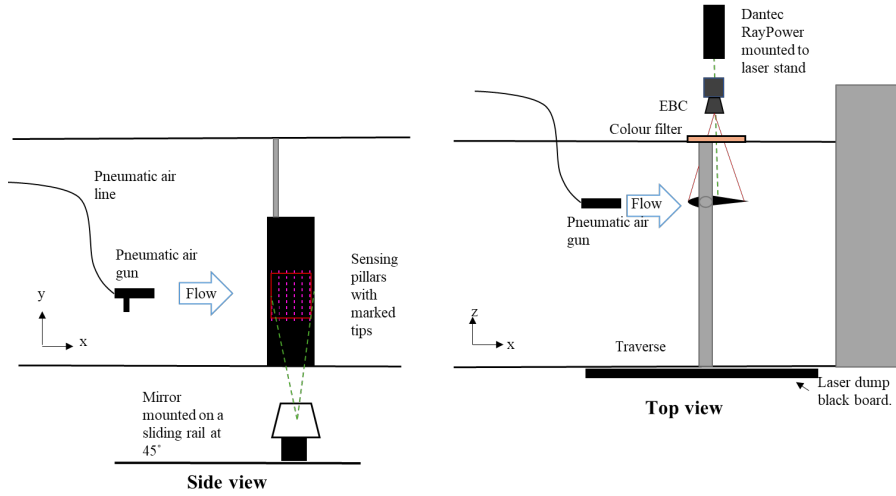


Figure 33: Schematic of the static experimental setup in air.

Twenty stills from the EBC, corresponding to roughly 0.6s, in which the generated disturbance passed over the sensing pillars, were layered together to create the left-hand side of figure 34. The right-hand side of 34, is a quiver plot of the same flow structure of the pillars taken from [75]. It can be seen that the EBC can detect the same flow structure, we can see that the central row of pillars are blue, indicating that the pillars are bending opposite to the freestream direction, which is seen on the quiver plot too. This region of flow retardation is bound by areas of flow acceleration, indicated by the white dots, showing the pillars bending in the same direction as the freestream velocity, this is also shown on the quiver plot.

With Cylinder Upstream

The below figure, 35, is the probability density mapping of one pillar in the wake of the cylinder at 35cm/s freestream velocity. The figure shows a clear pattern of two bright areas, in which the pillar is at maximum velocity coming to inflection in forward and backwards directions, relative to the mean. The two clear bright spots shows that the pillars spend the majority of their time at either extremes, with negligible time spent moving between them. The figure was made by adding one pixel position over time, with a +1 in grey level each time an event happened at this position. Resulting in a grey level map from 0 to the total number of events. The maximum grey level is 225.

The Reynold's number using the tunnel freestream velocity (35cm/s) and the diameter of the upstream cylinder (2.7cm) is $Re_{Cylinder} = 10^4$, using this and the below figure, 36, it can be seen that the expected Strouhal number, St , for the cylinder is around 0.2, assuming smooth surface.

Where St is defined below in 4, where f is the shedding frequency, D is the

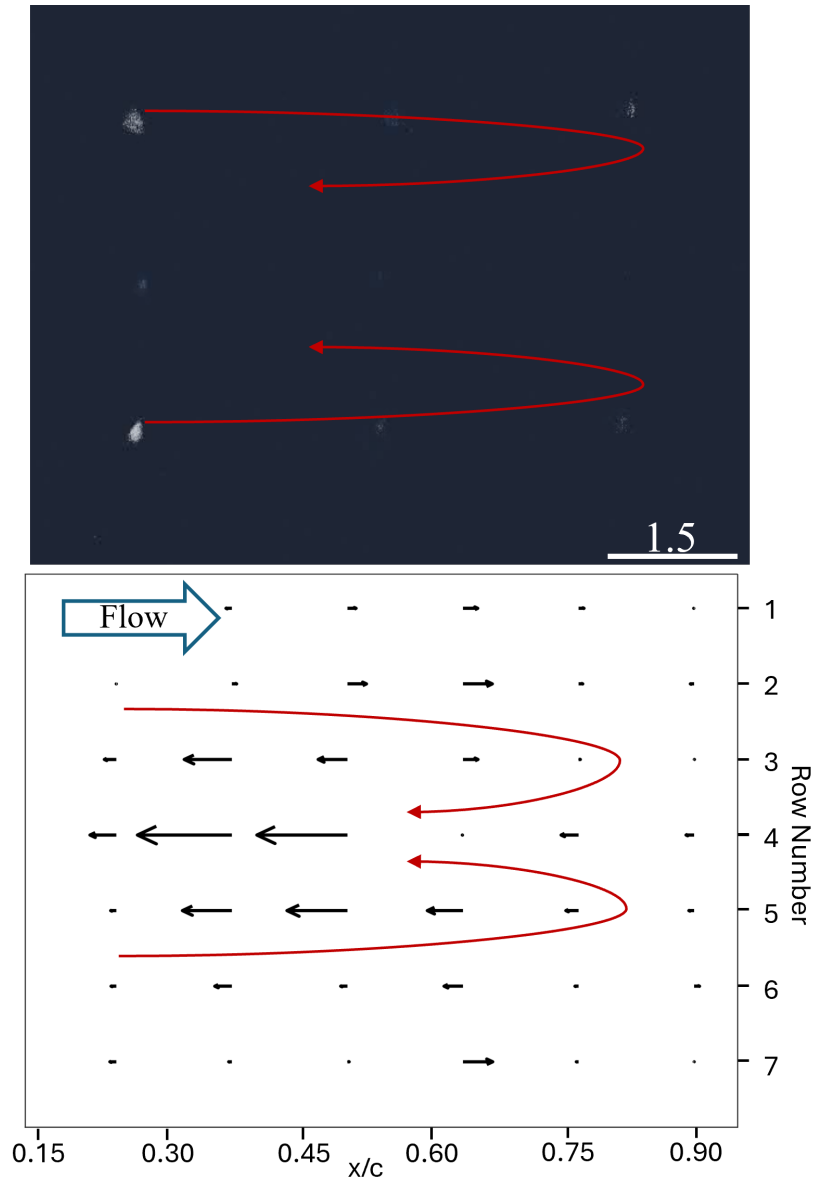


Figure 34: Comparison of layered EBC view and quiver plot from [58]

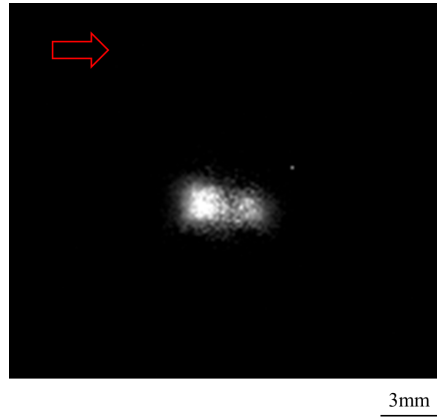


Figure 35: Enlarged view of one pillar probability density location, with red arrow to indicate flow direction.

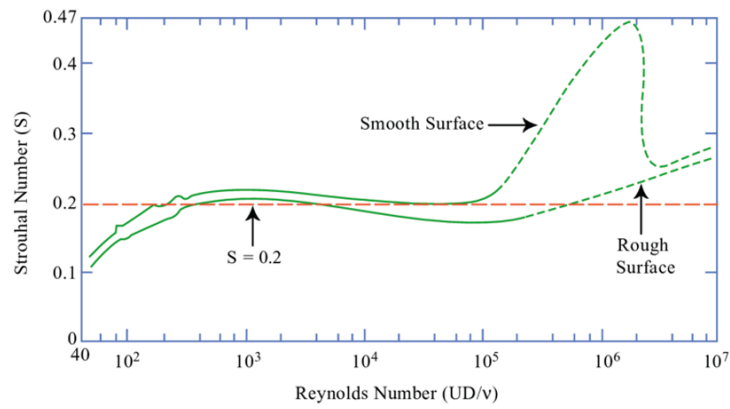


Figure 36: Graph showing the variation of Strouhal with Reynolds for a cylinder, as taken from [76]

diameter of the obstructing cylinder and U is the freestream velocity.

$$St = fD/U \quad (4)$$

Using the recordings taken from the cylinder tests, it can be seen by eye that the pillars oscillate at a frequency of around 3 Hz. Two colour changes, ie white to blue, then blue to white were deemed one full oscillation of a pillar, corresponding to fully back, then fully forward. Substituting an f value of three into the above equation, 4, gives a St number of 0.23, showing that the pillars and EBC can pick up the oscillations from the upstream cylinders vortex trail.

4.5.2 Single gust disturbance

The disturbances generated by the pneumatic air gun as described in the experimental setup were categorised by snapshots of the outputted recordings. The below figure, 37, is two snapshots taken 0.2s apart during the gust testing phase. This was where the air gun was pulsed on and off in quick succession to generate gusts. This is a top-down view of the pillars in the vertical plane, as seen by the EBC.

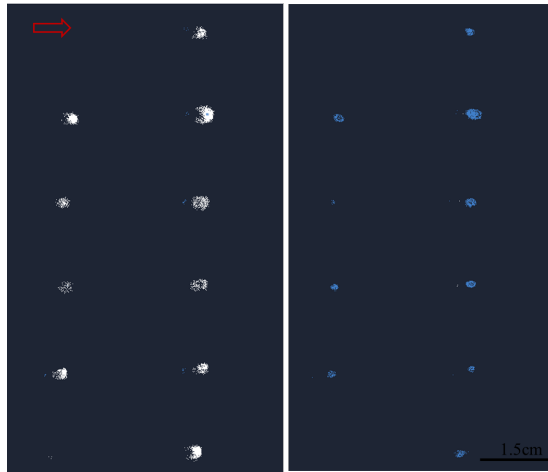


Figure 37: Two raw images of data as shown from the camera in Metavision, taken 0.2s apart, showing flow retardation.

The above figure, 37, shows that the EBC can successfully show changes in the flow velocity of the pillars. All the pillars moving forward during increased flow velocity leave a white-marked positive event at the edge (left-hand image of figure 37). In comparison, when the pillars relax back to their equilibrium position after the air gust they leave a blue region of negative intensity change in the EBC image (right-hand side of 37). A complete colour change of the array indicates a shift in velocity. Here, in this figure, all the pillars changing from

white to blue indicates that the flow over them is decelerating and the pillars are relaxing back to their equilibrium position, the opposite would be true for flow acceleration.

4.5.3 Cross flow disturbance

The results of the test in which the angle of the air gun relative to the centre row of pillars changed are as shown below in 38. This test mimics a change in freestream angle or crosswinds over the sensing wing. It can be seen that there is a rather constant phase difference of π rad in the motion between the rows of pillars (top and bottom rows nearly anti-phase).

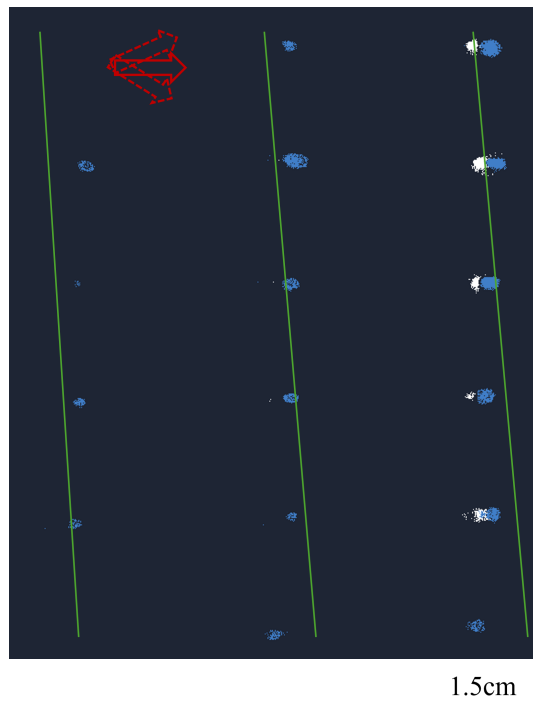


Figure 38: Raw image of data as shown from the camera in Metavision, with pillar phase difference in columns highlighted with green lines. The red arrows indicate oscillating flow direction in a singular plane.

4.6 Conclusions

The results above demonstrate the feasibility of EBCs to be used to detect flow characteristics impacting a wing equipped with bio-inspired wind-hairs, over specific regions of interest, during specific gust conditions in both water and air. The results show potential for future fly-by-feel strategies where the EBCs can be used to monitor the flow patterns passing over the array of sensory hairs. Machine learning will help to train the system for specific events and to use the resulting workflow for monitoring or flow control.

The specific regions of interest are localised and centred around the pillar tips, which allows for sophisticated data collection and processing. Comparing EBCs to PIV, there is a lower event rate, below 1MEv/s, allowing for less data to be collected and easier, quicker processing. In addition, spatiotemporal information of the events along the pillar array makes it easier to distinguish coherent events from background noise, as we can expect a certain degree of consistency in the event patterns over the array. The results show that using the pillars with the EBC successfully distinguishes flow structures of the scale of the array.

The study has shown promise for future applications but is still in its infancy. The EBC requires a high-quality, powerful light source, which reduces the number of real-world applications. It is suggested that for future testing with the pillar and EBC setup, the tip marking of the pillars needs to improve to detect edge events better. A single reflective sphere attached to the pillar tips may help to give an improved localised pattern. Furthermore, one may use wave-guiding features of transparent silicone hairs or optical fibres as the sensing hairs, which could disregard the need for external illumination and provide a better quality of the tip spots.

The future applications for this study could include online flow monitoring via a machine learning algorithm that can detect the pattern of known flow structures over the pillars. This could allow for the implementation of flow control loops, which are designed to react to specific flow patterns.

4.7 Extension

The following section acts as an extension of the work from Paper 3 above. It was decided to test both the high-speed and event-based cameras in identical setups in the wind tunnel. For the disturbance, a set upstream cylinder would provide constant vortex shedding. The setup and arrangement also loosely follows [77] from our research group, for later comparison.

4.7.1 Further experimental setup

The following experiments were carried out in the T2 mid-velocity wind tunnel at City, University of London. Both the high-speed and the event-based camera used were the same camera(s) as described in previous tests. The sensing hairs were also the same as mentioned previously, with the same tip marking.

Figure 39 below shows the schematic of the setup used, where the red box indicates the area of interest for the camera. An existing model with one row of sensing hairs of chord $C_3=20\text{cm}$ was placed 20cm downstream of a cylinder of diameter 5cm. The cylinder spanned the whole of the working section in the y-direction and was mounted centrally to the leading edge of the model in the z-direction. The sensing hair model was mounted onto the above force balance and was touching the bottom wall of the test section.

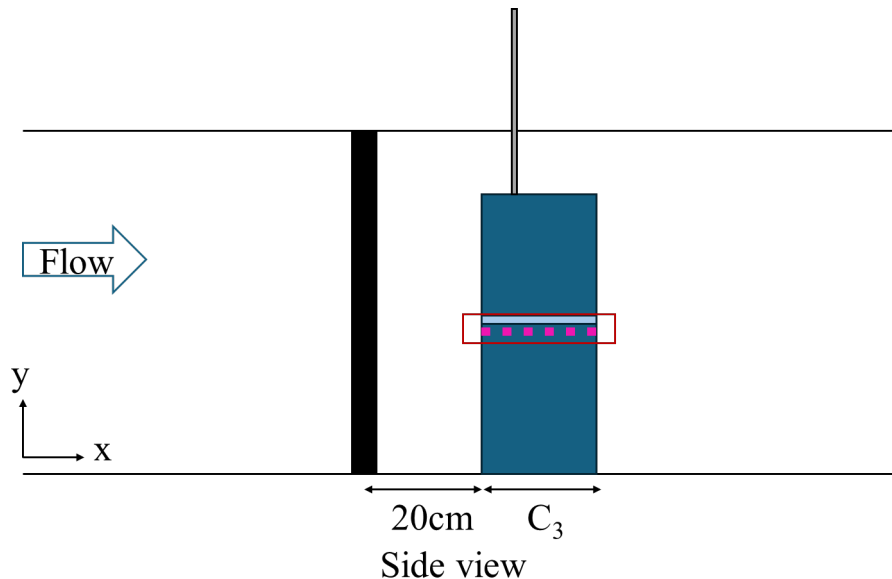


Figure 39: Schematic of the side view of the wind tunnel setup.

Both the camera(s) and the laser were set outside the tunnel, looking in via the optical access section, Figure 40 depicts this setup. It should be noted that the laser had to be lowered and angled upwards onto the sensing hairs,

whilst the camera(s) were perpendicular to the hair tips. Mounting the laser as described allowed for reduced reflections to be picked up. This was due to the sensing model having a chordwise strip of perspex (roughly 2cm) above the sensing hairs.

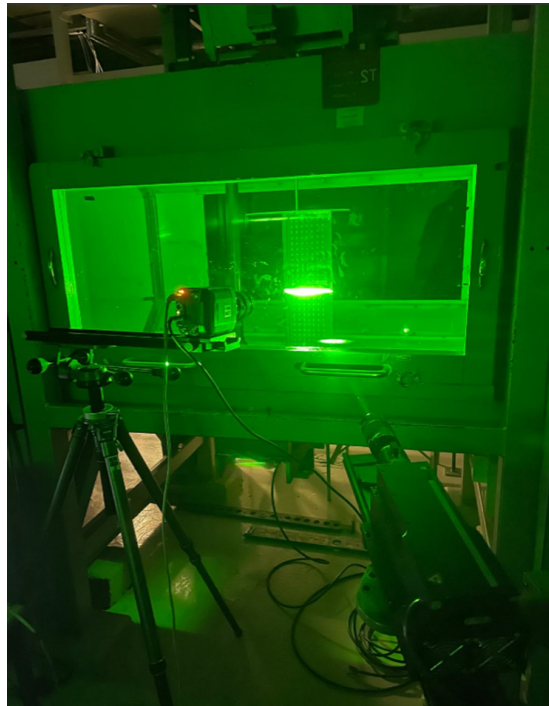


Figure 40: Setup image with both laser and camera visible of the wind tunnel.

The wind tunnel freestream velocity was set to roughly 15m/s, this correlates to Reynold's number of $Re_{cylinder}=50k$ and $Re_{model}=200k$. Using the graph as shown in Figure 36 and the corresponding Reynold's values, it can be found that the $St_{cylinder}=0.22$, similarly $St_{model}=0.2$.

4.7.2 Further results

Event based camera

A sample Python code was used to analyse the frequency of the hair tips with the .RAW file that the EBC produced. The code sample used is an open-access processing algorithm, called Vibration Estimation, supplied by Prophesee (Prophesee, Metavison for Machines, Paris), see Appendix 7.1. This algorithm outputs a frequency map of the recording, as shown below in Figure 41.

The colour bar runs between 10Hz and 150Hz, with the average frequency of the wind hairs at fluctuating between 65Hz and 70Hz. It can be seen from Figure 41, that the algorithm could not properly process hairs 1, 5 or 6 and the

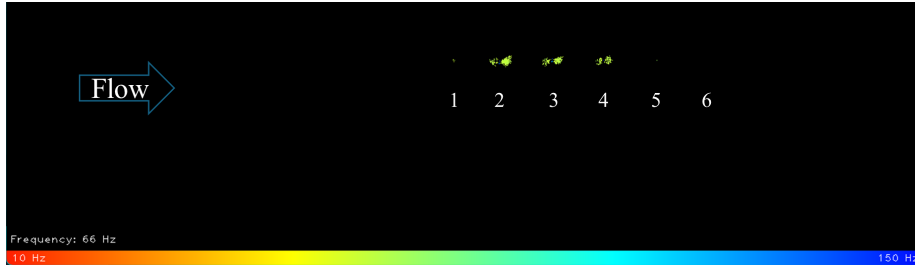


Figure 41: Frequency map of wind hairs in the wind tunnel, with a colour bar below.

resulting image only shows hairs 2,3 and 4 clearly, however it is clear that the average frequency for the remaining hairs is the same.

With the knowledge of $St_{cylinder}$, freestream velocity and the characteristic length of the upstream cylinder, equation 4 can be rearranged to find the shedding frequency of the upstream cylinder, $f_{cylinder}=66\text{Hz}$. This compares well to the frequencies found by the vibration algorithm of between 65Hz and 70Hz. This frequency value was also matched via MATLAB, in which a time series of the hair tip location was created from the x-y coordinates of the EBC and then an FFT was performed to obtain peak frequency. The MATLAB frequency was around 60-70Hz depending on where the area of interest was set.

High speed camera

The high-speed camera was used to track the tips of the hairs, as done previously in papers 1 and 2. In this instance, the results of the high-speed camera are used in comparison to the EBC. Below, in Figure 42, the position time series of the first hair is plotted. The frequency is taken of this hair, as it is the one that is not affected by the others and is in the least developed boundary layer. The frequency was calculated via the inflection points of the data over 0.5s, this is such that the peaks and troughs are counted but the frequency value remains correct as the sample is only 0.5s. The calculated frequency of 71Hz is displayed on the Figure, While this value is higher than that of the EBC, it is still in a 10% range. The higher frequency value here is thought to originate from the 'false' peaks that occur but the inflection point is still counted.

The convection rate of the passing structure can be found from the shift in deflection of consecutive hairs. In Figure 43, the time series of the first three hairs are plotted over a short time period. Each hair follows the same displacement pattern but time shifted back the further away from the leading edge the hairs are. From here, the time between the peaks can be found and, alongside the known distance of hair separation, the convection velocities between hairs can be found. It should also be noted that the deflections of hair 2 are larger due to the increased velocity over the aerofoil at that point.

The below Figure, 44, plots the normalised convection velocity between the

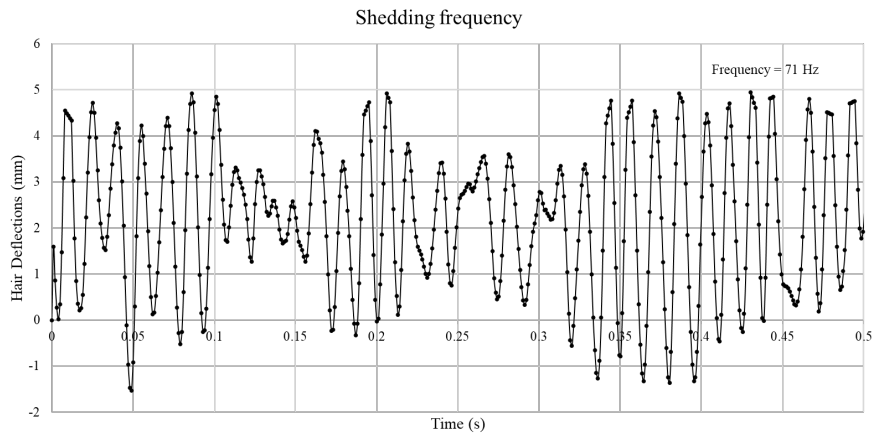


Figure 42: Time series plot of the first hair, with calculated frequency shown.

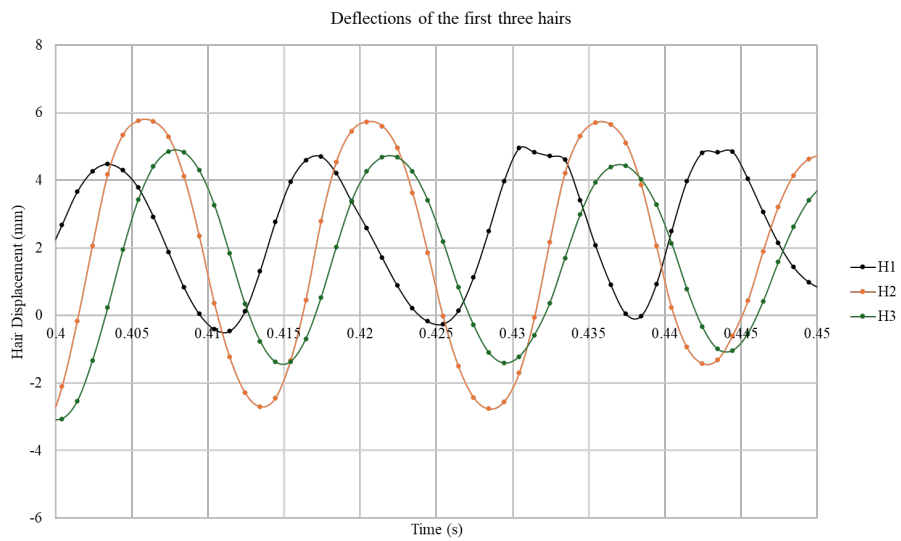


Figure 43: Shortened time series plot of the first three hairs.

hairs. The figure has a graphic of the pillars overlaid to show the approximate location of the calculated convection velocities, and quite nicely shows the expected acceleration over the aerofoil. The red lines indicate predictive data, if more pillars were used, then velocities further forward and aft could have been calculated.

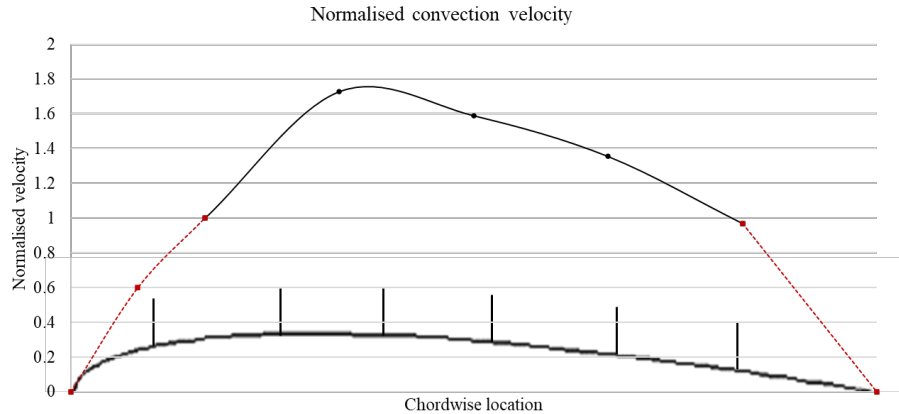


Figure 44: Normalised velocity convection between hairs, with sensing aerofoil overlaid. Not to scale.

4.7.3 Further discussion

The extra results show the ability of the EBC and sensing hairs in airflow conditions with constant disturbances, it is shown that they are able to accurately sense frequencies and oncoming structures. The use of the frequency program with the EBC also shows promise for real-time fly-by-feel flow monitoring in air. Machine learning could be used to train the system to look for certain flow events and then a suitable response could be put in place. The hairs are specific and localised, allowing for a low event rate and data collection rate, however, the layout of the hairs could benefit from a space and layout optimisation study, to ensure that the flow features can be sensed in the most effective way. The ability to detect the upstream shedding frequencies could allow for known frequencies to be detected and filtered out of the seen data, allowing for an even lower data collection rate.

4.8 Critical Review

4.8.1 Paper Overview

This final paper uses the sensing model from Paper 2, with one of the future works ideas. It is an initial feasibility study looking into using an EBC to detect the motion of the sensing array under generated flow disturbances. EBCs are a novel and upcoming field, showing great cost saving potential for classical PIV setups. Results were compared to PIV results from the same setup and under the same tunnel conditions in both air and water. It was found that the EBC and the sensing wind hairs can detect large flow structures and show a lot of promise for the future of real-time flow monitoring.

4.8.2 Supplementary Information

EBC Focus

Focusing an EBC differs from a frame-based camera, due to the fact that a still object will not be detected with the EBC. The EBC is usually focused by placing a rotating black and white disc in your region of interest, however, this was not possible to do in the water tunnel. Instead, the laser was pulsed at a low frequency, this allowed for the camera focus to be modified until the edges of the tips were as sharp as possible. The light intensity change allows for the camera to detect the tips, even without movement.

4.8.3 Problems and Limitations

Detailed below are some issues faced during Paper 3.

Tip Marking

As already briefly mentioned in the conclusions of Paper 3, it is thought that the tip marking of the wind hairs introduced some problems. The tip marking used was the same as described in Paper 2, in which the fluorescent dye was added to glue and carefully painted onto the rectangular cross-sectional tip. When the tips were illuminated and viewed via a colour filter lens, they could be viewed as clear bright spots through the camera. This was a great setup for the high-speed camera but it was not so effective with the EBC. The EBC works best detecting the movement change of something that is very reflective, it is also beneficial to have something with very defined edges of bright and dark. This would give a clear pattern of movement, as opposed to the current cluster. Using white paint as a high contrast tip marker, as opposed to a silver ball, may be a cheaper alternative. The ball may also reflect too much light in an array of directions that aren't useful, whereas the paint would just offer high contrast.

Light Source

Following on from the marking issue, the tips required full laser power to be clearly visible to the EBC. This is likely to be due to either the tip marking not providing enough contrast or reflection, or the colour filter lens that was

added could have absorbed too much useful light. It could also be due to the water tunnel, and that light was absorbed while travelling through the water and reflected in other directions. The EBC should not usually require the intensity of the light source that was used in Paper 3 (a 5W laser, operated at 3W), in fact, Prophesee demonstrated their camera under usual daylight conditions. Having to use a high-powered laser with this setup reduces the real-world uses, due to safety implications, however, if the tip marking was improved, it is thought a lower intensity light source could be used, such as a standard LED.

Data Processing

The data from the EBC is outputted into a .RAW file and can be changed into a . DAT file via a command prompt from Prophesee. The data file contains the x and y locations and the change intensity value at each given time stamp that an event is detected. Whilst the raw file is very small, the data file is in the order of a few GBs for less than 5s at a low event rate ($<1\text{ME/s}$). This file then becomes difficult to process via MATLAB, as it is so large, meaning the data file had to be split into 1-2 second intervals to be processed. As the EBC for particle tracking is so new, there are few resources to learn from in regards to processing the output files. Prophesee offers sample processing algorithms in Python, one of which was used in the extension of Paper 3.

4.8.4 Future Work

Detailed below are some bigger-picture ideas of how the work documented in Paper 3 could be applied.

Real Time Processing

The ability to process and see results in real-time from the wind hairs could be a future area of interest, especially for tunnel testing of models. This would drastically reduce setup times and could also prove useful for initial flight tests, to gather real-world data. real-time monitoring wing systems have been developed, such as [78], in which a binocular non-contact method of morphing winglet monitoring was developed. The sensing hairs are cheap, lightweight and non-invasive, meaning that they can be retrofitted to specific regions of interest on models and then tested with real-time processing to see the flow events.

Machine Learning

Combining machine learning with the morphing wing concepts, already discussed previously in the critical review of Paper 1 and active wing control from the critical review section of Paper 2 could lead to active wing control for a variety of parameters. Researchers have developed active flutter suppression via machine learning in [79] that can automatically tune the flutter control parameters via reinforcement learning. This is applied to a flexible flying wing aircraft and has led to more efficient controller performance. Also, air data parameters can be estimated using embedded wing sensors, which can then be

put into a machine learning algorithm to estimate AoA and airspeed [80]. This shows the potential that the location of the hair tips could be used alongside a machine-learning algorithm to determine known flow patterns.

Real world applications

The addition of the EBC alongside the sensing array makes this setup more appealing to real-world applications. If the future work suggested was integrated, then the real-time intelligent sensing system would have many applications. Being able to see in real time the flow structures would have beneficial applications for industry, initial wind tunnel models could be improved upon quickly, without having to process masses of PIV data. It may also prove useful for sensing on a wing, where spoilers, flap settings and pitch/yaw are being investigated and seeing the dynamic effects would be beneficial.

4.8.5 Measurements for the Future

To continue on with this work, it is suggested that the following measurements and setups are considered first.

Improved Marking

Investigation into improved tip marking needs to be carried out to determine the best material and marking technique to ensure clear visibility with the EBC. It is theorised that a thin coating of silver would provide adequate reflection but may be difficult to bond to the wind hair tips. Instead, a small silver ball could be glued to the tips of the hairs, however, care must be taken to ensure that the weight of the tip marking does not affect the bending of the hairs.

Gust Detection

The EBC setup should be further tested with a clear upstream gust, as opposed to constant shedding frequencies produced by the cylinder. The constant shedding frequencies produced mean that the tips are in constant motion and therefore the EBC produces a lot of data when there is little of interest happening. Perhaps known frequencies could be filtered out during the processing stage, but this has not yet been investigated here. It is believed that the EBC would be better suited to detect gusts or large flow structures, as they are well defined movement patterns.

This page has been left blank to separate chapters

5 Conclusions

Contents

5.1	Concluding Remarks	83
5.2	Purpose and Novelty	83
5.3	Future Work	84
5.4	Emerging Topics	84

5.1 Concluding Remarks

The research defined by the three papers has shown positive results for both the development and testing of a gust generator model and the use of bio-inspired sensing wind hairs. Paper 1 used PIV to look at the trailing edge flaplet and the aft wake area to characterise the effect that the opening and closing effect of the flaplets had on the nearby flow and then how the structure generated developed downstream. The model developed and tested in Paper 1 has shown the ability to repeatedly generate horse-shoe shape vortexes, so that it can be used upstream to generate disturbances or to re-energise the boundary layer for potential flow control. Paper 2 developed sensing wind hair work, already carried out in our research group, and used the model from paper 1 as an upstream gust generator. This paper used PIV in the downstream wake to further characterise the disturbance generated by the gust generator and then PIV to analyse the effect that the gust had on the sensing array when placed in the same downstream location. The results were compared with each other and it was found that the sensing array could detect the arrival and structure of the generated disturbance, effectively detecting the 'footprint' of the flow. Paper 3 was a feasibility study into using an EBC in place of a high-speed camera in the traditional PIV setup. Comparative experiments were undertaken on the sensing array under various tunnel conditions with both traditional PIV and the EBC. These results were compared and they present the ability that the EBC and the sensing hairs have for future flow monitoring abilities. The EBC presents a new up-and-coming field in which real-time flow monitoring and feedback could be possible.

5.2 Purpose and Novelty

The work in this study initially started by building on work from my master's thesis, [21]. The gust generator model was one of the first pneumatically actuated models and the first to be used as an upstream gust generator. [81] used bellow actuators to control sweep on a NACA0012 20 years ago and since then, advances in shape morphing materials and the minimisation improvements in electronics and actuation have led to other researchers looking into pneumatically actuated wings. Just more recently researchers have started to investigate and analyse the effect that morphing wing technologies have, with a brief review of some current technologies in [82]. Pneumatics are not the usual choice of actuation, usually, the actuation is electronic, as there is a much wider variety available on the market, however, the benefits of pneumatics could prove useful. As already discussed in Paper 1, a wing has a constant source of high-pressure air and the pneumatic hardware required is much lighter than the equivalent hydraulic hardware. The model developed in Paper 1, is the first pneumatically actuated model to be used as an upstream gust generator, with the generated disturbance being studied via PIV.

The sensing array developed and tested in Paper 2, also builds on work from City, University of London, [62]. The array was integrated into an aerofoil and

placed downstream of the gust generator, the response of the hairs to known generated disturbances were compared to straight PIV results in the same downstream location under the same tunnel conditions. The hairs showed that they can accurately detect flow footprints and could be used as part of a relatively non-invasive flow monitoring system. Compared to other sensing hairs, from other research groups, these are low cost, as they don't have inbuilt sensing capabilities and are extremely easy to manufacture, requiring only a silicone sheet and a laser cutter.

Paper 3 presents a very novel way of PIV, using the sensing array and an EBC. Very little work has been carried out in terms of using an EBC for PIV, the most notable work being [61] in which PIV was carried out with an EBC. Using the sensing arrays alongside this setup is very novel and provides a great benefit in that the event rate is reduced. The hairs only bend in the chordwise direction and so limit out-of-plane motion and background noise. The work with the EBC shows great potential and should be further investigated.

5.3 Future Work

In each critical review, future works have been suggested, but can be summarised as follows:

- **Morphing Wing**
This could either be a fully enclosed morphing wing, such that the camber is modified via actuation in the trailing edge, or a continuous morphing trailing edge flaplet that can 'pop up' in specified spanwise locations. This could modify the lift distribution and provide benefits during different flight manoeuvres.
- **Smart Skin**
This would be the outer skin but with integrated sensors for other types of flow monitoring, smart skin could even be combined with the morphing wing idea to have a flexible smart skin. This flexible smart skin could be used over existing models and so would not require a complete redesign.
- **Machine Learning**
A wing with integrated sensing capabilities also has the ability to create a positive feedback control loop. In the case of the sensing hairs and the EBC, a machine learning algorithm could be used to learn the patterns and responses of the large flow structures that pass over the sensing hairs and then react accordingly.

5.4 Emerging Topics

Some other publications to note, since the publication of the papers are listed below.

Relating to Paper 1

The importance of developing reliable gust generation methods for use in wind tunnels has become very relevant recently. Researchers from DLR have developed an in-tunnel gust generator that can mimic wind gusts during flight, [83]. This has been developed as a novel method to meet carbon neutrality by 2050, by possible drag and weight reduction. Their gust generation method is via stationary aerofoils and downstream rotating cylinders to produce large repeatable gusts, and whilst this differs from the generation method in Paper 1, it still reinforces the need for gust generators.

Relating to Paper 2

Researchers at the US Air Force Laboratory have recently developed an optimisation algorithm to decide the best location of sensor placement on a delta wing [84]. Their sparse sensor placement optimisation for prediction (SSPOP) algorithm uses large datasets from flow situations to find and output the best sensor locations for near-optimal data sets. For AoA detection, the sensor locations were located in the top 1% of locations, judged by RMS values. The reduction in sensors required has shown reliability and flexibility benefits, compared to algorithms requiring large data sets. This optimisation of sensor layout is another step towards true fly-by-feel flight.

Relating to Paper 3

Very similar to the direction of Paper 3 is [85]. Wind tunnel flutter tests on parallel flexible membranes were conducted with an event-triggered camera and strobe laser at equivalent fps of 10,000. It was found that their proposed method could continuously record membrane flutter, unlike a traditional high-speed camera. Whilst the application is different to that of Paper 3, the basic conclusions remain the same, the EBC setup is far cheaper and records much less data than traditional cameras.

This page has been left blank to separate chapters

6 Calibration of Equipment

Contents

6.1	Water Tunnel	88
6.2	Wind Hairs	89

6.1 Water Tunnel

The water tunnel used in all experiments in this thesis refers to the ChB Water Tunnel at City, University of London. The tunnel is an open free surface with a recirculating system, the open surface schematic is shown below in Figure 45. The flow direction is left to right, as indicated by the arrow, and the test section is marked by red colouring. Before the flow enters the test section, the flow enters a diffuser and contractor and then after the test section flow is recirculated through filters and underneath the tunnel.

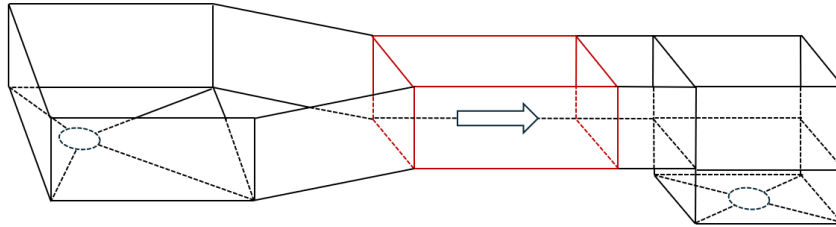


Figure 45: Schematic of the top, open surface of the water tunnel, with test section and flow direction highlighted. (Please note this is not to scale).

The water tunnel speed is controlled by adjusting the hp of the tunnel pump motor. However, the speed also depends on the amount of water in the tunnel and the blockage effect of the model(s) placed in the test section. To know with certainty the speed of the tunnel at a corresponding water, model and hp a tunnel calibration experiment was conducted. The tunnel was filled to 80% water capacity, as measured by:

$$80\% = \frac{\text{Water level height in test section}}{\text{Vertical test section height}} 100\% \quad (5)$$

The tunnel was suitably seeded and classical PIV measurements were taken centrally of the test section with no model(s), at varying pump hp settings. The PIV results were used to record the freestream velocity of the water as the hp was varied. The results are shown below in Figure 46.

This graph was used to select hp for accurate freestream velocities for all experiments in this thesis at 80% capacity.

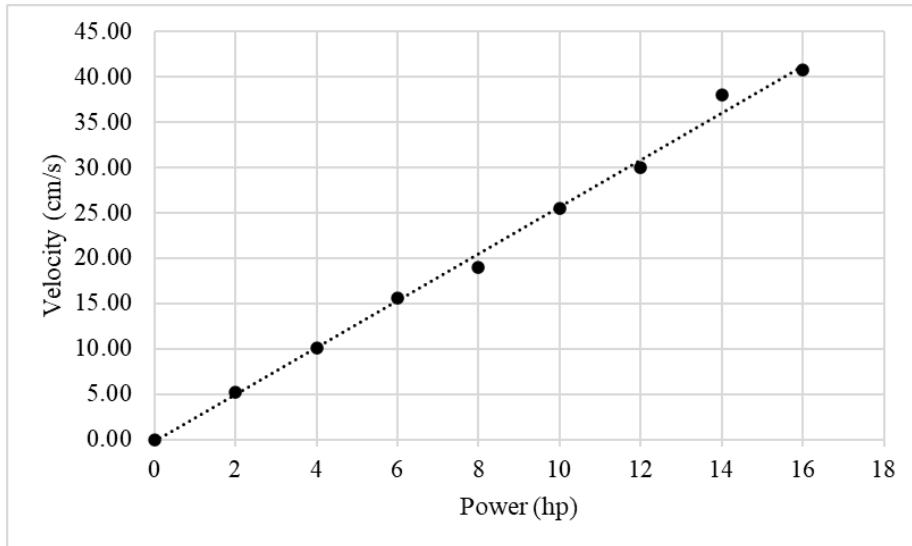


Figure 46: Graph with linear trend line fitted showing the variation of freestream velocity with pump hp. Dots represent data points, dashed line is a trend line

6.2 Wind Hairs

The first of the calibration tests carried out on the wind hairs prior to using them experimentally, was their response to freestream velocity changes. A row of wind hairs was mounted in the water tunnel and the high speed camera setup to monitor their response to the velocity changes. The tunnel velocity was set, allowed to settle, and then recordings were taken of the single chord of wind hairs. The leading edge hair deflection was time-averaged and noted. The graph plotted below in Figure 47 shows the leading edge pillar's response to varying freestream velocities. The results follow a linear trend, up to the freestream velocity of 35cm/s, as that was the maximum required experimentally. The maximum wind hair tip deflection encountered was in the order of 2mm.

The second set of calibration tests done on the wind hairs were structural tests. Again, a single row of hairs was placed in the water tunnel, with the high-speed camera setup outside the tunnel. A pillar was deflected with a wooden pointer and then released to return to its rest position, whilst being captured via the high-speed camera. This test was completed for each pillar and then the response averaged, as it is assumed that the properties of the silicone material are homogenous. The results are shown below in Figure 48, with an added trend line.

From Figure 48, it can be seen that the hairs follow a slightly underdamped motion, with a settling time of around 60ms. This informs our use of post-

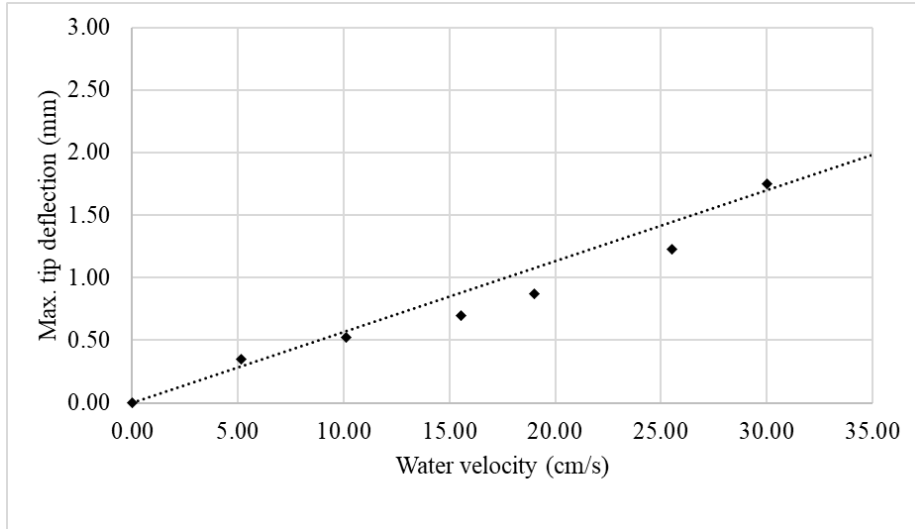


Figure 47: Graph to show the variation of pillar tip deflection with freestream velocity

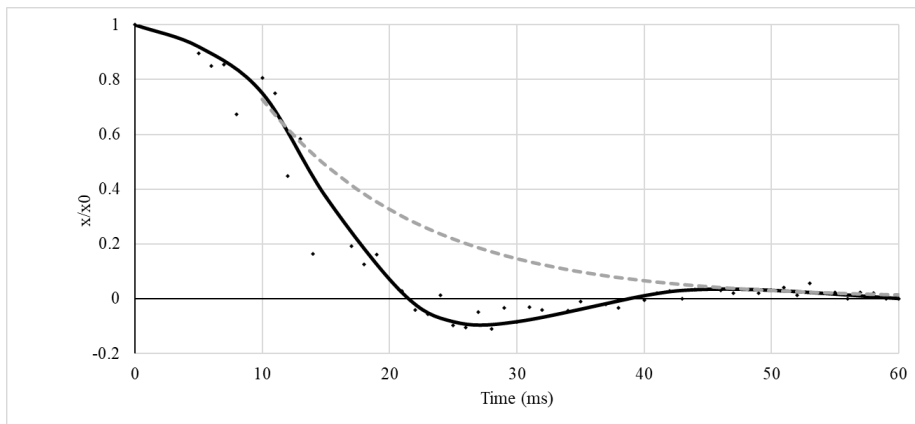


Figure 48: Damping curved average across chordwise pillars with a trend line fitted.

processing filters. The underdamped motion of the wind hairs can be described by the following equation of the general real solution:

$$x = e^{-\gamma t} A [\cos \omega_1 t - \alpha] \quad (6)$$

Where γ is the damping coefficient, t is time, A is amplitude, ω_1 is the sinusoid frequency and α is the phase. The equation for the line of best fit for the motion is roughly defined as follows:

$$y(t) = 8.2e^{-0.06t}$$

This page has been left blank to separate chapters

References

- [1] Antonis Chaliakopoulos. The myth of daedalus and icarus: Fly between the extremes, 2021.
- [2] Ludwig Heinrich Heydenreich. Leonardo da vinci. *Encyclopaedia Britannica*, 2024.
- [3] Allen Andres. *The flying machine: its evolution through the ages*. Putnam, New York, 1977.
- [4] Wikipedia. Wright brother. *Wikipedia*, Accessed August 2024.
- [5] David McCullough. *The Wright Brothers*. Simon & Schuster, New York, NY, 2015.
- [6] Airbus. An airbus futuristic conceptual airliner "takes flight" to inspire next-generation engineers, 2019.
- [7] Tom McKeag. Shape means strength, from a boeing dreamliner to a bone chair. Technical report, Trellis, 2014.
- [8] Tarah N. Sullivan, Bin Wang, Horacio D. Espinosa, and Marc A. Meyers. Extreme lightweight structures: avian feathers and bones. *Materials Today*, 20(7):377–391, 2017.
- [9] Xingyuan Zhang, Yunbo Luan, Yongcun Li, Zhihua Wang, Zhiqiang Li, Feng Xu, and Zhangxin Guo. Bioinspired design of lightweight laminated structural materials and the intralayer/interlayer strengthening and toughening mechanisms induced by the helical structure. *Composite Structures*, 276:114575, 2021.
- [10] Grant Turnbull. Bae systems reveals futuristic 'human' skin concept for aircraft. Technical report, Airforce Technology, 2014.
- [11] CAA. Caa's environmental sustainability strategy-our areas of work, 2022.
- [12] Tamsin Edwards Nuala Burnett and Nicole Watson. The uk's plans and progress to reach net zero by 2050, 2023.
- [13] Pascal de Marmier and Norman Wereley. *Control of Sweep Using Pneumatic Actuators to Morph Wings of Small Scale UAVs*. AIAA, 2003.
- [14] Julie Blondeau and Darryll Pines. *Pneumatic Morphing Aspect Ratio Wing*. AIAA, 2004.
- [15] Daochun Li, Shiwei Zhao, Andrea Da Ronch, Jinwu Xiang, Jernej Drolfenik, Yongchao Li, Lu Zhang, Yining Wu, Markus Kintscher, Hans Peter Monner, Anton Rudenko, Shijun Guo, Weilong Yin, Johannes Kirn, Stefan Storm, and Roeland De Breuker. A review of modelling and analysis of morphing wings. *Progress in Aerospace Sciences*, 100:46–62, 2018.

- [16] Emmanuel Siéfert, Etienne Reyssat, José Bico, and Benoit Roman. Bio-inspired pneumatic shape morphing elastomers. *Nature Materials*, 18(1):24–28, 2019.
- [17] Aniello Riccio, Andrea Sellitto, and Miriam Battaglia. Morphing spoiler for adaptive aerodynamics by shape memory alloys. *Actuators*, 13(9), 2024.
- [18] Alaeddine Zereg, Mounir Aksas, Mohamed Taher Bouzaher, Salah Laghrouche, and Nadhir Lebaal. Efficiency improvement of darrieus wind turbine using oscillating gurney flap. *Fluids*, 9(7), 2024.
- [19] M. Siclari, F. Austin, W. Van Nostrand, G. Volpe, M. Siclari, F. Austin, W. Van Nostrand, and G. Volpe. *Optimization of segmented flaps for in-flight transonic performance enhancement*.
- [20] Ralph Stephan, Nicolas Schneiders, Gerrit Weber, Florian Schueltke, Eike Stumpf, and Fabian Peter. Methodology for evaluating a distributed variable-camber trailing-edge system in preliminary aircraft design. *Journal of Aircraft*, 61(4):1057–1070, 2024.
- [21] Aleksandra Court. Trailing edge pneumatic systems for flow control. Master’s thesis, City, University of London, 2021.
- [22] Omar Selim, Erwin R. Gowree, Christian Lagemann, Edward Talboys, Chetan Jagadeesh, and Christoph Bruecker. The peregrine falcon’s dive: On the pull-out maneuver and flight control through wing-morphing, 2020.
- [23] Edward Talboys, Thomas F. Geyer, and Christoph Brücker. An aeroacoustic investigation into the effect of self-oscillating trailing edge flaplets. *Journal of Fluids and Structures*, 91:102598, November 2019.
- [24] Civil and Structural Engineer Media. Unpiloted aerial vehicle (uav) industry is booming due to increasing adoption of uav in-flight terrorism and increase in demand from commercial applications. Technical report, 2021.
- [25] Kieran T. Wood, Ronald M. Cheung, Thomas Richardson, Jonathan Cooper, Oliver Darbyshire, and Clyde Warsop. A new gust generator for a low-speed wind tunnel: Design and commissioning. In *AIAA SciTech Forum - 55th AIAA Aerospace Sciences Meeting*. American Institute of Aeronautics and Astronautics Inc. (AIAA), January 2017.
- [26] Alexander M. Pankonien and Daniel J. Inman. Aerodynamic performance of a spanwise morphing trailing edge concept. 2014.
- [27] Q. Chanzy and A.J. Keane. Analysis and experimental validation of morphing uav wings. *The Aeronautical Journal*, 122(1249):390–408, 2018.
- [28] Edward Talboys, Thomas Geyer, and Christoph Brücker. The aerodynamic and aeroacoustic effect of passive high frequency oscillating trailing edge flaplets. 06 2018.

- [29] Ben Ponitz, Anke Schmitz, Dominik Fischer, Horst Bleckmann, and Christoph Bruecker. Diving-flight aerodynamics of a peregrin falcon (*falco peregrinus*). *PloS one*, 2014.
- [30] Manoranjan Majji, Othon Rediniotis, and John Junkins. Design of a morphing wing: Modeling and experiments. *AIAA Atmospheric Flight Mechanics*, 08 2007.
- [31] Musavir Bashir and Parvathy Rajendran. Recent trends in piezoelectric smart materials and its actuators for morphing aircraft development. *International Review of Mechanical Engineering*, 02 2019.
- [32] Anders Hedenström and L. Christoffer Johansson. Bat flight: aerodynamics, kinematics and flight morphology. *Journal of Experimental Biology*, 218(5):653–663, 03 2015.
- [33] Alden Midmer and Christoph Brücker. Nature-inspired self-adaptive wingtip for vortex mitigation. 09 2022.
- [34] Ashok Gopalarathnam and Rachel King Norris. Ideal lift distributions and flap angles for adaptive wings. *Journal of Aircraft*, 46(2):562–571, 2009.
- [35] Marco Rosti, Mohammad Omidyeganeh, and Alfredo Pinelli. Numerical simulation of a passive control of the flow around an aerofoil using a flexible, self adaptive flaplet. *Flow, Turbulence and Combustion*, 100, 06 2018.
- [36] B T Dickinson. Hair receptor sensitivity to changes in laminar boundary layer shape. *Bioinspiration and Biomimetics*, 5(1):016002, feb 2010.
- [37] S Sterbing-D’Angelo, M Chadha, and C Moss. Functional role of airflow-sensing hairs on the bat wing. *Journal of neurophysiology*, 117(2):705–712, 2017.
- [38] A.G.P. Kottapalli, M. Asadnia, J.M. Miao, and M.S. Triantafyllou. Harbor seal whisker inspired flow sensors to reduce vortex-induced vibrations. In *2015 28th IEEE International Conference on Micro Electro Mechanical Systems (MEMS)*, pages 889–892, 2015.
- [39] Robyn A. Grant, Ben Mitchinson, Charles W. Fox, and Tony J. Prescott. Active touch sensing in the rat: Anticipatory and regulatory control of whisker movements during surface exploration. *Journal of Neurophysiology*, 101(2):862–874, 2009. PMID: 19036871.
- [40] Dominic Keidel, Urban Fasel, and Paolo Ermanni. Control authority of a camber morphing flying wing. *Journal of Aircraft*, 57(4):603–614, 2020.
- [41] Madeleine Seale, Cathal Cummins, Ignazio Viola, Enrico Mastropaolo, and Naomi Nakayama. Design principles of hair-like structures as biological machines. *Journal of The Royal Society Interface*, 15, 2018.

- [42] Junliang Tao and Xiong (Bill) Yu. Hair flow sensors: from bio-inspiration to bio-mimicking—a review. *Smart Materials and Structures*, 21(11):113001, sep 2012.
- [43] Alex C. Hollenbeck, Ramana Grandhi, John H. Hansen, and Alexander M. Pankonien. Bioinspired artificial hair sensors for flight-by-feel of unmanned aerial vehicles: A review. *AIAA Journal*, 61(12):5206–5231, 2023.
- [44] Christoph Brücker, J Spatz, and Wolfgang Schröder. Feasibility study of wall shear stress imaging using microstructured surfaces with flexible micropillars. *Experiments in fluids*, 39:464–474, 2005.
- [45] Christoph H Bruecker and Vladimir Mikulich. Sensing of minute airflow motions near walls using pappus-type nature-inspired sensors. *Plos one*, 12(6):e0179253, 2017.
- [46] D Shen, Y Jiang, and Z. et al Ma. Bio-inspired flexible airflow sensor with self-bended 3d hair-like configurations. *Journal of Bionic Engineering*, 19:73–82, 2022.
- [47] Wennan Xiong, Chen Zhu, Dongliang Guo, Chao Hou, Zhaoxi Yang, Zhangyu Xu, Lei Qiu, Hua Yang, Kan Li, and YongAn Huang. Bio-inspired, intelligent flexible sensing skin for multifunctional flying perception. *Nano Energy*, 90:106550, 2021.
- [48] Francesco Rizzi, Antonio Quattieri, Tommaso Dattoma, Gianmichele Epifani, and Massimo De Vittorio. Biomimetics of underwater hair cell sensing. *Microelectronic Engineering*, 132:90–97, 2015. Micro and Nanofabrication Breakthroughs for Electronics, MEMS and Life Sciences.
- [49] Yingchen Yang, Nam Nguyen, Nannan Chen, Michael Lockwood, Craig Tucker, Huan Hu, Horst Bleckmann, Chang Liu, and Douglasl Jones. Artificial lateral line with biomimetic neuromasts to emulate fish sensing. *Bioinspiration and Biomimetics*, 2010.
- [50] J Dusek, Ajay Kottapalli, Mohsen Asadnia, Jianamin Miao, and Micheal Triantafyllou. Development and testing of bio-inspired microelectromechanical pressure sensor arrays for increased situational awareness for marine vehicles. *Smart Materials and Structures*, 2013.
- [51] A. Kottapalli, M. Bora, and M. et al Asadnia. Nanofibril scaffold assisted mems artificial hydrogel neuromasts for enhanced sensitivity flow sensing. *Sci Rep*, 2016.
- [52] Mohsen Asadnia, Ajay Kottapalli, Reza Haghghi, Audren Cloitre, Pablo Alvarado, Jianmin Miao, and Micheal Triantafyllou. MemS sensors for assessing flow-related control of an underwater biomimetic robotic stingray. *Bioinspiration and Biomimetics*, 2015.

- [53] Omar Selim and Christoph Brücker. Aerofoil flow sensing using on-board optical tracking of flexible pillar sensors. *Fluids*, 8(5), 2023.
- [54] Xingwen Zheng, Amar Kamat, Ming Cao, and Ajay Kottapalli. Creating underwater vision through wavy whiskers: a review of the flow-sensing mechanisms and biomimetic potential of seal whiskers. *Journal of The Royal Society Interface*, 12, 2021.
- [55] Heather R. Beem and Michael S. Triantafyllou. Wake-induced ‘slaloming’ response explains exquisite sensitivity of seal whisker-like sensors. *Journal of Fluid Mechanics*, 783:306–322, 2015.
- [56] Guido Dehnhart, Bjorn Mauck, and Horst Bleckmann. Seal whiskers detect water movements. *Nature*, 1998.
- [57] Daochun Li, Shijun Guo, Tariq Osman Aburass, Daqing Yang, and Jinwu Xiang. Active control design for an unmanned air vehicle with a morphing wing. *Aircraft Engineering and Aerospace Technology: An International Journal*, 88, 2016.
- [58] Aleksandra Court, Omar Selim, and Christoph Bruecker. Design and implementation of spanwise lift and gust control via arrays of bio-inspired individually actuated pneumatic flaplets. *International Journal of Numerical Methods for Heat and Fluid Flow*, 33(4):1528–1543, 2023.
- [59] Qianhui Li, Evangelos Stavropoulos-Vasilakis, Phoivos Koukouvinis, Manolis Gavaises, and Christoph H. Bruecker. Micro-pillar sensor based wall-shear mapping in pulsating flows: In-situ calibration and measurements in an aortic heart-valve tester. *Journal of Fluids and Structures*, 105:103346, 2021.
- [60] Dajun Liu and Takafumi Nishino. Numerical analysis on the oscillation of stall cells over a naca 0012 aerofoil. *Computers and Fluids*, 175:246–259, 2018.
- [61] Christian E. Willert and Joachim Klinner. Event-based imaging velocimetry: an assessment of event-based cameras for the measurement of fluid flows. *Experiments in Fluids*, 63, 2022.
- [62] Omar Selim and Christoph Brücker. Detecting separation pre-cursors using on-board optical tracking of flexible pillar sensors. *Proceedings of the International Symposium on the Application of Laser and Imaging Techniques to Fluid Mechanics*, 20:1–17, 07 2022.
- [63] Shuvashis Dey, Rahul Bhattacharyya, Sanjay E. Sarma, and Nemai Chandra Karmakar. A novel “smart skin” sensor for chipless rfid-based structural health monitoring applications. *IEEE Internet of Things Journal*, 8(5):3955–3971, 2021.

- [64] Yu Wang, Shuguang Hu, Tao Xiong, Yongan Huang, and Lei Qiu. Recent progress in aircraft smart skin for structural health monitoring. *Structural Health Monitoring*, 21(5):2453–2480, 2022.
- [65] Donglai () Gao, Hao () Meng, Yewei () Huang, Guanbin () Chen, and Wen-Li () Chen. Active flow control of the dynamic wake behind a square cylinder using combined jets at the front and rear stagnation points. *Physics of Fluids*, 33(4):047101, 04 2021.
- [66] Feng Ren, Hai-bao Hu, and Hui Tang. Active flow control using machine learning: A brief review. *Journal of Hydrodynamics*, 32:247–253, 04 2020.
- [67] Misha Mahowald. Vlsi analogs of neuronal visual processing: a synthesis of form and function, aug 1992.
- [68] Carver Mead. *Analog VLSI and neural systems*. Addison-Wesley Longman Publishing Co., Inc., USA, 1989.
- [69] Patrick Lichtsteiner, Christoph Posch, and Tobi Delbruck. A 128×128 120 db 15 μ s latency asynchronous temporal contrast vision sensor. *IEEE Journal of Solid-State Circuits*, 43(2):566–576, 2008.
- [70] Bongki Son, Yunjae Suh, Sungho Kim, Heejae Jung, Jun-Seok Kim, Changwoo Shin, Keunju Park, Kyoobin Lee, Jinman Park, Jooyeon Woo, Yohan Roh, Hyunku Lee, Yibing Wang, Iliia Ovsianikov, and Hyunsurk Ryu. 4.1 a 640×480 dynamic vision sensor with a 9μ m pixel and 300meps address-event representation. In *2017 IEEE International Solid-State Circuits Conference (ISSCC)*, pages 66–67, 2017.
- [71] T. Delbruck and P. Lichtsteiner. Fast sensory motor control based on event-based hybrid neuromorphic-procedural system. In *2007 IEEE International Symposium on Circuits and Systems (ISCAS)*, pages 845–848, 2007.
- [72] Guillermo Gallego, Tobi Delbrück, Garrick Orchard, Chiara Bartolozzi, Brian Taba, Andrea Censi, Stefan Leutenegger, Andrew J. Davison, Jörg Conradt, Kostas Daniilidis, and Davide Scaramuzza. Event-based vision: A survey. *IEEE Transactions on Pattern Analysis and Machine Intelligence*, 44(1):154–180, 2022.
- [73] Christian E Willert. Event-based imaging velocimetry using pulsed illumination. *Experiments in Fluids*, 64(5):98, 2023.
- [74] Christian Willert and Joachim Klinner. Time-resolved velocity profile measurement using event-based imaging. In *15th International Symposium on Particle Image Velocimetry–ISPIV 2023*. The California State University (ScholarWorks), 2023.
- [75] Alecsandra Court and Christoph Bruecker. Fly by feel: Flow event detection via bioinspired wind-hairs. *Fluids*, 9(3), 2024.

- [76] Václav Uruba and Pavel Procházka. The Reynolds number effect on dynamics of the wake behind a circular cylinder. *AIP Conference Proceedings*, 2189(1):020023, 11 2019.
- [77] Trishik Ghosh. Harnessing biomimicry for vortex shedding in aerodynamic environments. Master’s thesis, City, University of London, 2024.
- [78] Xinyi Wu and Zhiwei Xu. Deflection monitoring of morphing winglet by binocular vision system with environment adaptability. *Mechanical Systems and Signal Processing*, 185:109696, 2023.
- [79] Xusheng Mu, Rui Huang, Qitong Zou, and Haiyan Hu. Machine learning-based active flutter suppression for a flexible flying-wing aircraft. *Journal of Sound and Vibration*, 529:116916, 2022.
- [80] Kasper Trolle Borup, Thor Inge Fossen, and Tor Arne Johansen. A machine learning approach for estimating air data parameters of small fixed-wing uavs using distributed pressure sensors. *IEEE Transactions on Aerospace and Electronic Systems*, 56(3):2157–2173, 2020.
- [81] Pascal de Marmier and Norman Wereley. *Control of Sweep Using Pneumatic Actuators to Morph Wings of Small Scale UAVs*. ARC, 2003.
- [82] Cevdet Özel, Emre Özbek, and Selcuk Ekici. A review on applications and effects of morphing wing technology on uavs. *International Journal of Aviation Science and Technology*, 01(01):30–40, 2020.
- [83] Thomas G. Schmidt, Johannes Dillinger, Markus Raimund Ritter, Anna Altkuckatz, Charlotte Hanke, Marc Braune, Wolf R. Krüger, and Holger Mai. Design and experimental characterization of a gust-generator concept with rotating-slotted cylinders in the low-speed wind tunnel dnw-nwb. In *International Forum on Aeroelasticity and Structural Dynamics, IFASD 2024*, June 2024.
- [84] Alex Hollenbeck, Atticus Beachy, Ramana Grandhi, and Alexander Pankonien. Data-driven sparse sensor placement optimization on wings for flight-by-feel: Bioinspired approach and application. *Preprints*, September 2024.
- [85] Zhen Lyu, Weiwei Cai, and Yingzheng Liu. High-frequency visualization of flexible structures using an event-triggered camera: multiple flapping membranes. *Measurement Science and Technology*, 35(5):055302, feb 2024.

7 Appendices

7.1 A

metavision vibration estimation

```
# Copyright (c) Prohese S.A. - All Rights Reserved
#
# Subject to Prohese Metavision Licensing Terms and Conditions ("License T&C's").
# You may not use this file except in compliance with these License T&C's.
# A copy of these License T&C's is located in the "licensing" folder accompanying
this file.

"""
Simple script to estimate the frequency of vibrating objects.
It will display a window with a visualization of the events, and
another with the frequency for pixels with periodic motion.
You can use it for example, with the file monitoring_40_50hz.raw
from Metavision Datasets that can be downloaded from our documentation.
"""

from metavision_core.event_io import EventsIterator
from metavision_core.event_io import LiveReplayEventsIterator, is_live_camera
from metavision_sdk_analytics import FrequencyMapAsyncAlgorithm
from metavision_sdk_ui import EventLoop

from vibration_gui import VibrationGUI

def parse_args():
    import argparse
    """Parse command line arguments."""
    parser = argparse.ArgumentParser(description='Vibration estimation sample.',
                                    formatter_class=argparse.ArgumentDefaultsHelpFormatter)

    # Base options
    base_options = parser.add_argument_group('Base options')
    base_options.add_argument(
        '-i', '--input-raw-file', dest='input_path', default="",
        help="Path to input RAW file. If not specified, the live stream of the
        first available camera is used. "
        "If it's a camera serial number, it will try to open that camera
        instead.")
    base_options.add_argument('--process-from', dest='process_from', type=int,
                              default=0,
                              help='Start time to process events (in us).')
    base_options.add_argument('--process-to', dest='process_to', type=int,
```

```

default=None,
                                help='End time to process events (in us).')

# Estimation mode options
estimation_options = parser.add_argument_group('Estimation mode options')
estimation_options.add_argument('--min-freq', dest='min_freq', type=float,
                                default=10,
                                help='Minimum detected frequency (in Hz).')
estimation_options.add_argument('--max-freq', dest='max_freq', type=float,
                                default=150,
                                help='Minimum detected frequency (in Hz).')
estimation_options.add_argument('--filter-length', dest='filter_length',
                                type=int, default=7,
                                help='Number of successive periods to
                                detect a vibration.')
estimation_options.add_argument(
    '--max-period-diff', dest='max_period_diff', type=int, default=1500,
    help='Period stability threshold - the maximum difference (in us)
    between two periods to be considered the same.')
estimation_options.add_argument('--update-freq', dest='update_freq_hz',
                                default=25,
                                type=float, help='Update frequency of
                                the algorithm (in Hz).')
estimation_options.add_argument(
    '--freq-precision', dest='freq_precision_hz', type=float, default=1,
    help='Precision of frequency calculation - Width of frequency bins
    in histogram (in Hz).')
estimation_options.add_argument(
    '--min-pixel-count', dest='min_pixel_count', type=int, default=25,
    help='Minimum number of pixels to consider a frequency "real",
    i.e not coming from noise')

# Outcome Options
outcome_options = parser.add_argument_group('Outcome options')
outcome_options.add_argument(
    '-o', '--out-video', dest='out_video', type=str, default="",
    help="Path to an output AVI file to save the resulting video.
    A frame is generated every time the frequency measurement
    callback is called.")

# Replay Option
replay_options = parser.add_argument_group('Replay options')
replay_options.add_argument(

```

vibration gui

```
# Copyright (c) Prophesee S.A. - All Rights Reserved
#
# Subject to Prophesee Metavision Licensing Terms and Conditions
("License T&C's").
# You may not use this file except in compliance with these License
T&C's.
# A copy of these License T&C's is located in the "licensing" folder
accompanying this file.

"""
Utility classes to generate and display an image from a frequency map
and allow the user to interact with the mouse or
the keyboard to select pixels or regions of which he wants to know
the dominant frequency.
"""

import cv2
from metavision_sdk_analytics import DominantValueMapAlgorithm,
HeatMapFrameGeneratorAlgorithm
from metavision_sdk_ui import BaseWindow, MTWindow, UIAction,
UIKeyEvent

class VibrationGUI:
    """
    Class that displays every received frequency map using a color map
    and prints the dominant frequency. In addition, this GUI
    stage allows:
        - defining ROIs in the frequency map and print their dominant
        frequency
        - checking the frequency at a specific pixel in the frequency
        map

    Args:
        width (int): Sensor's width.
        height (int): Sensor's height.
        min_freq (float): Minimum detected frequency (in Hz).
        max_freq (float): Maximum detected frequency (in Hz).
        freq_precision (float): Precision of frequency calculation
        - Width of frequency bins in histogram (in Hz).
        min_pixel_count (int): Minimum number of pixels to consider
        a frequency "real", i.e not coming from noise.
        outvideo (str): Path to output AVI file to save slow motion
        video.
```

```

"""

def __init__(self, width, height, min_freq, max_freq,
freq_precision, min_pixel_count, out_video):
    self._frame_generator = DominantFrequencyFrameGenerator
        (width, height, min_freq, max_freq,

                freq_precision, min_pixel_count)
    self._window = MTWindow(title="Vibration estimation",
width=width, height=self._frame_generator.full_height,
                mode=BaseWindow.RenderMode.BGR,
                open_directly=True)
    self._window.show_async(self._frame_generator.
output_img)

    self._crt_roi_start_pos = (-1, -1)

    # Video Writer
    self.out_video = out_video
    if self.out_video:
        fourcc = cv2.VideoWriter_fourcc('M', 'J', 'P',
'G')
        self.video_name = out_video + ".avi"
        self.video_writer = cv2.VideoWriter(self.video_name,
fourcc, 20,
                (width, self._frame_generator.full_height))

    # Help message
    self._display_long_help = False
    self._long_help_msg = ["Keyboard/mouse actions:",
        " \h\" - show/hide the help menu",
        " \q\" - quit the application",
        " \c\" - clear all the ROIs",
        " Click and drag to create ROIs"]

    self._short_help_msg = ["Press 'h' for help"]

    # Event callbacks
    self._last_mouse_pos = (-1, -1)
    self._is_updating_roi = False
    self._rois = []

    def cursor_cb(x, y):
        window_width, window_height = self._window.get_size()
        # The window may have been resized meanwhile.
        So we map the coordinates to the original window's size.

```

```

mapped_x = x * self._frame_generator.full_width /
window_width
mapped_y = y * self._frame_generator.full_height /
window_height
mouse_pos = (int(mapped_x), int(mapped_y))

# The frequency map is smaller than the displayed
image (a color map bar is added). So we need to check
# that we won't be out of bounds.
if (mouse_pos[0] < 0) or (mouse_pos[0] >= width):
    return
if (mouse_pos[1] < 0) or (mouse_pos[1] >= height):
    return

# Update the last created ROI
if (self._is_updating_roi and self._rois):
    xmin = min(self._crt_roi_start_pos[0], mouse_pos[0])
    xmax = max(self._crt_roi_start_pos[0], mouse_pos[0])
    ymin = min(self._crt_roi_start_pos[1], mouse_pos[1])
    ymax = max(self._crt_roi_start_pos[1], mouse_pos[1])
    self._rois[-1] = ((xmin, ymin), (xmax, ymax))

self._last_mouse_pos = mouse_pos

def mouse_cb(button, action, mods):
    if action == UIAction.PRESS:
        # Start a new ROI
        self._is_updating_roi = True
        self._crt_roi_start_pos = self._last_mouse_pos
        self._rois.append((self._last_mouse_pos,
            (self._last_mouse_pos[0]+1, self._last_mouse_pos[1]+1)))
    elif action == UIAction.RELEASE:
        # Stop updating the ROI
        self._is_updating_roi = False

def keyboard_cb(key, scancode, action, mods):
    if action != UIAction.RELEASE:
        return
    if key == UIKeyEvent.KEY_ESCAPE or key == UIKeyEvent.KEY_Q:
        self._window.set_close_flag()
    elif key == UIKeyEvent.KEY_C:
        self._rois = []
    elif key == UIKeyEvent.KEY_H:
        self._display_long_help = not self._display_long_help

self._window.set_cursor_pos_callback(cursor_cb)

```

```

        self._window.set_mouse_callback(mouse_cb)
        self._window.set_keyboard_callback(keyboard_cb)

    def show(self, freq_map):
        """
        Processes the frequency map and displays the resulting
        image in the window.

        Args:
            freq_map (np.array): Floating point 2D frequency map
        """
        self._frame_generator.generate_bgr_image(freq_map)
        self._frame_generator.print_dominant_frequency(freq_map)
        self._frame_generator.print_cursor_frequency(
            freq_map, self._last_mouse_pos)
        self._frame_generator.print_rois_frequencies(
            freq_map, self._rois)
        self._frame_generator.print_help_message(
            self._long_help_msg if self._display_long_help
            else self._short_help_msg)

        self._window.show_async(self._frame_generator.output_img)
        if self.out_video:
            self.video_writer.write(self._frame_generator.output_img)

    def should_close(self):
        """
        Indicates whether the window has been asked to close.

        Returns:
            True if the window should close, False otherwise
        """
        return self._window.should_close()

    def destroy_window(self):
        """
        Destroys the current window.
        This function must only be called from the main thread.
        """
        self._window.destroy()
        if self.out_video:
            self.video_writer.release()
            print("Video has been saved in " + self.video_name)

class DominantFrequencyFrameGenerator:

```

```

"""
Class that converts a frequency map into an image and prints
dominant frequencies on top of it:
    - dominant frequency of the whole field of view
    - dominant frequencies of regions of interest in the
      frequency map
    - dominant frequency pointed by the mouse cursor

Attributes:
    full_height (int): Image's height (Sensor's height +
    color bar's height).
    full_width (int): Image's width (Sensor's width).
    output_img (np.array): CV_8UC3 color image representing
    the frequency map and the dominant frequencies.

Args:
    width (int): Sensor's width.
    height (int): Sensor's height.
    min_freq (float): Minimum detected frequency (in Hz).
    max_freq (float): Maximum detected frequency (in Hz).
    freq_precision (float): Precision of frequency calculation -
    Width of frequency bins in histogram (in Hz).
    min_pixel_count (int): Minimum number of pixels to consider
    a frequency "real", i.e not coming from noise.
"""

def __init__(self, width, height, min_freq, max_freq,
freq_precision, min_pixel_count):
    # Constants
    self._font_face = cv2.FONT_HERSHEY_PLAIN # Font used for
text rendering
    self._font_scale = 1.0 # Font scale used for text rendering
    self._thickness = 1 # Line thickness used for text rendering
    self._margin = 5 # Additional space used for text rendering

    self._width = width
    self._height = height

    # Heatmap frame generator
    self._heat_map_generator = HeatMapFrameGeneratorAlgorithm(
        min_freq, max_freq, freq_precision, width, height, "Hz")
    self.output_img = self._heat_map_generator.get_output_image()
    self.full_height = self._heat_map_generator.full_height
    self.full_width = self._heat_map_generator.full_width

    # Dominant value map algorithm

```

```

self._dominant_value_map_algo_ = DominantValueMapAlgorithm(
    min_freq, max_freq, freq_precision, min_pixel_count)

# Initialize some parameters used when rendering texts
(_, text_height), baseline = cv2.getTextSize("Frequency:
XXXX Hz", self._font_face, self._font_scale, self._thickness)
self._dominant_freq_text_pos_ = (self._margin, height -
baseline - self._margin)
self._help_msg_text_pos_ = (self._margin, text_height +
self._margin)
self._text_full_height = text_height + baseline

# Estimate the number of decimal digits to display in a
string using freq_precision
self._value_string_precision = 0
shifted_float_val = freq_precision
while abs(shifted_float_val - int(shifted_float_val+0.01)) > 0.00001:
    self._value_string_precision += 1
    shifted_float_val *= 10

# Print a message in the window at the beginning of the application
# when no frequency map has been received yet
self.output_img[:] = 0
init_message_1 = "NO VIBRATING OBJECT IN THE"
init_message_2 = "FIELD OF VIEW OF THE CAMERA"

init_font = cv2.FONT_HERSHEY_SIMPLEX
init_font_scale = 1
init_thickness = 2
y_mid = int(0.5 * self.output_img.shape[0])
(text_width1, _), baseline1 = cv2.getTextSize
(init_message_1, init_font, init_font_scale, init_thickness)
(text_width2, text_height2), _ = cv2.getTextSize(init_message_2,
init_font, init_font_scale, init_thickness)
x1 = int(0.5 * (self.output_img.shape[1] - text_width1))
x2 = int(0.5 * (self.output_img.shape[1] - text_width2))

cv2.putText(self.output_img, init_message_1, (x1, y_mid -
baseline1),
            init_font, init_font_scale, (255, 255, 255),
            init_thickness)
cv2.putText(self.output_img, init_message_2, (x2, y_mid +
text_height2),
            init_font, init_font_scale, (255, 255, 255),
            init_thickness)

```

```

def _freq_to_string(self, freq):
    """
    Converts floating point frequency to string with a given
    number of decimal digits.

    Args:
        freq (float): Floating point frequency
    """
    return "{:.{prec}f}".format(freq, prec=self._value_string_
precision)

def print_dominant_frequency(self, freq_map):
    """
    Computes and prints the dominant frequency measured in
    the camera's FOV.

    Args:
        freq_map (np.array): Floating point 2D frequency map
    """
    # Compute dominant frequency
    success, dominant_frequency = self._dominant_value_map_algo_.compute_dominant_value

    msg = "Frequency:"
    if success:
        msg += " " + self._freq_to_string(dominant_frequency) + " Hz"
    else:
        msg += "    N/A"

    cv2.putText(self.output_img, msg, self._dominant_freq_text_pos,
                self._font_face, self._font_scale, (255, 255, 255)
                , self._thickness)

def print_cursor_frequency(self, freq_map, mouse_position):
    """
    Prints the frequency pointed by the mouse cursor.

    Args:
        freq_map (np.array): Floating point 2D frequency map
        mouse_position (tuple(int)): Most recent 2D coordinates
        of the mouse cursor.
    """
    if (mouse_position[0] < 0) or (mouse_position[0] >= self._width):
        return
    if (mouse_position[1] < 0) or (mouse_position[1] >= self._height):
        return

```

```

freq = int(freq_map[mouse_position[1]][mouse_position[0]])
if freq > 0:
    cv2.putText(self.output_img, self._freq_to_string(freq) +
        " Hz", mouse_position,
                self._font_face, self._font_scale, (255, 255,
                255), self._thickness)

def print_rois_frequencies(self, freq_map, rois):
    """
    Prints the ROIs and their associated dominant frequency.

    Args:
        freq_map (np.array): Floating point 2D frequency map
        rois ([tuple(tuple(int))]): Regions of interest for which
        the dominant frequency is to be estimated.
        Each ROI is defined with its
        top-left and bottom-right positions.
    """
    for roi in rois:
        top_left = roi[0]
        bot_right = roi[1]
        cv2.rectangle(self.output_img, top_left, bot_right, (0, 255,
        255))

        roi_freq_map = freq_map[top_left[1]:bot_right[1]+1,
        top_left[0]:bot_right[0]+1]
        success, dominant_frequency = self._dominant_value_map_algo_
        .compute_dominant_value(roi_freq_map)

        msg = self._freq_to_string(dominant_frequency) + " Hz" if
        success else "N/A"
        cv2.putText(self.output_img, msg, (bot_right[0] + self._margin,
        bot_right[1]),
                    self._font_face, self._font_scale, (255, 255, 255),
                    self._thickness)

def print_help_message(self, help_msg_list):
    """
    Prints a help message indicating which interactions are possible.

    Args:
        help_msg_list ([string]): Help message, in the form of a
        list of lines to be printed
    """
    pos_x, pos_y = self._help_msg_text_pos_
    for line in help_msg_list:

```

```

        cv2.putText(self.output_img, line, (pos_x, pos_y),
                    self._font_face, self._font_scale, (255, 255,
                    255), self._thickness)
        pos_y += self._text_full_height

def generate_bgr_image(self, freq_map):
    """
    Generates and displays a BGR image corresponding to a
    frequency map.
        - converts the frequency map to an BGR image,
        - prints the dominant frequency in the whole FOV,
        - prints all the created ROIs and their associated
        dominant frequencies,
        - prints the dominant frequency pointed by the mouse cursor,
        - prints a help message

    Args:
        freq_map (np.array): Floating point 2D frequency map
    """
    # Generate the heat map
    self._heat_map_generator.generate_bgr_heat_map(
        freq_map, self.output_img)

```